# ABSTRACT

Title of Dissertation: PHASE TRANSITIONS
IN RANDOM QUANTUM CIRCUITS

Pradeep Niroula
Doctor of Philosophy, 2023

Dissertation Directed by: Professor Michael Gullans, Professor Alexey Gorshkov
Department of Physics

Random circuits have emerged as an invaluable tool in the quantum computing toolkit. On the one hand, the task of sampling outputs from a random circuit has established itself as a promising approach to experimentally demonstrate the superiority of quantum computers using near-term, noisy platforms. On the other hand, random circuits have also been used to deduce far-reaching conclusions about the theoretical foundations of quantum information and communication.

One intriguing aspect of random circuits is exemplified by the entanglement phase transition that occurs in monitored circuits, where unitary gates compete with projective measurements to determine the entanglement structure of the resulting quantum state. When the measurements are sparse, the circuit is unaffected and entanglement grows ballistically; when the measurements are too frequent, the unitary dynamics is arrested or frozen. The two phases are separated by a sharp-phase transition. In this work, we discuss an experiment probing such phases using a trapped-ion quantum computer.

While entanglement is an important resource in quantum communication, it does not fully capture the non-classicality necessary to achieve universal quantum computation. A family of measures, termed "magic", is used to quantify the extent to which a quantum state can enable universal quantum computation. In this dissertation, we also discuss a newly uncovered phase transition in magic using quantum circuits that implement a random stabilizer code. This phase transition is intimately related to the error correction threshold. In this work, we present numerical and analytic characterizations of the magic transition.

Finally, we use a statistical mechanical mapping from random circuits acting on qubits to Ising models to suggest thresholds in error mitigation whenever the underlying noise of a quantum device is imperfectly characterized. We demonstrate the existence of an error-mitigation threshold in dimensions $D \geq 2$.

# PHASE TRANSITIONS IN RANDOM QUANTUM CIRCUITS

by

Pradeep Niroula

Dissertation submitted to the Faculty of the Graduate School of the
University of Maryland, College Park in partial fulfillment
of the requirements for the degree of
Doctor of Philosophy
2023

Advisory Committee:
Professor Maissam Barkeshli, Chair
Professor Alexey Gorshkov, Co-chair/Co-Advisor
Professor Michael Gullans, Co-chair/Co-Advisor
Professor Christopher Monroe
Professor Christopher Jarzynski

# Acknowledgments

This dissertation truly is a culmination of the collective efforts and contributions of many individuals, and I am profoundly grateful for each and every one of them.

I am thankful to Alexey Gorshkov, who took me under his wings when I was a floundering undergraduate and later when I started graduate school. Alexey's unwavering belief in me, coupled with his boundless curiosity, energy, and kindness, has been a constant source of inspiration. I am eternally grateful for his mentorship and guidance.

I am also indebted to Michael Gullans, who I was lucky to have met early in my graduate years. This thesis would not have been possible without Michael's steadfast guidance and support throughout the various projects we undertook together. His remarkable prescience, enthusiasm, and willingness to help have left an indelible mark on me. I am truly fortunate to have had him as a mentor.

I hope to, one day, be able to emulate their wisdom and enthusiasm.

I would be remiss if I didn't express my gratitude to my collaborators: Andrii Maksymov, Abhinav Desphpande, Adam Ehrenberg, Bill Fefferman, Brayden Ware, Crystal Noel, Christopher Monroe, Christopher White, Daiwei Zhu, Domink Hangleiter, Igor Boettcher, Jake Bringewatt, Nikodem Grzesiak, Oles Shtanko, Przemyslaw Bienias, Qingfeng Wang, Sarang Gopalakrishnan, Sonika Johri, Yunseong Nam, and others from whom I have had the privilege of learning. Their contributions and insights have greatly enriched my research journey.

I would also like to thank my old friends and colleagues at IonQ, who made navigating the challenges of the pandemic a little easier.

A special thanks to Josiland Chambers, Melissa Britton, and Andrea Svejda for their patience and assistance with administrative matters.

I am also grateful to everyone at QuICS for creating a special and supportive environment.

Lastly, I want to express my deepest appreciation to my family for their unwavering encouragement and support throughout this journey.

# Table of Contents

# List of Figures

# List of Abbreviations

PEC Probabilistic Error Cancellation

RFIM Random Field Ising Model

SSRE Second Stabilizer Renyi Entropy

TVD Total Variation Distance

XEB Linear Cross Entropy

# Chapter 1: Introduction to Random Quantum Circuits

The technique of randomization has proven to be valuable in gaining insights into physics and information theory by abstracting away microscopic details. Notably, random matrix theory originated from Wigner's exploration of spectral gaps in heavy nuclei [1,2]. Similarly, foundational work on communication channels relied on observations about random error correcting codes [3]. Random quantum circuits follow in the footsteps of these approaches and have successfully contributed to our understanding of fundamental concepts in quantum information theory.

In quantum information theory, a "circuit" refers to the decomposition of a unitary operator, typically a component of a "quantum algorithm," into elementary gates that act on qubits [4]. This is analogous to an electronic circuit implementing a logical operation using elementary gates on charge-carrying wires.

Although the idea of applying a random series of operations in an electronic circuit or executing a random series of instructions on a classical computer may seem unusual, random quantum circuits have provided valuable insights into properties of quantum dynamics, such as information scrambling and entanglement spreading [5]. Moreover, while we would like to ultimately use a quantum computer to solve problems like factorization or to simulate quantum matter, the current limitations of hardware size and noise prevent those uses [6]. Meanwhile, random circuits have emerged as a promising tool to benchmark these near-term machines and

evaluate their capabilities.

On one front, random circuits are employed to benchmark quantum machines through randomized benchmarking [7]. The quality of a quantum operation is quantified by the "fidelity" between the target unitary it intends to apply and unitary it actually applies. Randomized benchmarking is used to estimate the fidelity of a gate for an average unitary, sampled from the Haar measure. Such a single measure of quality facilitates comparisons across different devices.

Likewise, random circuits have also been used to demonstrate the computational power of quantum computers. A random circuit induces a probability distribution on measurement outcomes of qubits, and it is believed that this distribution is difficult to sample from for a classical computer [8, 9]. Recent experiments have developed devices with a number of qubits large enough that they cannot be easily simulated on classical supercomputers [10, 11]. Proving that a quantum computer has sampled from a quantum distribution inaccessible to classical computers is considered a milestone in achieving quantum advantage [12]. The computational hardness of these tasks in noisy devices is currently an active area of research.

Beyond the utility of quantum computers as computational devices, they can also be regarded as a novel type of matter, where interactions can be engineered using gates [5]. A quantum circuit can be seen as implementing non-equilibrium dynamics, and the study of the resulting quantum states has revealed intriguing physics. For example, a new phase transition has been discovered to arise from the competition between entanglement-generating unitaries and entanglement-destroying measurements in a quantum circuit [13]. Furthermore, these new insights have led to surprising connections with well-established topics in statistical mechanics, such as percolation theory [14].

This dissertation aims to discuss specific instances of such phase transitions observed in monitored random circuits and to elucidate how the analytical and numerical tools used to study

random circuits can shed light on fundamental aspects of quantum information [15–17].

## 1.1 Preliminaries

A quantum circuit implements a unitary operation $U$ on a quantum state $|\psi\rangle$. In the context of this discussion, we assume that the quantum state is composed of qubits, each with a local Hilbert space dimension of two. The unitary $U$ is typically decomposed into a sequence of single-qubit and two-qubit gates: $U = G_T G_{T-1} \dots G_1$, where each gate $G_t$ acts on either a single qubit $i_t$ or a pair of qubits $(i_t, j_t)$.

The specific set of gates supported by a given quantum computer, also known as the "gateset", depends on the physical architecture or qubit design. A typical gateset may include single-qubit rotations of the form $\exp\left(i\theta\sigma_{x/y/z}/2\right)$, where $\sigma_x, \sigma_y, \sigma_z$ are Pauli matrices, together with a two-qubit entangling gate, like the CNOT gate. Furthermore, the connectivity of the quantum computer determines which qubits can be paired for a single interaction. For instance, an ion-trap computer with $n$ qubits may allow any $i_t, j_t \in n$, while a superconducting chip might only support interactions between neighboring qubits.

When investigating random circuits, we generate a random unitary $U$ on $n$ qubits by sampling local two-qubit gates from the 4-dimensional unitary group $\mathcal{U}(4)$. A commonly used model for random circuits, known as a brickwork circuit, is illustrated in Fig. 1.1A. In such circuits, at each step, a layer of two-qubit gates is applied in parallel to a subset of all available qubit pairings. Although we do not sample from $\mathcal{U}\left(2^n\right)$ directly, the statistical properties of random circuits with a depth of $\Omega(n)$ are indistinguishable from those of $\mathcal{U}(2^n)$. Specifically, random circuits with a brickwork architecture form unitary $t$-designs in depth $O\left(nt^{5+o(1)}\right)$ [18].

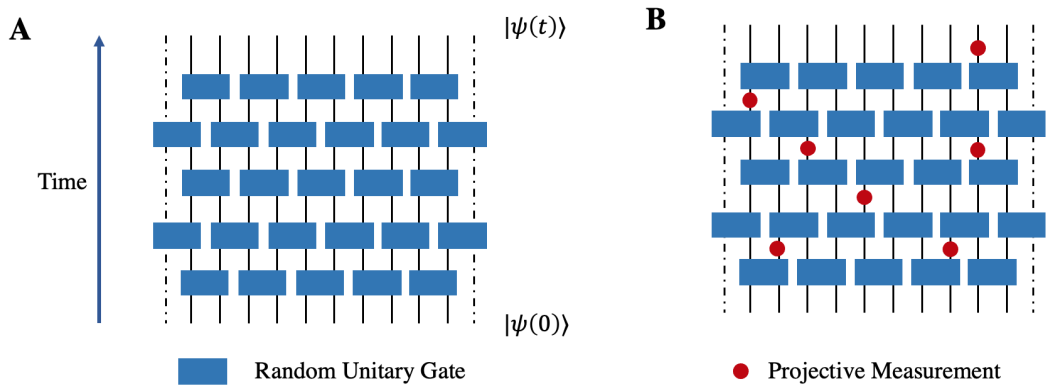


Figure 1.1: A) The brickwork model of random circuits in (1+1)D. Two-qubit unitaries are applied in layers on an initial state $|\psi(0)\rangle$. B) The brickwork model with interspersed projective measurements.

In monitored circuits, projective measurements are incorporated alongside unitary gates, as depicted in Fig. 1.1B. Without loss of generality, we focus on single-site measurements in the $Z$ basis, which yield outcomes $|0\rangle$ and $|1\rangle$. Each unitary gate $G_t$ maps the quantum state as $\rho \to G_t \rho G_t^\dagger$, while each single-qubit measurement stochastically transforms $\rho$ to $|0\rangle\langle 0|\rho|0\rangle\langle 0| / \mathrm{tr}(\rho|0\rangle\langle 0|)$ if the measurement outcome is $|0\rangle$, or $\rho \to |1\rangle\langle 1|\rho|1\rangle\langle 1| / \mathrm{tr}(\rho|1\rangle\langle 1|)$ if the outcome is $|1\rangle$. Consequently, when projective measurements are present in a circuit, the final state obtained depends on the measurement outcomes.

One use of random circuits is to investigate the growth and distribution of entanglement in quantum states during monitored dynamics. Given a density matrix $\rho$ on $n$ qubits, we can consider a subsection $A$ and its complement $\overline{A}$. The von Neumann entropy of subsection $A$ is given by $S_A = -\mathrm{tr}\,\rho\log\rho$. Similarly, the mutual information between $A$ and $\overline{A}$ is defined as $I_{A,\overline{A}} = S_A + S_{\overline{A}} - S_{A\overline{A}}$. Another entropy measure often employed, which admits helpful mappings to statistical mechanical models, is the Rényi entropy $R_\alpha = (1-\alpha)^{-1}\log(\mathrm{tr}\,\rho^\alpha)$, where $\alpha \in \mathbb{R}_{\geq 0}/\{1\}$ [14].

In random circuit sampling or randomized benchmarking, observables are selected to assess

how effectively a quantum computer can implement a target unitary or generate a target state. Randomized benchmarking is used to obtain quality measures for single-qubit and two-qubit gates. These measures are obtained by calculating the fidelity of a state after applying a series of gates. If the target state is a pure state $|\psi\rangle$ and the quantum device produces a mixed state $\tilde{\rho}$, the fidelity can be computed as $F(\tilde{\rho}, |\psi\rangle) = \langle\psi|\tilde{\rho}|\psi\rangle$. This often requires reconstructing the resulting density matrix through state tomography. However, in experiments such as random circuit sampling [10], performing complete state tomography on a large number of qubits is experimentally intractable. Therefore, a related measure called linear cross entropy (XEB) is commonly used:

$$\text{XEB}(\rho, \tilde{\rho}) = 2^n \sum_x p(x)q(x) - 1, \qquad \text{with} \quad p(x) = \langle x|\rho|x\rangle\,, q(x) = \langle x|\tilde{\rho}|x\rangle\,. \tag{1.1}$$

Both fidelity and linear cross entropy are second-moment quantities, which means they can be expressed as expectation values of two copies of the density matrix $\rho$:

$$\text{tr}(O\rho^{\otimes 2}) = \text{tr}\left(O(U \otimes U)(\rho(0) \otimes \rho_0(U^\dagger \otimes U^\dagger)\right), \tag{1.2}$$

where $O$ is a $4^n \times 4^n$ operator acting on the doubled Hilbert space, and $U$ is the unitary operator that acts on $\rho_0$ to generate $\rho$. This representation is useful for developing analytic and numerical techniques. Often, we are interested in calculating circuit-averaged expectations of $k$ copies of the density matrix $\rho$. In such cases, we may use the Schur-Weyl duality [19]:

$$\mathbb{E}_U(\rho^2) = \mathbb{E}_U(U^{\otimes k}\rho_0^{\otimes 2}(U^\dagger)^{\otimes k}) = \sum_{\Gamma \in S_k} a_k R(\Gamma), \tag{1.3}$$

where $S_k$ is the permutation group on $k$ elements, and $R(\Gamma)$ is the $(2^n)^k \times (2^n)^k$-dimensional representation of the permutation group. These identities can also be expressed as Weingarten integrals [20]. An immediate observation from (1.3) is that linear observables or single-copy expectations of random circuits converge to the same value proportional to $\mathrm{tr}(\mathbb{1})$, as the single-element permutation group only contains the identity element. For second-order observables, each randomized gate contributes an $I$ (identity element) or an $S$ (SWAP element), and the observable can be written as a partition function of a spin-$1/2$ Ising model [21]. These connections to Ising and Potts models have been instrumental in proving various theorems regarding the convergence of random circuits to unitary $t$-designs [18] or the rate at which the output of noisy quantum computers approaches the uniform distribution [22]. An example of such a calculation, where we compute the collision probability, $Z = \sum_{x \in X} p_x^2$, of a distribution $X$ induced by a noisy quantum circuit, is presented in Appendix A.

Analytic solutions are not always feasible for non-linear quantities such as von Neumann entropy. Therefore, we often resort to numerical simulations [5,23,24]. However, exact simulation of quantum dynamics is challenging. Storing and manipulating a generic quantum state over $n$ qubits requires memory resources that quickly become prohibitively expensive beyond around thirty qubits. As a result, various numerical tools have been developed to approximate quantum dynamics. Tensor network methods, for example, have seen widespread use and have become indispensable in the numerical investigation of quantum systems. These methods take advantage of the fact that many interesting quantum states are not highly entangled, allowing for a more efficient representation in computer memory [25–27]. However, tensor network methods encounter limitations when dealing with quantum states with a large amount of entanglement.

In certain cases, we can exploit the fact that not all quantum circuits are computationally

hard to simulate. Clifford circuits are quantum circuits constructed using only Hadamard (H), Phase (P), and CNOT gates, with the corresponding unitaries given by

$$H = \frac{1}{\sqrt{2}} \begin{pmatrix} 1 & 1 \\ 1 & -1 \end{pmatrix}, \qquad P = \begin{pmatrix} 1 & 0 \\ 0 & i \end{pmatrix}, \qquad \text{and} \qquad \text{CNOT} = \begin{pmatrix} 1 & 0 & 0 & 0 \\ 0 & 1 & 0 & 0 \\ 0 & 0 & 0 & 1 \\ 0 & 0 & 1 & 0 \end{pmatrix}. \tag{1.4}$$

The action of Clifford circuits on stabilizer states can be simulated exactly and efficiently using classical computers [28]. Such simulations have been useful in exploring properties of random circuits [23]. Certain properties, such as linear cross entropy and fidelities, are statistically equivalent for both the Haar ensemble and the Clifford ensemble.

## 1.2 Phase Transitions in Random Circuits

Phase transitions in random quantum circuits are best exemplified in models that incorporate a random sequence of gates interspersed with measurements, known as monitored quantum circuits (see Fig. 1.1B) [13, 23]. In this model, after each gate, a qubit is projectively measured with probability $p$. Each realization of the monitored random circuit generates a quantum state that depends on the outcomes of the randomly placed measurements, giving rise to different quantum trajectories.

The idea behind measurement-induced phase transitions is that the quantum trajectories separate into distinct phases as a function of the measurement rate $p$. This behavior is particularly evident in extreme cases. In the limit $p \to 1$, where qubits are measured after every gate, the

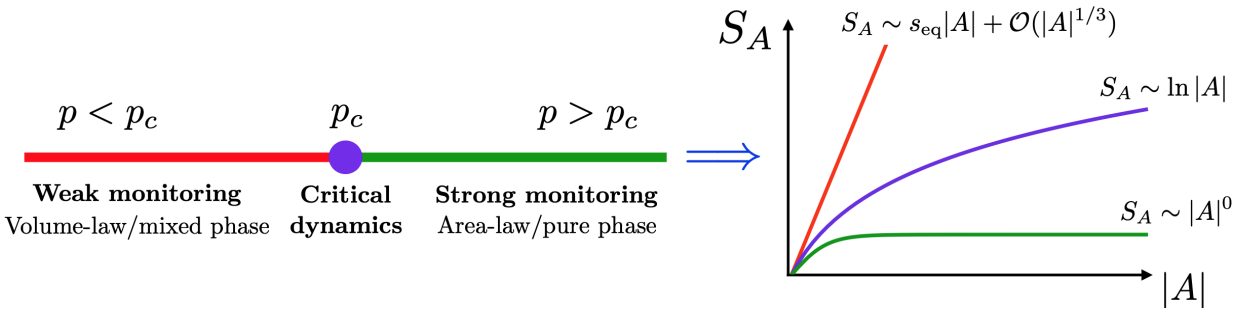


Figure 1.2: Schematic of a measurement-induced entanglement phase transition [5]. As a function of the measurement rate $p$, the von Neumann entropy of trajectories obtained with random circuits with interspersed measurements changes from one that grows with subsystem size $|A|$ to one that grows with the size of the boundary $|\partial A|$.

system remains in a product state without any entanglement. Conversely, in the limit $p \to 0$, the circuit is unaffected by measurements, and the entanglement of a subsystem $A$ grows linearly in time, eventually saturating to a value proportional to the volume (or size) of the subsystem $|A|$.

It has been shown that the two phases are separated by a sharp phase transition occurring at a critical point $p_c$ [13]. For $p < p_c$, the entanglement entropy in the subsystem increases with the volume $|A|$; this phase is referred to as the "volume-law phase". On the other hand, for $p > p_c$, the entanglement entropy grows with the size of the boundary of the subsystem $|\partial A|$; this phase is known as the "area-law phase". At the critical point $p = p_c$, the entanglement entropy exhibits logarithmic growth, proportional to $\ln|A|$. A schematic illustration of the two phases and their entanglement properties in (1+1)D is presented in Fig. 1.2.

Such a phase transition in $(d+1)$-dimensional monitored circuits has been observed for $d = 1, 2$, and 3 in various models of random circuits [23, 24]. Numerical simulation of the Clifford ensemble has allowed for the investigation of this transition in large system sizes, on the order of thousands of qubits [23,29]. Moreover, in certain limits, this transition can be mapped to well-known problems in statistical mechanics. For instance, in the limit where the local Hilbert space dimension $q \to \infty$ (with $q = 2$ for qubits), the calculation of Rényi entropies of quantum

states subjected to monitored circuits in $(1+1)$D can be mapped to the percolation problem in two dimensions [30]. Furthermore, evidence suggesting that these transitions in the Clifford and Haar ensembles belong to distinct universality classes, different from the percolation transition, indicates that this transition exhibits rich and diverse properties that can be further understood through probes beyond entanglement entropy.

A complementary perspective on the transition between the area- and volume-law entangled phases is provided by the concept of the dynamical purification transition [31, 32]. Consider a maximally mixed initial state over $n$ qubits, given by $\rho(0) = \mathbb{1}/2^n$, subjected to random unitary dynamics and measurements at a rate $p$. For any measurement rate $p$, the system purifies into a pure state at a time exponential in $n$ (for example, when an event occurs where all qubits are measured, which has a wait time $\propto 1/p^n$). It has also been observed that, below a critical threshold $p_c$, the system purifies at a rate independent of the system size. The two phases, one with system-size-independent purification time and another with purification time diverging exponentially in $n$, are referred to as the "pure phase" and the "mixed phase," respectively. These phases correspond to the area-law and volume-law phases of the entanglement phase transition.

The dynamical purification transition can be interpreted through the lens of quantum error correction [33]. The quantum entropy of a state can be seen as the amount of unknown information in the system. In the "pure phase," local projective measurements rapidly reduce the entropy of the system. In the "mixed phase," the system retains finite entropy for evolution times polynomial in the system size. This indicates that random unitary circuits enable an error correction code resilient to local noise.

This perspective of dynamical purification also provides a natural means to probe the transition. We can consider a reference system that is maximally entangled with the initial

state. As the combined system evolves, the original system either purifies, removing any residual entropy between the original system and the reference, or it remains entangled with the reference. By measuring the entropy of the reference, we can gather information about the original system. Notably, it has been demonstrated that even a single qubit can serve as a reference to probe the transition, eliminating the need for expensive state tomography of the entire system [34]. This forms the basis of the experiment discussed in Chapter 2.

While entanglement is a valuable property of quantum states, it alone cannot enable universal quantum computation [17, 35]. One measure that quantifies the usefulness of a quantum state for universal quantum computation is "magic" [36, 37]. A phase transition in magic, as a function of resources that introduce non-classicality to a stabilizer quantum state (such as T gates [38]), would imply phases where the degree of non-stabilizer nature is either suppressed or amplified. However, unlike entanglement, which can be studied using Clifford circuits, numerical and experimental investigations of magic remain challenging [39]. An experimental probe of a phase transition in magic is the focus of Chapter 3.

Recently, the concept of phase transitions has also emerged in the context of random circuit sampling. While fidelity is a natural measure for quantifying the performance of a quantum computer, it can be challenging to measure in experiments [40]. Consequently, experiments have employed a related measure called linear cross entropy (defined in (1.1)) as an alternative [10]. However, it has recently been discovered that linear cross entropy might not always serve as a good proxy for fidelity in noisy systems [41]. For noisy quantum devices with a local noise rate of $\epsilon$, it has been demonstrated that the discrepancy between fidelity and linear cross entropy manifests as a phase transition with respect to $\epsilon n$, where the correspondence abruptly breaks down at a certain critical value [22].

Finally, random circuits have also been utilized to explore methods for protecting quantum information from noise, such as error correction or error mitigation. In error correction, syndrome measurements and decoding techniques are used to suppress errors. While error correction in a quantum computer requires the costly overhead associated with fault-tolerance, lightweight protection against noise can be achieved through error mitigation [42]. In Chapter 4, we demonstrate how the statistical mechanical mappings employed in random circuits can establish the existence of a threshold for error mitigation.

## 1.3 Outline of the Thesis

The remainder of the thesis is structured as follows. In Chapter 2, we present an experimental realization of an entanglement phase transition on a trapped-ion quantum computer. Chapter 3 discusses a novel phase transition in magic, a measure associated with universal quantum computation, and its experimental observation. In Chapter 4, we present a discussion on error mitigation thresholds obtained through numerical and analytical methods applied to random circuits. Supporting material for all chapters is included in the appendices.

## List of Previously Published Works

The following works, either published or appearing in preprint journals, are discussed in this thesis:

- Chapter 2. Noel, C., Niroula, P., Zhu, D., Risinger, A., Egan, L., Biswas, D., Cetina, M., Gorshkov, A.V., Gullans, M.J., Huse, D.A. and Monroe, C., 2022. Measurement-induced quantum phases realized in a trapped-ion quantum computer. Nature Physics, 18(7), pp.760-764.

- Chapter 3: Niroula, P., White, C.D., Wang, Q., Johri, S., Zhu, D., Monroe, C., Noel, C. and Gullans, M.J., 2023. Phase transition in magic with random quantum circuits. arXiv preprint arXiv:2304.10481.

- Chapter 4: Niroula, P., Gopalakrishnan, S. and Gullans, M.J., 2023. Error Mitigation Thresholds in Noisy Quantum Circuits. arXiv preprint arXiv:2302.04278.

Other related publications, mentioned in the introductory chapter, but not described in subsequent chapters:

- Deshpande, A., Niroula, P., Shtanko, O., Gorshkov, A.V., Fefferman, B. and Gullans, M.J., 2022. Tight bounds on the convergence of noisy random circuits to the uniform distribution. PRX Quantum, 3(4), p.040329.

- Ware, B., Deshpande, A., Hangleiter, D., Niroula, P., Fefferman, B., Gorshkov, A.V. and Gullans, M.J., 2023. A sharp phase transition in linear cross-entropy benchmarking. arXiv preprint arXiv:2305.04954.

# Chapter 2: Measurement-Induced Purification Phase Transition

## 2.1 Introduction

Many-body open quantum systems balance internal dynamics against decoherence and measurements induced by interactions with an environment [43,44]. Quantum circuits composed of random unitary gates with interspersed projective measurements represent a minimal model to study the balance between unitary dynamics and measurement processes [45–47]. As the measurement rate is varied, a purification phase transition is predicted to emerge at a critical point akin to a fault-tolerant threshold [48]. Here, we explore this purification transition with random quantum circuits implemented on a trapped-ion quantum computer. We probe the pure phase, where the system is rapidly projected to a pure state conditioned on the measurement outcomes, and the mixed or coding phase, where the initial state becomes partially encoded into a quantum error correcting codespace that keeps memory of initial conditions at long times [48,49]. We find experimental evidence of the two phases and show numerically that, with modest system scaling, critical properties of the transition emerge.

An isolated many-body quantum system undergoes unitary evolution until it is probed by its environment via quantum measurement [43, 44]. The irreversible process of measurement converts quantum coherence in the system into classical entropy in the measurement apparatus due to the intrinsic randomness of quantum measurements. When the rate of partial measurements

is high, this process "collapses" the many-body system into a pure quantum state consisting of locally correlated regions determined by the recent unitary dynamics and measurement outcomes. At low measurement rates, however, there is a mixed (coding) phase where the associated projections can leave invariant a codespace in the system that retains memory of initial conditions for exponentially long times [48,49]. Such measurement-induced phase transitions have recently been theoretically explored in models based on random quantum circuits [45–49], but are believed to be a ubiquitous phenomenon in monitored non-equilibrium quantum systems. The theory of these transitions, although still nascent, has seemingly deep connections to percolation and conformal field theory [45, 47, 50, 51], as well as threshold theorems in fault-tolerant quantum computing [52, 53]. Observing these effects in experiment is a formidable challenge because measuring the observables that signify the transition requires exquisite control and isolation of the system, accurate monitoring by an external measurement apparatus, and the use of sophisticated feedback or post-processing with the measurement data.

Here, we report on a direct experimental observation of the two phases associated with a measurement-induced purification transition in a trapped ion quantum computer. We use a single reference qubit initially entangled with the system to directly test for the existence of the codespace in the mixed phase and its absence in the pure phase [34]. This approach has the practical benefit that it relaxes experimental resource requirements compared to observables that require measuring entanglement entropies of large numbers of qubits, such as measuring Renyi entropy [54]. We avoid the use of post-selection on measurement outcomes through the addition of feedback operations that reverse any measurement-induced unitary rotations on the reference qubit (i.e., so-called "quantum steering" effects [55]). As a result, absent noise, our experimental approach is directly scalable to large systems.

From early measurements of the quantum-to-classical nature of measurement in ion trap systems [56] and cavity quantum electrodynamics [57], to the recent observation of wavefunction collapse in superconducting qubits [58], the phenomenon of measurement itself has been a subject of great interest experimentally. Many-body coherent operations combined with controlled dissipation or measurements have been explored experimentally in, for example, the study of dissipative state preparation [59], as well as in recent theoretical proposals for many-body quantum non-demolition measurements [60]. We also note related experimental results showing symmetry resolved dynamical purification of spin chains in a long-range $XX$ model with local depolarizing noise [54, 61]. By contrast, in our study, we employ a "digital" model of computing with two-site unitaries and projective measurements with a temporal randomness to the dynamics.

## 2.2 Experimental Platform

Our quantum computer uses up to 13 $^{171}\mathrm{Yb}^{+}$ qubits in a single chain of 15 trapped ions in a microfabricated chip trap [62]. We achieve a universal gate set with native single-qubit gate fidelities of 99.96% and two-qubit gate fidelities on any pair of 98.5-99.3%, as detailed elsewhere [63].

## 2.3 Random Circuit Model

Since ion-traps allow for all-to-all connectivity, we use that. We now describe the specific dynamics of the random circuits in this work with a system of $L$ qubits subject to unitary evolution with all-to-all connectivity and measurements. For such all-to-all coupled models, spatial entanglement of the wavefunction is not a reliable diagnosis of the measurement-induced

phase transition; instead we characterize the problem in terms of a purification transition [48]. In this picture, the system transitions at low measurement rates to a phase with long-range correlations in time, similar to the behavior found in fault-tolerant error correction thresholds. This dynamical purification phase transition can be efficiently probed by studying how the system preserves entanglement over time with a single reference qubit [34].

An example circuit is shown in Fig. 2.1A. After preparing all qubits in $|0\rangle$, the reference is entangled to a randomly selected system qubit to form a Bell pair. The entangling operation is followed by a scrambling unitary, which consists of random single-qubit Clifford gates and two-qubit $XX(\pi/4)$ gates on random qubit-pairs. The scrambling stage, spreads the entanglement to the entire system and reduces finite-size effects. An example of the scrambling circuit is shown in Fig. 2.2 After scrambling the system qubits, we evolve the system in time with random unitary dynamics and measurements with a total number $N_g = \lfloor L\sqrt{L} \rfloor$ of $XX(\pi/4)$ gates applied to randomly chosen qubit pairs.

After each entangling-gate we add a measurement with probability $p$ (See Appendix B.1 for details on how measurements are added). While mid-circuit readout of ion qubits is possible [64], we use ancilla qubits to defer readout. When a circuit calls for measurement, we entangle that qubit with an ancilla in a chosen measurement basis. Because the unitaries are XX gates, the measurement choice of the $z$ or $x$ basis has a strong effect on the subsequent dynamics. This feature of our model allows us to tune the probability, $p_x$, that a measurement is in the $x$ basis to go across the purification transition without directly changing $p$. At the end of the circuit, all the qubits are read out in the $z$-basis via fluorescence imaging. For each circuit, we rotate the reference qubit to measure in $x$, $y$ and $z$-basis and post-select the observations to obtain Pauli expectations conditioned on measurement outcomes. The set of three Pauli expectations

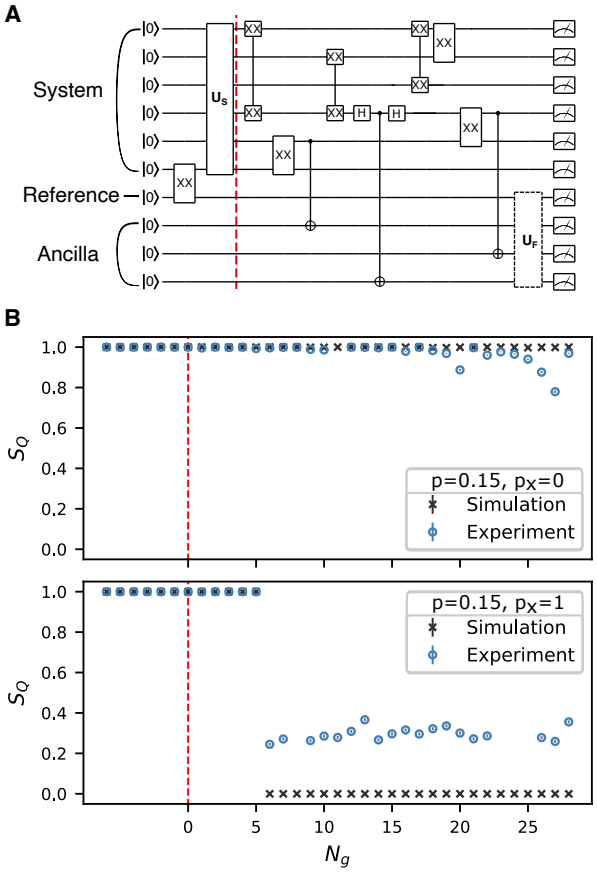


Figure 2.1: **Model and Purification Dynamics** (A) Schematic of a circuit with $L = 6$ system qubits, $N_g = 6$ two-qubit gates, 2 $z$-measurements and 1 $x$-measurement. The first XX gate entangles the reference with a system qubit. Next, we scramble the system, $U_S$. The time evolution of the unitary-measurement dynamics starts at the red dashed line. Probabilistic measurement is deferred until the end of the circuit using CNOT gates between system qubits and measurement ancillae. The x-basis measurement is shown after the third $XX$ gate. Finally, a feedback operation $U_F$ is applied (see Appendix B.4) (B) The entropy of reference qubit for two $L = 6$ circuits where the reference qubit stays mixed (upper panel) and purifies (lower panel). The $x$-axis shows the evolution of time in units of applied two-qubit gates ($N_g$) after scrambling is complete (indicated again by the red dashed line). In this example, the entropy is measured by performing single-qubit tomography of the reference by making measurements in the $x$, $y$ and $z$-basis. Error bars ($1\sigma$) are smaller than the markers, with 4000 and 10000 shots for experiment and simulation, respectively. Missing experiment data are due to ion loss events, which are assumed to be uncorrelated with the data being taken.

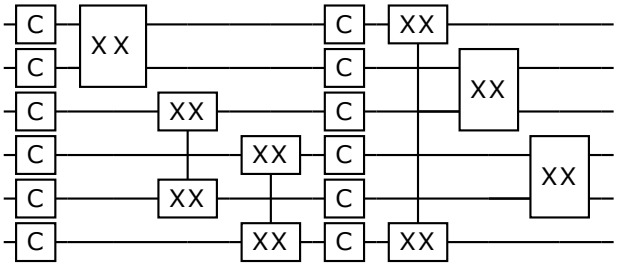


Figure 2.2: Example of a scrambling unitary on a system with $L = 6$ qubits. Each single-qubit gate $C$ refers to a random single-qubit Clifford gate. The $XX$ gates have an implied rotation angle of $\pi/4$

are then used to construct the density matrix of the reference qubit and measure its entropy $S_Q$. These circuits are examples of stabilizer circuits, whose noiseless dynamics are classically simulable [65, 66].

As an illustrative example, in Fig. 2.1B, we consider the experimentally measured evolution of $S_Q$ in two circuits sampled from ensembles with $p = 0.15$. We choose one circuit sampled from $p_x = 0$ that stays mixed (encoded) and one sampled from $p_x = 1$ that purifies over time. Units of time are measured in number of applied two-qubit gates, $N_g$, for consistency between theory and experiment. For noiseless stabilizer circuits, the entropy is always either 0 or 1 bit [47, 66], and, as a result, the circuits that purify must do so at precisely one time step. However, this property no longer holds exactly in the presence of noise. Experimentally, we find that the mixed circuit maintains a high value of $S_Q$. In the second circuit, the reference qubit purifies at the expected time in the circuit, albeit to a constant offset due to experimental noise. It is apparent from these examples that we observe a clear separation between pure and mixed results for $S_Q$. For each circuit, we ran 4000 shots of each measurement basis $(x, y, z)$ to compute $S_Q$ at each time step.

In order to characterize the many-body dynamics, we generate large ensembles of circuits and average their entropy for given values of $p$, $p_x$, and $L$. In Fig. 2.3A, we show the theoretical

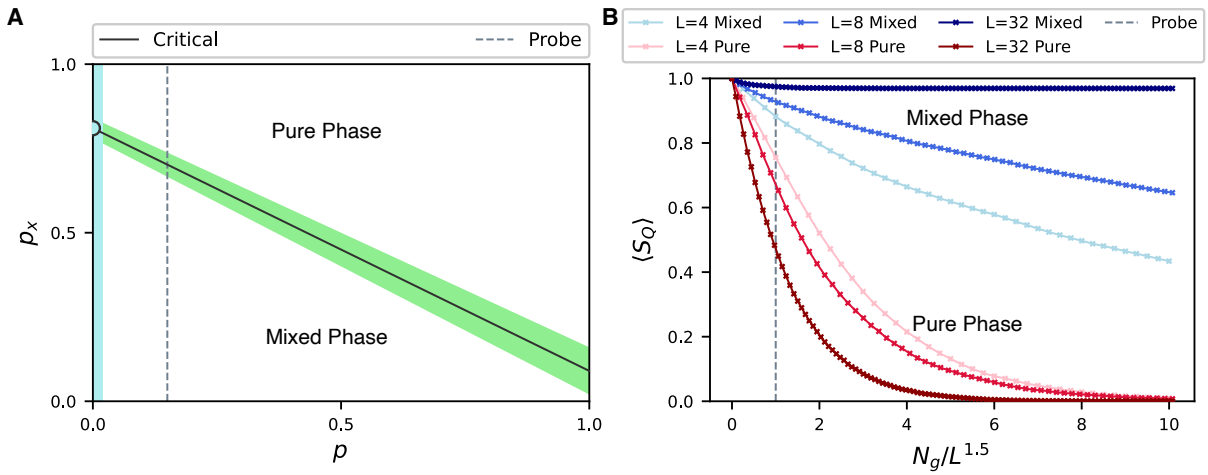


Figure 2.3: **Phase Diagram and Scaling Limit of Average Purification Dynamics** (A) The phase diagram of the model, parameterized by $p$ and $p_x$. The green shaded region indicates the numerical uncertainty in the critical region between the top phase where the reference qubit rapidly purifies, and the bottom phase where it stays mixed. In our experiment, we fix $p = 0.15$, and tune $p_x$ to probe the phase transition along the dashed line. In the limit $p \to 0$ (left blue shaded region) with time also scaled as $1/p$, our model becomes a measurement-only model [67]. A purification transition (circle) arises in this limit when tuning $p_x$ along the line $p = 0^+$. (B) The simulated entropy of the reference qubit averaged over many random circuits $\langle S_Q \rangle$ in the two phases. Here, we use the same fixed value of $p = 0.15$ from A, with $p_x = 0$ (mixed) and $p_x = 1$ (pure) plotted against time (measured in units of two-qubit gates) scaled by $L^{1.5}$. The dashed vertical line indicates the experimental probe time of $N_g = L^{1.5}$, and the intersection of this line with different system sizes shows increasing (decreasing) entropy in the mixed (pure) phase that is the signature of the two phases.

phase diagram for the model vs $p$ and $p_x$. For low $p$ and $p_x$, the system is driven to a mixed (coding) phase where the non-unitary dynamics projects quantum information about the initial state into a random quantum error correcting code. As either $p$ or $p_x$ is increased, the system enters a pure phase, where an initial mixed state collapses to a fixed quantum state and the encoding operation fails. The behavior at $p = 0$ can be smoothly connected to the finite $p$ behavior by scaling $N_g$ by $1/p$ and taking the limit $p \to 0$. In this limit, there is residual purification dynamics that leads to a phase transition along the $p = 0^+$ axis. This special critical point arises because of the restricted nature of our gates that do not effectively scramble the system in the absence of measurements [67]. The critical point at each value of $p$ was obtained from finite-size scaling analysis using simulations of $L = 16$ to $L = 64$ qubits (Appendix B.5). Our scaling analysis is based on extracting the exponential decay rate of $\langle S_Q(t) \rangle$ at late times.

In Fig. 2.3B, we show the simulated dynamics of $\langle S_Q(t) \rangle$ at two representative points in the phase diagram with $p = 0.15$. In the mixed phase, probed at $p_x = 0$, $\langle S_Q \rangle$ stays near one for exponentially long times in $L$. Deep in the pure phase, the reference qubit rapidly purifies, with an average entropy that exponentially approaches zero. In the experiment, we probe small systems $L \leq 8$ after a number $L^{1.5}$ of gate operations. For larger numbers of qubits $L$, this scaling limit is sufficient to probe the phase because the effective depth of the circuit scales as $2\sqrt{L}$, much greater than any fixed correlation time in the system. At the critical point, as we show in the Appendix B.5 Fig. B.5, the entropy decay time scales as $L^{1/5}$ to conform to the universal critical dynamics of the system.

This feedback approach avoids postselection and remains tractable for stabilizer circuits on any system size because we can efficiently find the feedback circuit [65]. Finding efficient extensions of this feedback approach for arbitrary gate sets and circuit architectures is an unsolved

problem [34]. Many of the naive approaches to investigating the phase transition for random circuit ensembles with a universal gate set requires some form of post-selection on the measurement outcomes. It is therefore an important goal to develop efficient feedback protocols (or other methods to circumvent post-selection) for generic random circuit models. Alternatively, it may be possible in some cases to give complexity theoretic evidence that an efficient feedback protocol does not exist.

To probe the phases experimentally, we generate an ensemble of random circuits for the chosen values of $p$, $p_x$, and $L$. To constrain the number of measurements to a low value, we study a fixed line of parameters at $p = 0.15$ (Fig. 2.3A), and the evolution is applied for a time $N_g$. At the end of the circuit, we measure the reference in the $z$-basis. We average over many shots to determine $S_C$ for each circuit. The majority of experimental noise can be explained with a simple noise model using XX-gate crosstalk. (See Appendix B.6 and B.7, where we also describe techniques to further mitigate errors). We assume a Gaussian distribution of expected $S_C = 0$ circuit outcomes and $S_C = 1$ circuit outcomes and find their intersection, which is used as a threshold at $S_C = 0.93$ (Appendix B.3 Fig. B.1, and Fig. B.2). Any outcome below the threshold is counted as $S_{C,T} = 0$, and those above as $S_{C,T} = 1$. For $p_x = 0, 1$ ($p_x = 0.5$), we average the entropy after binning with the threshold, $\langle S_{C,T} \rangle$, over the results of 300 (100) unique circuits.

We study $\langle S_{C,T} \rangle$ at $p_x = (0, 0.5, 1)$ and $L = (4, 6, 8)$, and observe the first experimental evidence of the phases of a dynamical purification phase transition. While the measured entropy increases with system size in the mixed phase ($p_x = 0$), in the pure phase ($p_x = 1$), the entropy decreases with system size (Fig. 2.4A). This behavior is expected and can readily be seen in simulations at the experimental probe time in the example in Fig. 2.4B. To probe the

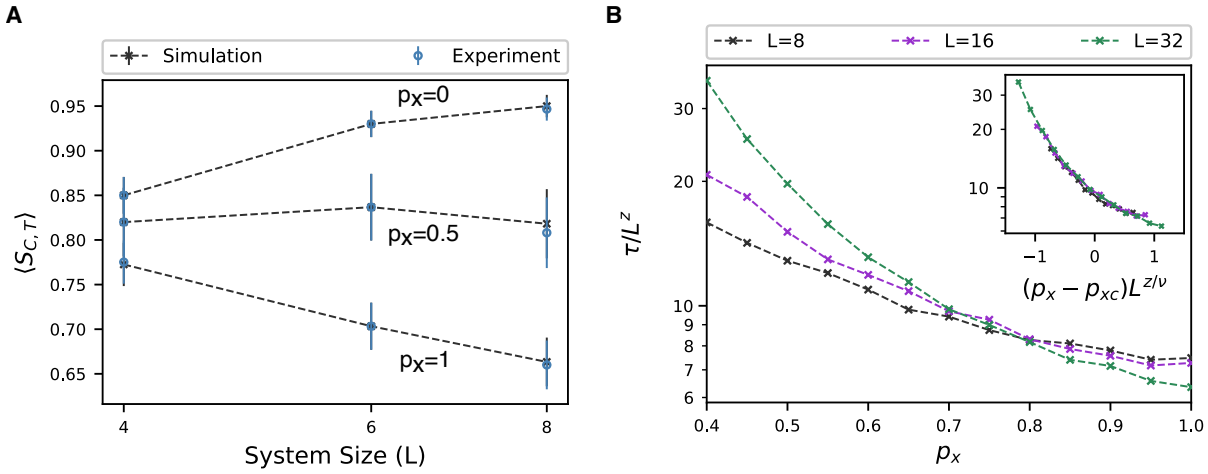


Figure 2.4: **Experimental Observation of Phases and Simulated Critical Behavior** (A) Classical entropy after thresholding $\langle S_{C,T} \rangle$ averaged over an ensemble of random circuits at varying system sizes. We show evidence of mixed (top), intermediate (middle), and pure phase (bottom) with $p_x = 0$, $p_x = 0.5$, and $p_x = 1$ respectively with size-scaling as predicted in Fig. 2.3. Error bars are $1\sigma$ uncertainty with 300 circuits for $p_x = 0, 1$ and 100 circuits for $p_x = 0.5$ (B) Simulated results showing the late-time decay rate $\tau$ of $\langle S_Q \rangle$ near the transition. Here, $z \approx 1/5$ is the dynamical critical exponent, $\nu \approx 1/2$ is the correlation length exponent, and $p_{xc} = 0.72(1)$ is the critical value of $p_x$. These critical parameters are extracted from a finite-size scaling analysis (see Inset and Appendix B.5).

crossover behavior on these system sizes, we also sample at an intermediate value of $p_x = 0.5$ close (for these sizes) to the critical point at $p_{xc} = 0.72(1)$. We observe consistent results with the simulations in this near-critical regime, showing behavior that interpolates between the two extremes.

## 2.4 Outlook

Having obtained conclusive evidence for the two phases in our system, it remains an outstanding challenge to experimentally probe the universal critical behavior of this model. We predict that such effects will become accessible in our system through modest increases in system sizes from $L = 8$ to $L = 32$ qubits combined with periodic sympathetic cooling [68], which enables mid-circuit measurements, improves fidelties at late times, and should allow for deeper

circuits. We have found that a sensitive probe of the critical properties of the purification transition is the late-time exponential decay constant $\tau$ of the order parameter $\langle S_Q(t) \rangle \sim e^{-t/\tau}$. Fig. 2.4B shows an example of a finite-size scaling analysis that can be used to extract critical properties of the model. Here, we use direct simulations of the ideal circuit evolution to predict the behavior of our system as it is scaled to larger sizes. Crucially, these scaling results illustrate that the critical properties of the purification transition are obtainable using the modest systems sizes and circuit depths accessible in near-term ion-trap hardware.

Our results show that measurement-induced quantum phases are accessible in near-term quantum computing systems despite the formidable experimental challenges. Recent years have seen a host of advances in mapping out the phenomenology of these novel nonequilibrium phases of matter, including the prediction of topological order stabilized by measurements in random circuits [67, 69, 70] and applications in computational complexity theory [71] and quantum error correction [72]. These developments point to a broad potential for the advancement of many-body physics and quantum information science through the continued explorations of quantum measurement.

From the perspective of fault-tolerant quantum computation, our results open up a number of new directions. Investigating similar physics in fault-tolerant operating regimes with error correction and feedback built into the model is an exciting direction for future work. Although the resource demands are often difficult to satisfy for fault-tolerant simulations, the intrinsic flexibility in implementing random circuit models allows one to circumvent the worst-case behavior analyzed in fault-tolerant threshold theorems [53]. As a result, many of the resource costs for fault-tolerance can be lowered for random circuits. For example, much of the overhead in the standard models for fault-tolerance arise from implementing a universal gate set. We have shown

that measurement-induced phase transitions are experimentally accessible with discrete gate sets like the Clifford group, which have efficient fault-tolerant transversal implementations in systems with long-range interactions, such as ion traps. Additional gates outside this set can be introduced with a low-density to avoid a large increase in the overhead for more generic random circuit models.

An important conceptual aspect of our work is that we experimentally study an error correction threshold as a physical phenomena, exploring its connections to universality in quantum many-body physics. This approach contrasts with many prior works on experimental quantum error correction that have so-far focused primarily on demonstrations of few-body gadgets in the below-threshold regime [63]. In addition, while error correction thresholds can be studied numerically, applying those theories in practice requires a deeper understanding of the errors in real physical systems, and how the corresponding thresholds behave. The ability to successfully operate quantum computing systems in these near-critical regimes is likely to be a crucial aspect in the future of fault-tolerant quantum computing.

# Chapter 3: Phase Transition in Magic

## 3.1 Introduction

A central goal in physics and computer science is to understand the origins of possible computational speedups of quantum information processors over their classical counterparts. Entanglement is a central resource for fault-tolerant quantum computing, but it is not necessarily sufficient to realize computational speedups. The notion of entanglement must be extended to distinguish between the production of "easy" and "hard" quantum states by fault-tolerant operations. Notably, even when the quantum state of the processor is highly entangled, computations consisting of only Clifford gates —a finite, non-universal subgroup of the unitary group —applied to stabilizer states, or eigenstates of Pauli operators, can be efficiently simulated on classical computers [73, 74]. Non-stabilizer input states or non-Clifford gates, by contrast, are believed to be exponentially difficult to simulate on classical computers [75, 76]. On quantum computers non-Clifford gates are easy, however, in the context of error-corrected quantum computer, these states and operations still require costly magic state distillation or other gate-intensive protocols [38, 77–79].

A resource theory of stabilizer computation has emerged [36] to study this division between easy (Clifford) and hard (non-Clifford) gates. In this theory, *magic* is the resource that enables universal quantum computation; the amount of magic in a state determines how useful it is as

a non-stabilizer input state in fault-tolerant synthesis of non-Clifford operations. Magic has been used to bound quantum complexities [80] and to constrain tensor network models of AdS-CFT [81]. Magic-generating non-Clifford operations have also been shown to be necessary for simulating quantum chaos [37]. Understanding the mechanisms by which magic can be generated or suppressed in a quantum circuit is, therefore, necessary not only to accelerate progress towards universal quantum computing but also to understand the limits in which quantum computations become classically accessible.

A related aspect of quantum entanglement is its behavior in monitored quantum circuits, such as measurement-induced entanglement phase transitions [13,23]. Monitored quantum circuits consist of local gates (or time evolution), interspersed with some rate or density of projective measurements. The simplest example of a monitored quantum circuit is the error correcting code: the state undergoes a series of entangling "encoding" unitaries, followed by projective syndrome measurement and final logical "decoding" unitaries [82]. In general, monitored quantum circuits can display a *measurement-induced phase transition in entanglement*. These systems display evidence of a complicated phase diagram determined by the details of the circuit [5, 83–85], and have connections to percolation theory [13, 86], the theory of stabilizer codes [31], and statistical mechanics models [14, 30, 32, 87]. Such hybrid circuits have also been shown to exhibit related phase transitions beyond entanglement [88].

In this paper, we show that measurement-induced phase transitions of entanglement can be extended to magic, and we study the transition experimentally. A quantum error correcting code subject to coherent errors displays a phase transition in the magic as a function of the number of logical qubits (which in our model sets the measurement rate) or the error rate. In the magic phase transition, syndrome measurements, which can destroy magic, compete with errors, which

can create magic, just as local dynamics and local measurement compete in the entanglement transition. For large error rate or infrequent measurements, the encoded state has extensive magic, while for low error rate or frequent measurements, the encoded state has nearly zero magic; the two regimes are separated by a phase transition. A brief overview of our setup is sketched in Fig. 3.1A and B and the resulting phase diagram is given in Fig. 3.1C. We also introduce a new measure of magic, the basis-minimized measurement entropy. We measure this quantity and another known measure of magic, the stabilizer Rényi entropy [89], in classical simulations, analytical calculations, and experiments on IonQ's Aria trapped-ion quantum computer. The magic phase transition is visible as a finite-size scaling collapse in these measures.

## 3.2 Random Circuit Model

We study magic in random Clifford codes. The initial state is a product state of $N$ qubits, $|0\rangle^{\otimes N}$. A randomly drawn Clifford circuit $C$ is applied to this state. This Clifford circuit maps the initial state to the logical space of a random Clifford code; such codes are known to make high-performing error correcting codes [90]. After the encoding circuit $C$, a single-qubit rotation $R_z(\alpha) = \exp(-i\sigma_z\alpha/2)$ is applied to each qubit. This "noise layer" models coherent noise and takes the quantum state away from the codespace of the Clifford code. We call $\alpha$ the *error rate*. The noise layer is followed by $C^\dagger$, the conjugate of the encoding circuit. Finally, $N-K$ qubits are measured in the computational basis, leaving a logical state with $K$ qubits. These $N-K$ measurements are syndrome measurements for the Clifford code.

The encoding Clifford circuits are generated by interweaving $d$ layers of single-qubit unitaries and $d$ layers of two-qubit Clifford unitaries (Fig. 3.1A). The odd layers are single-qubit gates

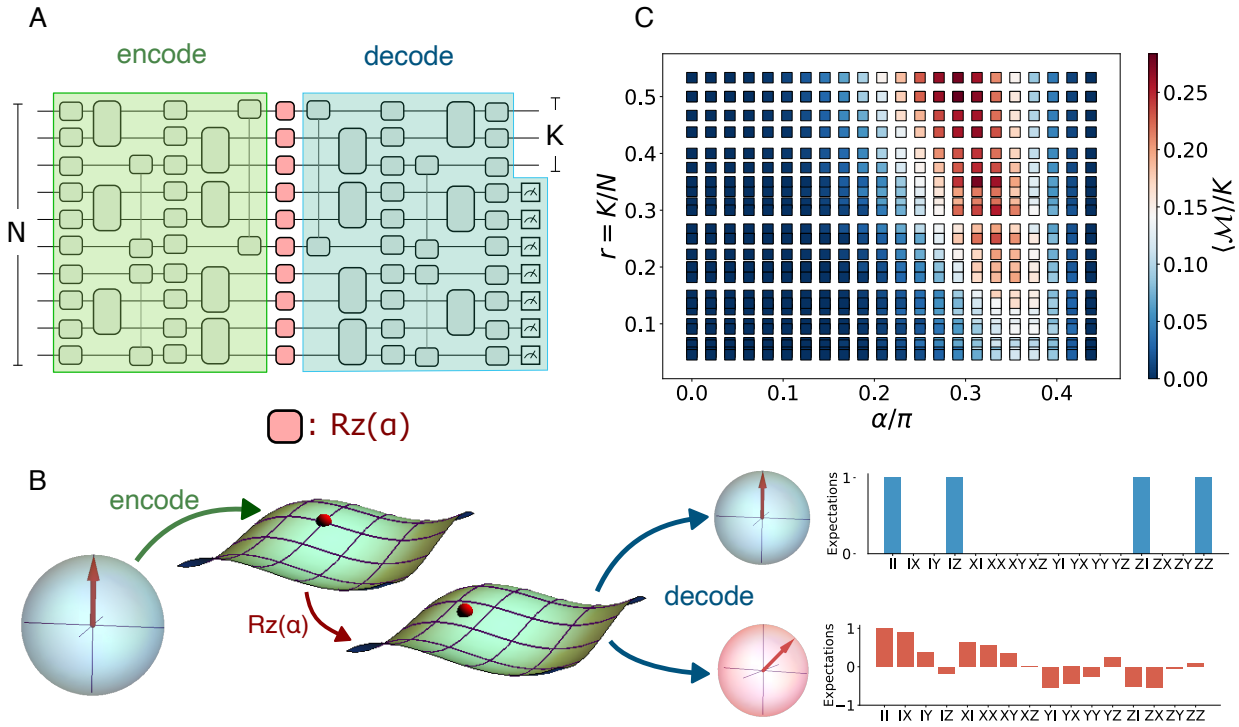


Figure 3.1: **Model and phase diagram**. **A**: The model. The qubits start in an all-zero state, corresponding to a logical 0 state. We apply a random Clifford encoding circuit (green), controlled "error" unitaries (red), and the conjugate of the encoding circuit (blue). **B**: A schematic illustration of how magic is created or destroyed in our model. The encoding step acting on an input stabilizer state (represented by a blue Bloch sphere) produces a highly entangled stabilizer state in the many-qubit Hilbert space. Coherent rotations move the state off the grid of stabilizer states. The decoding step either snaps the state back to the grid of stabilizer states or pushes the state away from that grid. The final state is either a multi-qubit stabilizer state, represented by a Bloch sphere shaded blue, or a magical state, represented by a Bloch sphere shaded red. The Pauli expectations of the resulting stabilizer (magical) state are shown as histograms shaded blue (red). **C**: Phase diagram for constant-rate codes. The color bar represents the magic density at a particular code-rate $r$, given by the ratio of logical qubits $K$ and total number of qubits $N$, and error rate, defined to be the angle of coherent rotation, $\alpha$.

sampled uniformly from the 24 elements of the single-qubit Clifford group. The even layers consist of fixed-angle ($\pi/2$) entangling Mølmer-Sørensen gates, defined as $\mathrm{MS}(\pi/2) = e^{i\pi XX/4}$, applied to $N/2$ randomly chosen disjoint pairs. The decoding circuit is the inverse of the encoder. We take $d = N$ in numerics and $d = N/2$ in experiment to reduce the effects of noise. Circuits with $d = N/2$ have a behavior similar to those with depth $d = N$. In Appendix C.4, we present numerics on $d = N/2$ and $d = 2N$ circuits.

Fig. 3.1B illustrates how magic is created or destroyed in our model. The state begins as a logical stabilizer state. The Bloch sphere, shaded blue, represents a multi-qubit stabilizer state. The encoding step maps the state to a stabilizer state in a many-qubit Hilbert space, and error moves the state off the grid of stabilizer states. The decoding (conjugate of the encoding operator together with syndrome measurements) step either snaps the state back to the grid of stabilizer states or pushes the state away from that grid; in either case it projects the state back to the logical space. The final state is either a multi-qubit stabilizer state, represented by a Bloch sphere shaded blue, or a magical state, represented by a Bloch sphere shaded red. The stabilizer-ness of a state is visible in the Pauli expectations. For a stabilizer state, the distribution of expectations is concentrated among the stabilizing Paulis, as shown in the histogram shaded blue for a representative two-qubit stabilizer state. For a Haar state, the distribution has support over all Paulis, as shown in the histogram shaded red for a representative two-qubit Haar state.

We study this transition for two different code rates (The code rate is the ratio of the number of logical qubits to underlying physical qubits.) The first case, which we refer to as "vanishing rate", has only one logical qubit, so the code rate $r = 1/N$ tends to zero for large $N$. The second case uses constant-rate codes with the scaling $K = rN$ logical qubits for a fixed code rate $r$.

## 3.3 Quantifying magic

Any measure of magic for pure states is a function of quantum states that is zero for stabilizer states and non-increasing under Clifford unitaries. Measures of magic can also be used to quantify the non-Clifford resources required to prepare a state, and how useful it can be in synthesizing non-Clifford gates via magic state distillation and injection. We consider two measures of magic: the second stabilizer Rényi entropy [89] and the basis-minimized measurement entropy.

### 3.3.1 Second Stabilizer Renyi Entropy

The second stabilizer Rényi entropy (SSRE) measures how spread out the state's density matrix is when expanded in the basis of Pauli operators. A key property of stabilizer states is that they are the common eigenstate of a maximal set of mutually commuting Pauli operators [91]. As a result, the stabilizer state's density matrix is only supported on those operators, so it is maximally concentrated and the SSRE is zero. A Haar state on $N$ qubits, by contrast, has approximately equal weight on all Pauli operators, so it is nearly maximally spread out and the SSRE, defined as $M_2(\rho) = -\log \frac{1}{2^N} \sum_{P \in \mathcal{P}} \mathrm{Tr}(\rho P)^4$ for $N$ qubits, is proportional to $N$. The histograms in Fig. 3.1B illustrate the distribution of Pauli expectations for these two cases.

### 3.3.2 Basis-Minimized Measurement Entropy

We also consider a second measure of magic, which we call *basis-minimized measurement entropy*, defined as the entropy of the Born probability distribution of measurement outcomes, minimized over the finite set of possible stabilizer measurement bases. For instance, consider a

two-qubit stabilizer state $|00\rangle$ which we can measure in arbitrary length-two Pauli bases, including $X_1X_2$ and $Z_1Z_2$. Measuring $X_1X_2$ will result in a Born probability distribution of four equally possible measurement outcomes $|\pm\pm\rangle$, giving an entropy of 2. On the other hand, measuring in $Z_1Z_2$ results in only one outcome $|00\rangle$, giving an entropy of 0. Minimizing the entropy over all possible measured bases, the resulting basis-minimized measurement entropy is 0 in this case. We wish to compute this basis-minimized measurement entropy for the resulting logical state in our model—that is, the state on the logical qubits after encoding, noise, application of the inverse of the encoding circuit, and syndrome measurement. In Appendix C.1, we show that the basis-minimized entropy is a good measure of non-stabilizerness for pure states. It is zero for a stabilizer state, is non-increasing under Clifford unitaries, and is subadditive for product states, i.e. $f(\sigma \otimes \rho) \leq f(\sigma) + f(\rho)$.

The basis-minimized measurement entropy of the logical state depends on the syndrome outcome. Averaging the entropy of the logical state over all syndromes $\boldsymbol{s}$ gives us the basis-minimized classical conditional entropy $\min_B S_{\boldsymbol{l}_B|\boldsymbol{s}} = \min_B (S_{\boldsymbol{l}_B,\boldsymbol{s}} - S_{\boldsymbol{s}})$, where $S_{\boldsymbol{s}}$ is the entropy of the distribution of syndromes, $B$ is a stabilizer basis for the logical Hilbert space, and $l_B$ is the outcome of measurement in stabilizer basis $B$. Furthermore, the conditional entropy without any basis minimization serves as a good upper-bound in the non-magical phase. Below the code's error correction threshold, the logical state is close to the initial computational basis state, so we expect the optimal basis to be the computational basis. So, for small $\alpha$ in our model, we expect the optimal basis to be the computational basis, and the conditional entropy is close to its optimal value (after basis minimization). Furthermore, the Rényi analogue of the conditional entropy, $S^{(2)}_{\boldsymbol{l}_B,\boldsymbol{s}} - S^{(2)}_{\boldsymbol{s}}$ where $S^{(2)}_X = -\log \sum_{x\in X} p_x^2$ is the Rényi entropy of distribution $X$, is analytically approachable. We compute the conditional entropy in classical simulation and experiment, and

the Rényi analogue in experiment and analytical calculations.

The conditional entropy of the logical state quantifies the uncertainty in the logical space given a syndrome measurement, and it directly bounds the ability of a decoder to recover encoded classical information from measurements of the logical qubits (see Appendix C.7). A decoder is a syndrome-dependent operation that corrects logical errors corresponding to the syndrome measured. While the basis-minimized conditional entropy measures the minimal uncertainty over all possible Clifford decoding operations, the conditional entropy without basis-minimization limits the decoder to measurements in the computational basis.

In our experiment, we measure these measures of magic as a function of the error rate $\alpha$, tuning it from $0$ to $\pi/2$. At zero error ($\alpha = 0$) and maximal error ($\alpha = \pi/2$), both measures are identically zero, because in each case the state is a stabilizer state. When $\alpha = 0$, the noise layer acts as the identity operator, the encoding circuit $C$ is cancelled by the following $C^\dagger$, and the final state is the same as the input stabilizer state. When $\alpha = \pi/2$, the error operator $e^{-i\sigma_z \alpha/2}$ is itself a Clifford gate, so the magic is likewise zero.

### 3.3.3 Circuits Generation

The quantum circuits in the model were produced by randomly sampling Clifford encoders. Each encoder has depth $d$, where a unit of depth consists of a layer of $N$ single-qubit gates and a layer of $N/2$ disjoint pairs of entangling gates. The single qubit gates are sampled from the set of 24 single-qubit Clifford gates. The entangling gate is chosen to be the fixed-angle Mølmer-Sørensen gate, $MS(\pi/2)$. After selecting the gate sequence for each circuit, the encoder and decoder are optimized separately. After optimization, the circuits are compiled natively to a

gateset comprising GPi, GPi2 and MS gates, as described in IonQ Documentation [92]. As a part of execution, the circuits were further augmented with single-qubit gates to minimize noise, using a firmware-level protocol described in [93].

## 3.4 Vanishing Rate Code

First, we discuss the vanishing rate case with a single logical qubit. Between the two special Clifford points $\alpha = 0, \pi/2$ the logical qubit has finite magic according to SSRE, with a peak at a distance $\propto 1/\sqrt{N}$ away from the Clifford point $\alpha = \pi/2$ point (see Fig. 3.2B). At large $N$ the Clifford point, therefore, becomes a singularity. We can understand the square root scaling by perturbing around the Clifford point $\alpha = \pi/2$. At the Clifford point, the logical state is not magical because it is an equal superposition over states corresponding to that syndrome. Away from the Clifford point, the logical state becomes magical to the extent the amplitudes in the superposition are no longer equal. If exactly two errors give rise to each syndrome and the two errors corresponding to the measured syndrome have weights $n_a, n_b$, then the ratio of amplitudes is $[\tan(\pi/2-\alpha)]^{(n_a-n_b)} \approx (\pi/2-\alpha)(n_a-n_b)$, and the SSRE is $\mathcal{M}_2 \approx (\pi/2-\alpha)^2(n_a-n_b)^2$ (see Appendix C.3). Fig. 3.2A shows the SSRE, for classical simulations of circuits; the distribution is sharply peaked near this prediction. Since the error weights $n_a, n_b$ controlling the SSRE, are drawn from a binomial distribution, averaging over syndromes gives $\mathcal{M}_2 \propto N(\pi/2-\alpha)^2 = f((\pi/2-\alpha)\sqrt{N})$. (See Appendix C.3 details.) Fig. 3.2B shows the syndrome- and circuit-averaged SSRE, as a function of error angle $\alpha$; Fig. 3.2C shows the same quantity for experiments (see below). Both show the predicted square-root scaling $\langle \mathcal{M}_2 \rangle = f((\pi/2-\alpha)\sqrt{N})$.

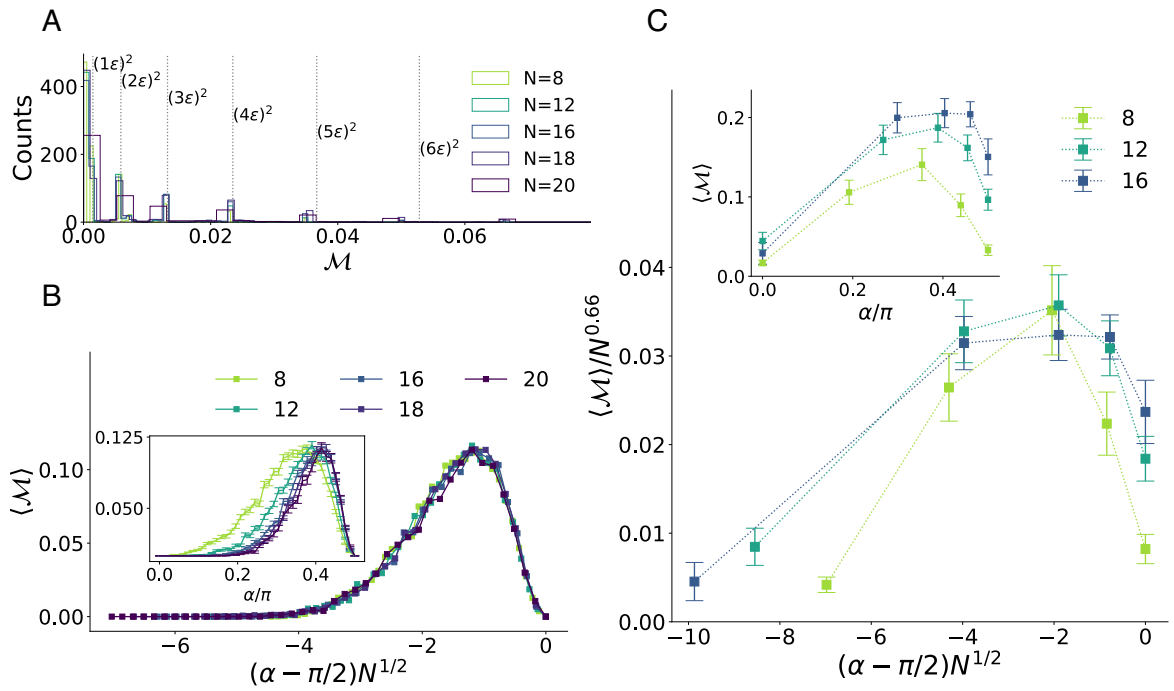


Figure 3.2: **A**: Distribution of second stabilizer Rényi entropy (SSRE) across codes and syndromes in classical simulation. The distribution is tightly peaked around square-integer multiples of the distance $\epsilon = \pi/2 - \alpha$ from the Clifford point, because it is controlled by the weights of the errors. **B & C**: Syndrome- and circuit-averaged SSRE, in classical numerics (B) and experiment on IonQ Aria trapped-ion quantum computer (C). Both display the predicted square-root scaling. The error estimates are derived using bootstrapping (details in the Appendix C.6). The scaling with respect to system size of the vertical axis of C (main) is chosen to match the scaling of the peak in unscaled experimental data (inset). For B, the errorbars are omitted in the collapse (main plot).

### 3.4.1 Experiment

We perform our experiments on IonQ's Aria quantum processor, made available through the QLab facility at the University of Maryland. We use 16 out of 32 qubits for our experiments to limit the circuit depth and effects of noise. All quantum circuits, compiled into a native gateset, were executed using API access. We provide further details on circuit execution in Appendix C.2. For the vanishing rate case, we run the encoding, error, and decoding circuit over $N$ physical qubits many times. Since we need to perform tomography on the single logical qubit, we append

an appropriate basis change Clifford gate for each instance of random encoding circuit. Finally, we measure the entire register. Postselecting on syndrome outcomes is prohibitively expensive, so we use the fact that the number of effective actions on the logical qubit (up to a global phase) is much smaller than the number of possible syndromes. This allows us to group the syndrome into equivalence classes, where elements in a class have the same effective action on the logical qubits. These classes are identified by grouping the rotations using classical simulations. To mitigate incoherent errors, we project the density matrix of the logical qubit, obtained using tomography of a syndrome-class, to its maximum-eigenvalue eigenstate in post-processing. We then calculate the circuit- and syndrome-averaged magic $\mathcal{M}(\alpha) = \langle |\overline{s}| \times \langle M_{C,\overline{s}} \rangle_{\overline{s}\in\mathcal{S}} \rangle_C$, where $\mathcal{S}$ denotes syndrome classes and $|\overline{s}|$ denotes the size of a syndrome class $\overline{s}$.

We present our experimental measurements in Fig. 3.2E for $N = 8, 12,$ and $16$, using $50$, $50$ and $30$ instances, respectively, of random circuits. The error-bars are obtained via bootstrap resampling (details in Appendix C.6). We observe that, following the mitigation techniques discussed above, we can achieve a measurement of magic that qualitatively resembles the theoretical expectations.

## 3.5 Constant Rate Code

At finite rate—that is, when the number of logical qubits $K$ scales as $K = rN$ with the number of physical qubits $N$—the finite-magic critical region displayed by the vanishing-rate code becomes an extended magical phase. This magical phase is visible in Fig. 3.1C, which shows the phase diagram of SSRE as a function of the code and error rate in classical simulations for systems of $N \leq 14$ physical qubits. Fig. 3.3A shows the density of SSRE at fixed rate $r = 1/2$

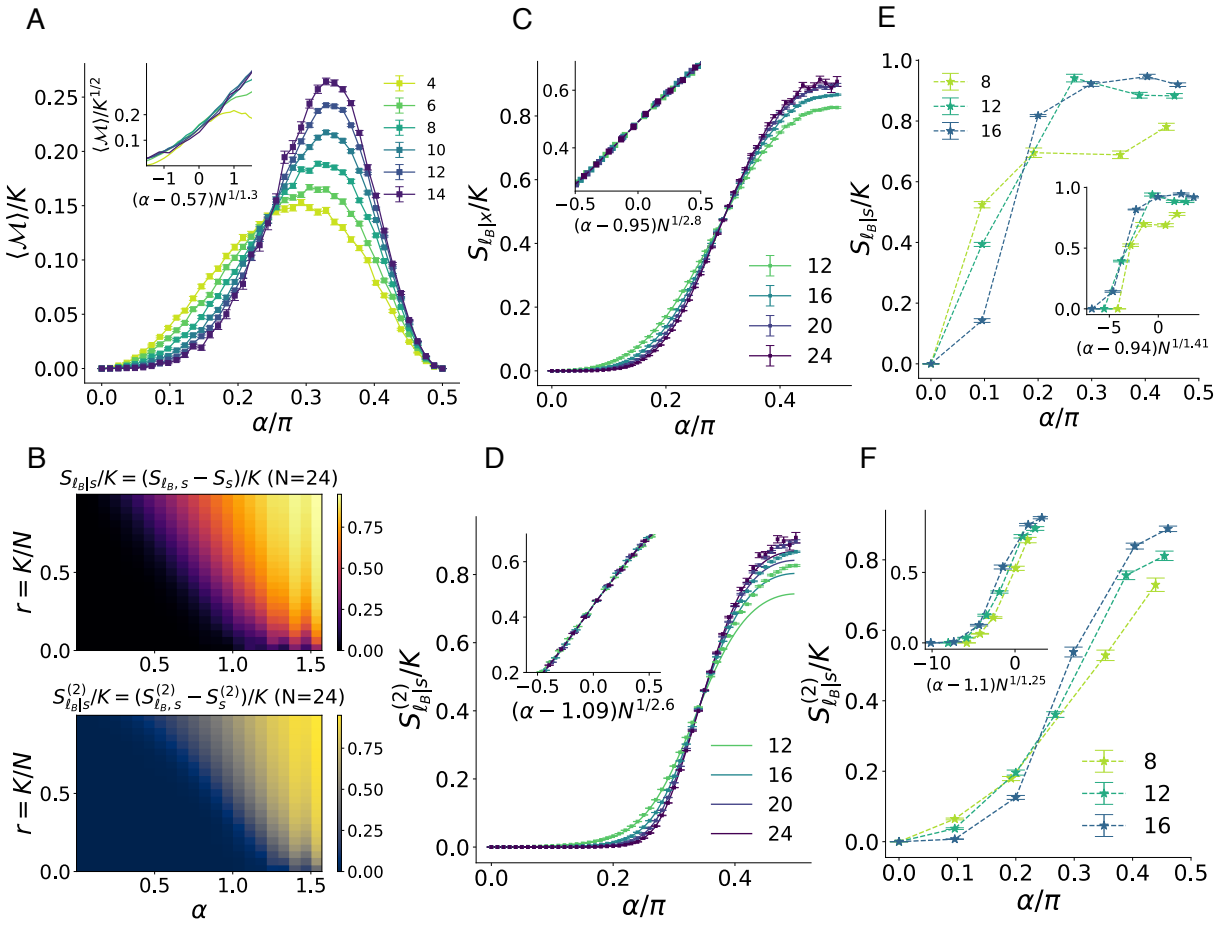


Figure 3.3: **Results for constant rate codes.** **A**: Density of magic (SSRE) of the logical space and its scaling collapse (inset) plotted against the error rate $\alpha$, for code rate $r = K/N = 1/2$. The error bars are derived using standard error and are omitted in the scaling collapse (inset), where the x-axis is scaled as $(\alpha - \alpha_c)N^{1/\nu}$ with critical parameters $\alpha_c = 0.573(8)$ and $\nu = 1.3(1)$. **B**: Phase diagrams of conditional entropy (upper) and its Rényi approximation (lower), without any basis minimization. **C**: Finite size scaling of the conditional entropy and its collapse (inset) computed numerically using simulations at $r = 1/2$. The scaling collapse (inset) has critical parameters $\alpha_c = 0.95(5)$ and $\nu = 2.8(6)$. **D**: Finite size scaling of the Rényi approximation of the conditional entropy and its collapse (inset) computed numerically using simulations (displayed points) and analytics (solid line) at $r = 1/2$.. The scaling collapse, computed with data from simulations, has critical parameters $\alpha_c = 1.090(3)$ and $\nu = 2.6(3)$. **E**: Finite size scaling of the conditional entropy using data from experiments in IonQ Aria at $r = 1/2$. The error bars are obtained using boostrap resampling. The scaling collapse (inset) uses critical exponents derived from numerical simulations of circuits with $d = N/2$, as shown in Fig. C.2. **F**: Finite size scaling of the Rényi-approximation of the conditional entropy and its collapse (inset) computed using experiments at $r = 1/2$.

as a function of error rate $\alpha$, again in classical simulations. The scaling collapse indicates that the transition from non-magical to magical is indeed a phase transition, not a crossover.

Since the SSRE is an expensive quantity to measure for finite-rate codes, we use the conditional entropy of the logical state as a diagnostic for the phases. In Fig. 3.3B (upper), we show the phase diagram for conditional entropy density as a function of code rate and error-rate. The conditional entropy, without any minimization over basis, serves as an upper-bound to the basis-minimized conditional entropy, which is a genuine measure of magic. Therefore, the conditional entropy is a good diagnostic for the non-magical phase. In Fig. 3.3C, we present finite rate scaling, obtained through simulations, of the conditional entropy at code rate $r = 1/2$. This critical error rate $\alpha_c$ and critical exponent $\nu$ both differ from the SSRE. Such a difference in critical point and scaling exponent is a common feature of phase transitions in monitored quantum circuits; it comes about because different quantities correspond to different statistical mechanical models [30,32] and because different measures quantify resources differently. For each datapoint in numeric simulations of sizes $N = 12, 16, 20$ and $24$, we simulate $5000, 5000, 500$ and $50$ circuits, respectively. The procedure used to extract the critical parameters and their errors is described in Appendix C.5.

### 3.5.1 Analytical Approximations

We also observe that the Rényi conditional measurement entropy, the Rényi analogue of the Shannon conditional measurement entropy, exhibits similar phases, as shown in Fig. 3.3B

(lower). The circuit-averaged conditional Rényi entropy is defined as

$$\mathbb{E}_C \left[ -\log \sum_{x\in\{0,1\}^N} \left(p^{\alpha,C}_{(\ell,s)}(x)\right)^2 + \log \sum_{s\in\{0,1\}^{N-K}} \left(p^{\alpha,C}_{s}(x)\right)^2 \right], \tag{3.1}$$

where $p^{\alpha,C}_s(x)$ denotes the probability of measuring $x$ in the syndrome register $s$, for a state produced with a Clifford encoder $C$ and coherent rotations of strength $\alpha$. Similarly the $(\ell, s)$ subscript denotes measurement in the joint syndrome and logical register. For large systems, we can use a typicality argument to assume that the circuit-to-circuit variation in distribution of measurement outcomes is negligible; this allows us to interchange logarithm with expectation over $C$ in the equation above. Finally, we can calculate $\mathbb{E}_C \sum_x (p^{\alpha,C}(x))^2$ using Clifford averaging via Schur-Weyl duality (see Appendix C.8 for details).

Fig. 3.3D shows the finite-size scaling for Rényi conditional measurement entropy, for system sizes $N \leq 24$ comparable to those used in classical simulation and experiment, at code rate $r = 1/2$. The analytical result is plotted as solid lines. The datapoints represent circuit averages computed via numerical simulations. For each datapoint in numeric simulations of sizes $N = 12, 16, 20$ and $24$, we simulate $5000, 5000, 500$ and $50$ circuits, respectively. Indeed, the analytical computation matches the exact numerics for large systems for which the typicality assumption is true. While our analytics lets us access arbitrarily large sizes for this observable, we perform the scaling collapse over sizes that are experimentally accessible. The procedure used to perform the scaling collapse and extract related errors is described in Appendix C.5.

### 3.5.2 Experiment

The random Clifford code was implemented on up to 16 qubits of IonQ's 32-qubit Aria device. (The implementation was limited not by the number of qubits available but by circuit depth, which in turn was limited by gate noise.) The second stabilizer Rényi entropy is not accessible in experiments on finite-rate codes, because it requires full state tomography. The conditional measurement entropy, by contrast, requires only computational basis measurements. These computational basis measurements undergo postprocessing similar to linear cross-entropy benchmarking in random circuit sampling experiments [10], using information from classical simulation. The reported entropies are $S_X = -\sum_x p(x) \log \tilde{p}(x)$, where $\tilde{p}(x)$ is the probability anticipated from classical simulation, and $p(x)$ are experimentally obtained distributions projected onto the support of the ideal distribution $\tilde{p}(x)$.

Figures 3.3E and 3.3F show the resulting Shannon and Rényi entropies, respectively. As expected, the scaling of the entropies with respect to system size is inverted across the threshold. Recall that the experiments were performed using circuits of depth $d = N/2$. The scaling collapse (insets) in the experimental data use the critical parameters derived from numerical simulations for $d = N/2$ circuits, as shown in Fig. C.2B,C in Appendix C.4. For each experimental datapoint of sizes $N = 8, 12$ and 16, we execute $50, 50$ and 20 different circuit instances, respectively. The errorbars were estimated using boostrap resampling, discussed in Appendix C.6.

## 3.6 Outlook

We have observed that a random Clifford code subject to coherent errors displays a phase transition in magic. Concentrating magic of a large system to a smaller subsystem can be difficult,

as has also been shown in [35]. In our model, measuring the syndromes of a random Clifford code concentrates magic in the logical space if the error rate or the code rate is above a critical value, and suppresses magic below the threshold. This result establishes a connection between the resource theory of stabilizer computation, i.e., magic, and the study of decoder breakdown in quantum error correction codes via the basis-minimized measurement entropy.

In this work, we study phases of magic for small systems for which calculating measures of magic is tractable. In general, non-stabilizerness is difficult to measure. Measures of magic usually require exponentially many measurement samples and often need extensive classical processing, making them intractable for large systems. Our work, however, suggests the possibility of diagnostics, like the conditional entropy, that can be estimated efficiently using a small number of samples and classical post-processing. In the future, such measures can be used to study the phase transition in larger systems to better approximate the thermodynamic limit.

Phase transitions in magic—both ours and the theoretical predictions of [35]—indicate that existing measurement-induced phase transitions sit in a broader landscape of information theoretic phase transitions. In each case, the phase transition arises from the competition between three channels—a channel that generates the resource (whether entanglement or magic), a channel that generates correlations, and a channel that destroys the resource—that fail to commute. In the phase transition shown here, the correlation-generating channels are the encoding Clifford operations, the resource-generating channels are the rotations $R_z(\alpha)$ of the noise layer, and the resource-destroying maps are syndrome measurements. In the phase transition of [35] the correlation-generating channels are layers of random Clifford gates, the resource-generating channels are interspersed T gates, and the resource destroying maps are partial traces. In the measurement-only entanglement phase transition of [94], all channels are projective measurements: nonlocal

projective measurements generate entanglement as well as correlation, while onsite measurements destroy the resource. We conjecture that any information-theoretic setting with this structure of three competing channels can be made to show a phase transition.

Our result also suggests that error correction together with sufficiently well-characterized coherent noise can create useful magic states. In the magical phase the syndrome measurements move magic from the physical qubits, where non-Clifford gates like single-qubit rotations are easy, to the logical qubits, where non-Clifford gates are typically hard. Syndrome-dependent Clifford unitaries may then transform these states into states suitable as inputs to existing magic state distillation protocols. In this case, an outstanding challenge is the decoding problem of identifying the right Clifford unitary given a code and a syndrome. Notably, such unitaries are efficiently computable under a wide-range of circumstances for zero-rate topological surface codes [95]. If this can be done more generally, the magical phase may improve the efficiency of magic state distillation, thereby reducing overhead in quantum computation algorithms where magic state distillation is the bottleneck.

# Chapter 4: Error Mitigation Threshold

Extracting useful information from noisy near-term quantum simulations requires error mitigation strategies. A broad class of these strategies rely on precise characterization of the noise source. We study the performance of such strategies when the noise is imperfectly characterized. We adapt an Imry-Ma argument to predict the existence of an *error mitigation threshold* for random spatially local circuits in spatial dimensions $D \geq 2$: characterization disorder below the threshold rate allows for error mitigation up to times that scale with the number of qubits. For one-dimensional circuits, by contrast, mitigation fails at an $\mathcal{O}(1)$ time for any imperfection in the characterization of disorder. We discuss implications for tests of quantum computational advantage, fault-tolerant probes of measurement-induced phase transitions, and quantum algorithms in near-term devices.

Noise presents a fundamental barrier to realizing scalable quantum information processing [4]. The theory of fault-tolerant quantum error correction shows how this barrier can be overcome in principle [53, 96, 97]. However, despite remarkable experimental progress establishing the basic validity of the theory of fault-tolerance [63,98–100], achieving large-scale quantum computing with error corrected qubits remains a formidable challenge. In recent years, quantum error mitigation has emerged as a complementary paradigm for addressing the effects of noise in large-scale quantum devices [42, 101–112]. At its core, error mitigation relies on the ability

to accurately characterize the interaction of the system with its environment. Armed with this knowledge, one can design classical post-processing techniques to construct more accurate estimators of the noiseless signal using data obtained from a noisy device. Similar methods have been ubiquitously employed in quantum process tomography to reliably extract error models in the presence of noisy operations [113–115]; using these methods to improve the accuracy of noisy quantum circuits is a more recent development.

A key aspect of the threshold theorem for fault-tolerant quantum computing is that it applies even in the case where the individual components used to implement the error correction are noisy. An analogous question for error mitigation strategies is whether they work when the noise is imperfectly characterized. As noted above, related questions have been addressed for quantum process tomography in the presence of faulty operations [113–115]; however, these models are often considered only at the level of a few qubits, generally precluding the existence of a sharply defined phase transition. In the case of many-body tomographic problems (e.g., Pauli noise estimation [116, 117] or Hamiltonian learning [118, 119]), thresholds in learnability are possible and likely arise under some circumstances. However, to our knowledge, threshold results have not been considered for quantum error mitigation.

In this paper, we demonstrate the possibility of thresholds for quantum error mitigation. We focus on one of the conceptually simplest quantum error mitigation techniques, which goes under the moniker "probabilistic error cancellation" (PEC) [102, 120]. PEC relies on the fact that many of the most common noise channels used to model quantum devices are actually trivially invertible at the mathematical level. Unfortunately, the inverse operation is not generally a physical evolution. For example, the inverse of the depolarizing channel violates the complete-positivity condition for quantum channels. As a result, the only known way to implement the

inverse is through classical post-processing. In the case of PEC, this classical post-processing step is implemented via Monte Carlo sampling methods but, for constant noise rates, incurs exponential sampling overheads in the worst case [102, 120]. Nevertheless, PEC can be used to significantly extend the accessible circuit depths of a given noisy quantum device, as demonstrated in recent experiments [120]. Some other examples of quantum error mitigation include zero-noise extrapolation [102–104], symmetry-based error detection [106, 107], cooling/purification [108–110], and learning based methods [111, 112]. In the remainder of the paper we will focus on the PEC technique, primarily because of its conceptual simplicity.

Our central prediction is that PEC has an error mitigation threshold for random, spatially local circuits in spatial dimensions $D \geq 2$ when the noise is imperfectly characterized. Building on the extensive work characterizing quantum phases and phase transitions in hybrid random circuits [121, 122], we consider a model of random unitary circuits subject to depolarizing noise with binary disorder in the depolarization rate [see Fig. 4.1(a)]. To mitigate the effects of the noise we apply a uniform "antinoise" channel that inverts the depolarizing noise on average. We show that a replica statistical mechanics description of the problem has close parallels to the classical random field Ising model (RFIM) in $D + 1$ dimensions. At the zero-mean field condition in the RFIM, Imry-Ma arguments [123] show that the ordered phase survives random symmetry-breaking terms in sufficiently high dimensions. In the random circuit problem, this analysis indicates the possibility for error mitigation thresholds for $D \geq 2$, while $D = 1$ is the marginal dimension. We also analyze the performance of error mitigation as a function of circuit depth. For depths larger than the linear size of the system, the mitigation fails, resulting in a signal worse than that obtained by sampling from the uniform distribution. The corresponding phase diagram of the system is shown in Fig. 4.1(b) for $D \geq 2$. Analytic and numerical studies

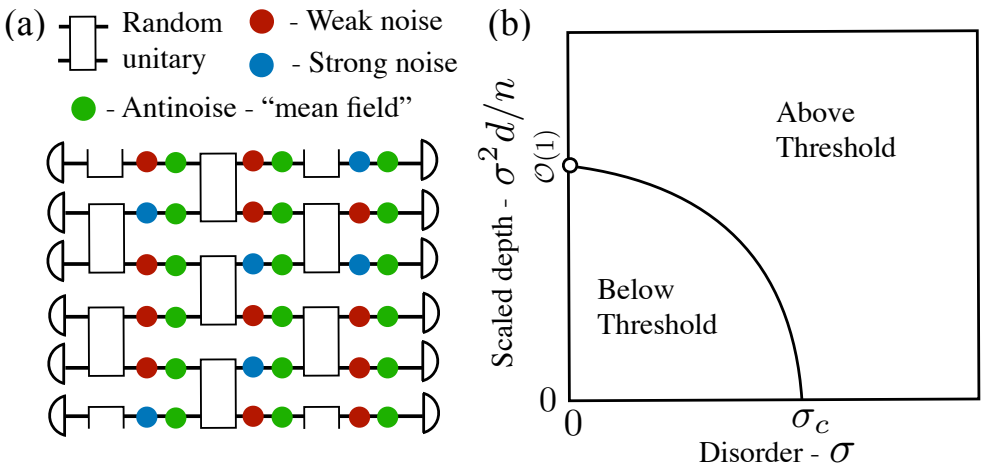


Figure 4.1: Model and phase diagram: (a) Noisy random circuit with spacetime disorder in the noise rate and error mitigation. (b) Phase diagram for the error mitigation threshold in this model for $D \geq 2$ spatial dimensions. At high disorder rates and linear depths, the system transitions from a "below-threshold" phase where mitigation succeeds on average to an "above-threshold" phase where mitigation fails.

of the two-copy replica theory and exact simulations of the mitigated circuit dynamics confirm our predictions.

## 4.1 Model and Simplified Limits

The basic model we consider in this work is illustrated in Fig. 4.1(a). Each two-site gate is chosen to be Haar random [124–126] and are interspersed with noise and antinoise channels. We focus on the case of depolarizing noise and its inverse channel as the antinoise

$$\mathcal{E}_{\boldsymbol{x},t}(\rho) = (1 - q_{\boldsymbol{x},t})\rho + q_{\boldsymbol{x},t}\,\mathrm{tr}_{\boldsymbol{x}}[\rho] \otimes I/2, \tag{4.1}$$

$$\mathcal{A}_{\boldsymbol{x}}(\rho) = \frac{\rho - q_a\,\mathrm{tr}_{\boldsymbol{x}}[\rho] \otimes I/2}{1 - q_a}, \tag{4.2}$$

where $\mathrm{tr}_{\boldsymbol{x}}[\rho]$ is a partial trace operation at site $\boldsymbol{x}$. Tuning $q_a = q_{\boldsymbol{x},t}$ inverts the noise at space-time site $(\boldsymbol{x}, t)$ such that $\mathcal{A}_{\boldsymbol{x}} \circ \mathcal{E}_{\boldsymbol{x},t}(\rho) = \rho$. To include the disorder, the noise rates are drawn randomly at each space-time location of the circuit from one of two values $q_{\boldsymbol{x},t} = q_{1/2}$ with probability $p/1-p$ and $q_1 < q_2$. The antinoise can be tuned to a zero mean-field condition by taking $(1-q_a) = (1-q_1)^p(1-q_2)^{1-p}$ equal to a geometric mean. This condition ensures that a Pauli operator $\sigma^\mu_{\boldsymbol{x}}$ ($\mu \in \{X, Y, Z\}$) evolved under multiple rounds of noise and antinoise up to depth $t = d$ will have expectation value

$$\mathrm{tr}\left[\sigma^\mu_{\boldsymbol{x}} \prod_{t=1}^{d} \mathcal{A}_{\boldsymbol{x}} \circ \mathcal{E}_{\boldsymbol{x},t}(\rho)\right] = \prod_t \frac{1-q_{\boldsymbol{x},t}}{1-q_a} \mathrm{tr}[\sigma^\mu_{\boldsymbol{x}}\rho], \tag{4.3}$$

where the prefactor tends to a log-normal distribution that concentrates around one. Any deviations of $q_a$ from this zero mean-field condition will result in an exponential growth rate that scales linearly in the depth $d$. At the zero-mean field condition, however, the noise is canceled on average and the prefactor deviates from one only due to random fluctuations as $e^{\pm\mathcal{O}(\sqrt{d})}$ (i.e., the exponential growth rate is suppressed by a factor $\sqrt{d}$).

To develop some basic intuition for how unitary dynamics can improve the robustness of error mitigation, it is helpful to consider a toy model consisting of two sites $L/R$ with $q_L < q_R$ fixed in time. Now, take $1-q_a = \sqrt{(1-q_R)(1-q_L)}$ to satisfy the zero mean-field condition. The $R$ site will be subject to excess noise and the $L$ site will experience excess antinoise. The case of weak unitary dynamics is analogous to the above threshold phase. In the limit where the unitary dynamics tends to trivial evolution, any state initialized with non-zero Pauli expectation value on site $L$ will experience exponential growth of the expectation values leading to an unphysical density matrix after an $\mathcal{O}(1)$ time. We discuss below how this type of rapid

instability to unphysical states is characteristic of the above threshold phase.

To build in the effects of unitary dynamics, consider the base circuit to consist of repeated applications of SWAP gates. In this case, it is readily verified that the effects of the noise on Pauli expectation values will be completely canceled for arbitrarily deep circuits except for the most recent layer of gates. In this two-qubit example, Haar random gates behaves similarly to SWAP gates in that the noise is cancelled on average. However, the temporal randomness will lead to exponential fluctuations of Pauli expectation values of size $e^{\mathcal{O}(\sqrt{d})}$, where the term in the exponent will follow the statistics of a random walk. This tendency of the random unitary dynamics to suppress effects of the noise/antinoise from linear in $d$ to $\sqrt{d}$ scaling for certain initial conditions is characteristic of the behavior we find for the below-threshold phase. To more quantitatively capture the trends found in this simple two-site model, we now develop a mean-field theory for the threshold.

## 4.2 Mean-field Theory

In deriving a mean-field theory, it is convenient to turn to a more analytically tractable model formulated in continuous time rather than as a discrete circuit. The noise and antinoise are now captured through a Lindblad master equation [127]

$$\dot{\rho} = -i[H(t), \rho] - \sum_j (\gamma_j - \gamma_a)\big(\rho - \mathrm{tr}_j[\rho] \otimes I/2\big), \tag{4.4}$$

$$H(t) = \sum_{i<j,\mu,\nu} J_{ij\mu\nu}(t)\sigma_i^\mu \sigma_j^\nu, \tag{4.5}$$

where $H(t)$ is a time-dependent Hamiltonian that sets the unitary evolution, $\gamma_i$ is the random noise rate on site $i$, and $\gamma_a$ is the antinoise rate. The noise rate $\gamma_i = \gamma_{1/2}$ is drawn randomly with probability $p/1-p$. The zero mean-field condition becomes $\gamma_a = \bar{\gamma} \equiv p\,\gamma_1 + (1-p)\,\gamma_2$. We take the random unitary dynamics to be given by an all-to-all coupled Brownian circuit model in which the $J_{ij\mu\nu}(t)$ are drawn from a white-noise Gaussian random process with variance parameters [128, 129]

$$\langle J_{ij\mu\nu}(t) J_{k\ell\gamma\delta}(t')\rangle = \frac{J}{2N}\delta_{ik}\delta_{j\ell}\delta_{\mu\gamma}\delta_{\nu\delta}\delta(t-t'). \tag{4.6}$$

To treat this model analytically, we average the dynamics over the random coupling constants for multiple identical copies of the density matrix $\rho(t)^{\otimes k}$ ($k$ is a replica index). In the equations of motion for the averaged moments $\rho_k(t) \equiv \mathbb{E}_H[\rho^{\otimes k}]$, the unitary drive-term averages to zero, leading to a purely dissipative master equation for $\rho_k(t)$ (see Appendix D.1). Focusing on second moments ($k = 2$) gives rise to a particularly simple model with two global product steady states given by $I^{\otimes N}$ and $S^{\otimes N}$ [129], where $S$ is the SWAP operator acting on the two copies. The all SWAP steady-state captures non-trivial corrections to second moment observables like the purity of sub-systems. In the mean-field approximation, we enforce the density matrix to take a product state form $\rho_2 = \bigotimes_{i=1}^{N} \sigma_i$. Due to the lack of symmetries or conservation laws in the problem, $\sigma_i$ can be parameterized as

$$\sigma_i = (1/4 + \delta_i)|s\rangle\langle s| + (1/4 - \delta_i/3)P_T, \tag{4.7}$$

where $\delta_i$ is the deviation from an infinite temperature state, $|s\rangle$ is a two-qubit singlet state across the two copies, and $P_T$ is the projector onto the two-qubit triplet subspace of the two copies.

The mean-field equations for $\delta_i$ take the form

$$\dot{\delta}_i = -4\Big[\Delta_i + \frac{J}{N}\sum_{j\neq i}(3+4\delta_j)\Big]\delta_i, \tag{4.8}$$

where $\Delta_i = \gamma_i - \gamma_a$. This simple equation captures much of the basic physics we described in the two-site model, while also exhibiting the phase transition. Notably, we can see that at weak values of the disorder, the interaction term acts as a restoring force towards the fixed point $\delta_i = 0$. The other fixed point $\delta_i = -3/4$ corresponds to an unphysical density matrix, which is unstable at weak disorder. At a critical disorder strength of $|\Delta_1| = 3J$ (see App. D.1), however, the $\delta_i = 0$ fixed point becomes unstable. The dynamics flows to a new stable fixed point which is an unphysical density matrix. Thus, we see that the above threshold phase in the mean-field theory is characterized by an instabilty of the density matrix to unphysical states.

To rigorously characterize the threshold behavior, particularly in finite-dimensional systems, we need a more systematic treatment of the correlations in the state beyond the mean-field approximation. To develop this approach, it is convenient to return to the circuit models. In these discrete models, the connections to the physics of the RFIM become more explicit.

## 4.3 Statistical Mechanics Mapping

Our rigorous analysis of the problem relies on well-established mappings from random quantum circuit dynamics in $D$ spatial dimensions to statistical mechanics models in $D+1$ dimensions [51, 125, 126, 130–134]. We outline the details of the mapping in Appendix D.2. The approach we take is to expand $\rho_k \equiv \mathbb{U}[\rho^{\otimes k}]$ into a basis of operators based on representations of the permutation group $S_k$ [131]. One can then derive update rules for the averaged state following

each layer of gates, noise, and antinoise. In this paper, we focus on the two-replica case where the two operators are $I$ and $S$ (the SWAP gate). We expect this model to be sufficient to capture many of the properties of the transition, as has been argued in the unitary case [125]. Numerical evidence based on exact simulations is presented below that support this claim.

Without noise/antinoise, $\rho_2$ has two fixed points $I^{\otimes N}$ and $S^{\otimes N}$ just as in the Brownian circuit model. Configurations with persistent "domain walls" (i.e., mixtures of $I$ and $S$) are exponentially damped with depth in the model. As a result, the two fixed points can be interpreted as ferromagnetic ground states of an Ising-type spin model. In this interpretation, noise acts as a symmetry breaking field because it favors the identity configuration and damps out configurations with $S$ operators [51]. Antinoise acts as a field in the opposite direction, but it also adds additional sign-structure to the problem from the second term in Eq. (4.2). We account for this sign by labeling spacetime configurations of $I$ and $S$ operators by the sign of their contribution, then we can write $\rho_2 = \rho_2^+ - \rho_2^-$, where $\rho_2^\pm$ sum over spacetime configurations with a positive/negative sign.

## 4.4 Imry-Ma arguments

To make precise connections to Imry-Ma arguments [123], we rigorously analyze finite-dimensional versions of the statistical mechanics models. First, we define a *simple initial condition* as a state $\rho_2$ that is identity everywhere except in a contiguous region $A$ where it is given by $\mathrm{tr}_{A^c}[\rho_2] \propto I^{\otimes|A|} + S^{\otimes|A|}$. Such an initial condition can be prepared physically by taking a Haar random state (or a state drawn from a two-design such as the Clifford group [135]) on $A$ and the infinite temperature state on the complement of $A$. The first model we consider is a *quenched*

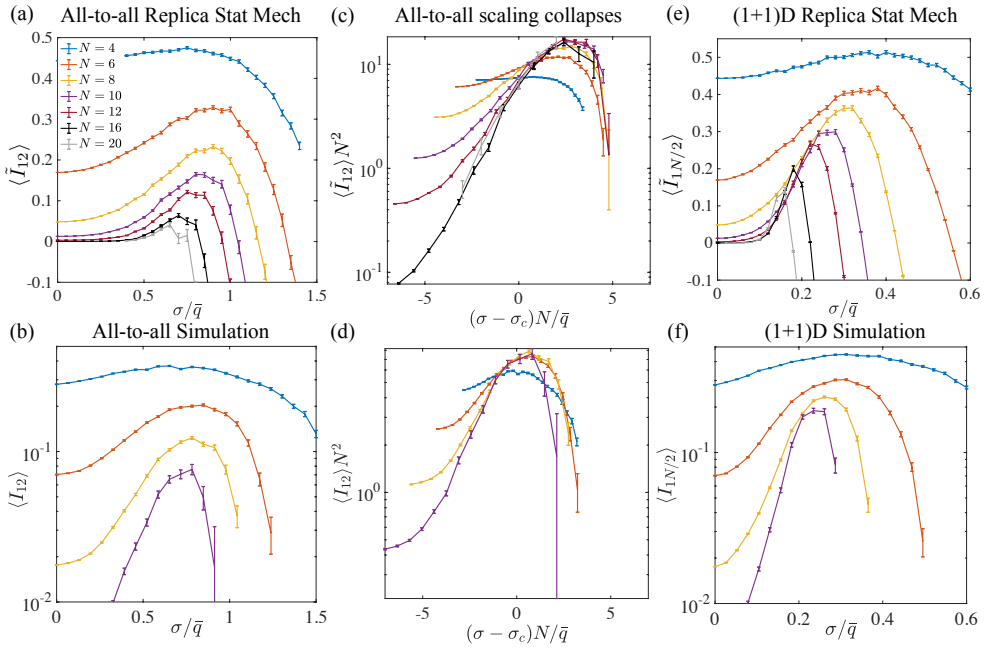


Figure 4.2: Numerical tests of the threshold behavior: (a) Numerical simulations of circuit and noise-disorder averaged the correlation metric $\tilde{I}_{12}$ obtained from purity of subregions for two random sites in the system. (b) Mutual information $I_{12}$ for exact simulations of the mitigated noisy random circuit. (c-b) Scaling collapse of data from (a-b) using $\sigma_c/\bar{q} = 0.65(5)/0.55(5)$ and critical exponent on $x$-axis obtained from local probe (see Appendix D.3). The critical scaling on the $y$-axis is an ansatz. (e-f) Similar quantities as (a-b) for antipodal sites of a 1D chain. The strong drift in the peak with increasing system size is consistent with the lack of a below-threshold phase in this model. In all the plots, we took a Haar random initial pure state with noise parameters $\bar{q} = 0.1$ and $p = 0.9$ and ran to depth $d = 4N$.

*1D* model described by a one-dimensional brickwork circuit of the type shown in Fig. 4.1(a) with Haar random two-qubit gates and spatially random noise rates that are constant in time. We define $\sigma = \sqrt{p(1-p)(q_2 - q_1)}$ as the standard deviation of the noise rates. We prove that the quenched 1D model always exhibits an instability for one of the simple initial conditions.

**Theorem 1** (Instability in quenched 1D)**.** *For the quenched 1D model with any $\sigma > 0$, there is a simple initial condition for subregion $A$ of size $\mathcal{O}(\log N)$ such that as $N \to \infty$ and $d \to \infty$ with high probability $||\rho_2^{\pm}|| \geq e^{\mathcal{O}(d \log N)}/2^{2N-|A|}3^{|A|}$.*

*Proof.* The proof of the theorem essentially follows a standard Imry-Ma argument. For any finite

$\sigma$ as $N \to \infty$ with high probability (whp) there will be a contiguous region of sites $A$ with noise rate $q_1$ of size $|A| = \mathcal{O}(\log N)$. For sufficiently large $N$ there will be a region satisfying $(1-q_1)^{|A|}/(1-q_a)^{|A|} > (5/2)^2$ whp, which implies that the $\mathcal{O}(1)$ boundary cost of the two domain walls at the edge of $A$ can be overcome by the amplification of the $S$ configurations in the bulk. Taking a configuration of all $S$ on $A$ with identities elsewhere that moves by order 1 site at the boundary at each time-step according to the rules for the replica model provides a contribution to $\rho_2^{\pm}$ that diverges as $e^{\mathcal{O}(d \log N)}/2^{2N-|A|}3^{|A|}$. The denominator is the normalization constant for the initial state. □

As a corollary to this result, an initial pure product state evolved with this model will also have this instability. The converse of this type of Imry-Ma argument is that we expect the instability of these initial conditions to be suppressed for weak enough disorder for high enough dimensions. In this case, for large regions $A$ the boundary cost of the domain wall scales as $|A|^{(D-1)/D}$, whereas the amplification from the antinoise scales as $|A|^{1/2}$. As a result, with quenched disorder in time, we expect the instability to vanish for $D \geq 3$ at sufficiently small values of $\sigma$, while $D = 2$ is the marginal dimension. For space-time random disorder, the marginal dimension is $D = 1$ and an ordered phase persists for $D \geq 2$. Note, that at large values of $\sigma$, the domain wall cost can be overcome even by a single site with strong antinoise, leading to an instability. As a result, there will be a disorder driven phase transition at finite $\sigma$ in sufficiently high-dimensions associated with the onset of this instability.

## 4.5 Numerical Tests

Figure 4.2 summarizes our numerical results. We run numerical simulations of random circuits, together with noise and antinoise, to characterize this phase transition in two settings. In the first case [see Fig. 4.2(a-d)], we simulate an infinite-dimensional circuit where entangling gates can exist between any pair of qubits and noise is random in both space and time. In the second case [see Fig. 4.2(e-f)], we simulate $(1+1)D$ circuit dynamics assuming quenched noise, where the randomness is only spatial. The first model is a test of the high-dimensional limit of the model, while the second model is the same one considered in Theorem 1.

In both cases, we initialize a state of a $N$-qubit register in a global Haar-random state, which corresponds to the string $\propto I^{\otimes N} + S^{\otimes N}$ in the statistical-mechanical mapping. For the infinite-dimension model, we apply random Haar gates on a set of $N/2$ disjoint pairs, randomly drawn from all $N(N-1)/2$ possible pairs of qubits. For the $(1+1)D$ model, each time-step corresponds to a layer in the brickwork circuit in Fig. 4.1 with periodic boundary conditions. Each layer of unitary gates is followed by the noise-antinoise channel on all qubits.

After evolving the circuit to depth $d$, we take the partial trace of two qubits and calculate correlation metrics between the two qubits [136,137]. These low-order correlations are exponentially suppressed in $N$ for $\sigma = 0$, but they develop a peak at the critical point where long-range correlations develop. For $D = 1$, the pair consists a randomly chosen qubit and its corresponding anti-pode at a distance of $N/2$; for the all-to-all model, both qubits are randomly chosen.

We study the two systems using the replica statistical-mechanical mapping introduced above, with background details in Appendix D.2. The mapping lets us probe the phase transition for system sizes as large as $N = 20$. For sizes up to $N = 10$, we complement the numerics on

statistical-mechanical mapping with direct circuit simulations. In the replica stat-mech model, we study a measure of correlations $\tilde{I}_{ab} = -\log_2 \mathbb{E}_U[\mathrm{Tr}[\rho_a^2]] - \log_2 \mathbb{E}_U[\mathrm{Tr}[\rho_b^2]] + \log_2 \mathbb{E}_U[\mathrm{Tr}[\rho_{ab}^2]]$ averaged over noise-disorder (denoted by $\langle\cdot\rangle$ brackets), while in the exact simulations we study the standard mutual information $I_{ab} = S_a + S_b - S_{ab}$ for the von Neumann entropy $S_a = -\mathrm{tr}[\rho_a \log_2 \rho_a]$ [4].

The numerical results provide strong supporting evidence for the theoretical scenario outlined above. We see evidence for a stable ordered phase in the high-dimensional limit of the all-to-all model, whereas the 1D model with quenched randomness in the noise is consistent with the lack of an ordered phase. In addition, we estimate critical exponents for the transition in Fig. 4.2(b-c) that are consistent with simple rational values characteristic of mean-field behavior.

## 4.6 Outlook

An important application of our results is to improved benchmarking and verification of random circuit sampling in noisy devices [12, 138–142]. In Appendix D.4, we demonstrate an exponential improvement in a mitigated version of the so-called "linear cross-entropy" fidelity below the error mitigation threshold. Notably, this mitigated benchmark can be computed using existing experimental data. The below threshold behavior may have important consequences for proofs of quantum computational advantage in noisy circuits [133, 143, 144], potentially motivating the inclusion of error mitigation in complexity theoretic arguments. Moreover, the exponential improvement in the fidelity score for $D \geq 2$ might indicate a method to foil "spoofing" algorithms that have been developed for unmitigated fidelity benchmarks in noisy random circuits [134].

These results also have implications for measurement-induced phase transitions in hybrid random circuits [121, 122, 136, 137]. Such models are not fault-tolerant because circuit-level depolarizing noise drives the system to a short-range correlated mixed state (it acts as a symmetry breaking field in the replica theory [51]). The addition of the antinoise terms considered here can restore the symmetries of the model on average, allowing for a stable ordered phase. Thus, our analysis indicates that MIPT for $D \geq 2$ can be made fault-tolerant via error mitigation techniques.

More broadly, the existence of error mitigation thresholds has important implications for near-term quantum simulation and quantum computing. A natural question is whether the threshold behavior observed here extends to other models. For example, in quantum simulation of Hamiltonian dynamics, one can apply a continuous time version of PEC [127]. An error mitigation threshold qualitatively similar to the one studied in this work should arise for chaotic Hamiltonian evolution with sufficiently strong interactions relative to the dissipation, raising the intriguing possibility of a rich interplay between the Hamiltonian and error mitigated dynamics. Similarly, error mitigation thresholds may naturally arise in more conventional quantum algorithms like Shor's factoring algorithm.

# Chapter A: Statistical Mechanical Mappings for Random Circuits

In this appendix chapter, I present a proof that uses a statistical mechanical mapping to make predictions about the probability distribution induced by random quantum circuits.

## A.1 Total Variation Distance of Noisy Random Circuit from Uniform Distribution

Consider a partially heralded noise model where first a random set of sites are selected after each layer of a 1D random circuit circuit independently with probability $p$. At each site $i$ in this random subset, a local dephasing channel $\mathcal{E}_i$ is applied with dephasing parameter $q$, where

$$\mathcal{E}_i(\rho) = (1-q)\rho + qZ_i\rho Z_i. \tag{A.1}$$

In the limit $p \to 1$, this becomes a standard local dephasing model with parameter $q$, while $q \to 1/2$ is equivalent to a model where a random set of sites are measured at rate $p$ in the $Z$-basis, but without keeping track of the measurement outcomes. For $p < 1$, we absorb the random locations of the dephasing events into the ensemble $\mathcal{B}$.

The "heralding" refers to the fact that the set of sites where the measurements occurred is known, but not the measurement outcomes. Note that this is different from a dephasing model where each site is uniformly dephased with dephasing parameter $pq$. In particular, the noise

locations act as an additional source of randomness in the model.

We focus on this noise model for two reasons. First, we would like to verify the intuition that noise acting during a random unitary circuit renders the output distribution "worthless" (close to the uniform distribution) after logarithmic depth [145], even though there are atypical circuits that can avoid the effects of the noise in a heralded dephasing model. The second motivation arises from the observation that when the measurement outcomes are also known, such models exhibit an entanglement transition in the conditional evolution of the quantum states in monitored quantum circuits. Our analysis of the heralded dephasing model proves that discarding the measurement outcomes, but maintaining knowledge of the noise locations, is enough to remove any signature of such entanglement transitions.

For a noisy Haar random circuit with this noise model, we prove an upper bound on the circuit-averaged total variation distance $\delta$ that is independent of the circuit architecture:

**Theorem 2.** *For a noisy Haar random circuit on any parallel circuit architecture with heralded dephasing noise at rate $p$ with the dephasing parameter $q$, we have the upper bound*

$$\mathbb{E}_{\mathcal{B}}[\delta] < \frac{3^{2/3}}{2} n^{1/3} e^{-\gamma p d/3}, \tag{A.2}$$

*where $\gamma = 8q(1-q)/3$.*

*Proof.* We start from Pinsker's inequality, which states that the total variation distance between distributions $P$ and $Q$ is related to the corresponding KL-divergence (the classical relative entropy) by the relation $\delta(P,Q) \leq \sqrt{D_{\mathrm{KL}}(P||Q)/2}$. The KL-divergence with respect to the uniform distribution $\mathcal{U}$ is given by $n \log 2 - H(P)$, where $H(P)$ is the Shannon entropy. Let $\mathcal{D}$ denote the distribution of measurements for a circuit. This gives us the following chain of inequality for

variation distance to the uniform distribution:

$$2\delta(\mathcal{D},\mathcal{U})^2 \leq D_{KL}\left(\mathcal{D}||\mathcal{U}\right) = n\log 2 - H(\mathcal{D}) \leq n\log 2 - H_2(\mathcal{D}), \tag{A.3}$$

where the last inequality follows from the fact that second Rényi entropy $H_2(\mathcal{D}) = -\log\left(\sum_x p_x^2\right)$ is less than or equal to the Shannon entropy $H(\mathcal{D}) = H_{\alpha\to 1}(\mathcal{D}) = -\sum_x p_x \log p_x$. We can now use Markov's inequality to bound the average TVD. For any $\epsilon \in [0,1]$, letting $\Pr_{\mathcal{B}}(\delta = \sigma)$ denote the probability *density* of the continuous variable $\delta$, we have

$$\mathbb{E}_{\mathcal{B}}(\delta) = \int_0^{\epsilon} \mathrm{d}\sigma\sigma \Pr_{\mathcal{B}}(\delta = \sigma) + \int_{\epsilon}^{1} \mathrm{d}\sigma\sigma \Pr_{\mathcal{B}}(\delta = \sigma) \leq \epsilon + \Pr_{\mathcal{B}}(\delta \geq \epsilon) \leq \epsilon + \frac{\mathbb{E}_{\mathcal{B}}(\delta^2)}{\epsilon^2}. \tag{A.4}$$

If $\mathbb{E}_{\mathcal{B}}(\delta^2)$ decays exponentially or faster with depth, i.e., $e^{-\gamma d}$ for some $\gamma > 0$, we can take $\epsilon = e^{-\gamma d/3}$ to ensure that $\mathbb{E}_{\mathcal{B}}(\delta)$ decays exponentially as $e^{-\gamma d/3}$. To show that the second moment of TVD must indeed decay exponentially with $d$, we calculate the expectation of A.1:

$$\mathbb{E}_{\mathcal{B}}[2\delta(\mathcal{D},\mathcal{U})^2] \leq n\log 2 - \mathbb{E}_{\mathcal{B}}(H_2(\mathcal{D})), = n\log 2 + \mathbb{E}_{\mathcal{B}}\left[\log\left(\sum_x p_x^2\right)\right], \leq n\log 2 + \log\mathbb{E}_{\mathcal{B}}\left[\sum_x p_x^2\right].$$

In the last inequality, we have used Jensen's inequality for concave functions $\mathbb{E}_{\mathcal{B}}[f(X)] \leq f(\mathbb{E}_{\mathcal{B}}[X])$. The term inside the expectation function, $\sum_x p_x^2$, is the collision probability. From 1, we have that the expectation of the collision probability is upper-bounded by $2^{-n}\exp[\frac{n}{3}e^{-\gamma pd}]$, where $\gamma = 8q(1-q)/3$. With this, we have

$$\mathbb{E}_{\mathcal{B}}[2\delta(\mathcal{D},\mathcal{U})^2] \leq n\log 2 + \log\left[2^{-n}\exp\left[\frac{n}{3}e^{-\gamma pd}\right]\right] = \frac{n}{3}e^{-\gamma pd}.$$

Thus, we have that the second moment of the TVD decays exponentially in circuit depth. The right hand side of A.4 is minimized at $\epsilon = (n/3)^{1/3} e^{-\gamma pd/3}$. This yields the desired bound

$$\mathbb{E}_{\mathcal{B}}(\delta) \leq \frac{3^{2/3}}{2} n^{1/3} e^{-\gamma pd/3}.$$

□

To complete the proof, it remains to prove the following lemma:

**Lemma 1.** *For a noisy Haar random circuit on any parallel circuit architecture with heralded dephasing noise at rate $p$ with the dephasing parameter $q$, we have the upper bound on the collision probability $Z$*

$$\mathbb{E}_{\mathcal{B}}[Z] = \mathbb{E}_{\mathcal{B}}\left[\sum_x p_x^2\right] \leq 2^{-n} \exp[\frac{n}{3} e^{-\gamma pd}], \tag{A.5}$$

*where* $\gamma = 8q(1-q)/3$.

To prove this bound, we make use of the statistical mechanics mapping method developed by [131].

## A.2 Proof: Collision Probability for Random Circuits with Heralded Dephasing

Here, we introduce the concepts that go into proving Lemma 1.

If $X$ is a random variable in $\{0,1\}^n$ denoting the measurement outcome of $n$ qubits after a

unitary $U \sim \mathcal{B}$, the collision probability of the random-circuit architecture is defined as

$$Z = \mathbb{E}_{\mathcal{B}} \left[ \sum_{x \in \{0,1\}^n} \Pr(X = x)^2 \right] = \mathbb{E}_{\mathcal{B}} \left[ \sum_{x \in \{0,1\}^n} p_U(x)^2 \right], \tag{A.6}$$

where $p_U(x)$ is the probability that the measurement result is $x$. If there is at least one gate for each qubit in a parallel circuit architecture with Haar-random gates, all measurement outcomes are equally random and, thus, there is a symmetry over them.

$$Z = \mathbb{E}_{\mathcal{B}} \left[ \sum_{x \in \{0,1\}^n} p_U(x)^2 \right] = 2^n \mathbb{E}_{\mathcal{B}} \left[ p_U(0^n)^2 \right], \tag{A.7}$$

where $0^n$ denotes the state $|00\ldots0\rangle$. Assuming that the input state is also $0^n$, the probability of measuring $0^n$ after the circuit is given by $\mathrm{tr}(|0^n\rangle \langle 0^n| U |0^n\rangle \langle 0^n| U^\dagger)$. To get the second moment of the probability distribution, we consider two copies of the circuit acting on two copies of the input state. Since the trace obeys $\mathrm{tr}(A \otimes B) = \mathrm{tr}(A)\,\mathrm{tr}(B)$, we get

$$\begin{aligned} Z = 2^n \mathbb{E}_{\mathcal{B}} \left[ p_U(0)^2 \right] &= 2^n \mathbb{E}_{\mathcal{B}}\, \mathrm{tr}[(|0^n\rangle \langle 0^n|)^{\otimes 2}\, U^{\otimes 2}\, (|0^n\rangle \langle 0^n|)^{\otimes 2}\, (U^\dagger)^{\otimes 2}], \\ &= 2^n\, \mathrm{tr} \left[ (|0^n\rangle \langle 0^n|)^{\otimes 2}\, \mathbb{E}_{\mathcal{B}} \left[ U^{\otimes 2}\, (|0^n\rangle \langle 0^n|)^{\otimes 2}\, (U^\dagger)^{\otimes 2} \right] \right]. \end{aligned} \tag{A.8}$$

For convenience, we denote the two-copy, Haar-averaged channel over $k$ qubits as $M_{U_k}$:

$$M_{U_k}[\rho] = \mathbb{E}_{\mathcal{B}} \left[ {U_k}^{\otimes 2} \rho ({U_k}^\dagger)^{\otimes 2} \right], \tag{A.9}$$

where $U_k$ is a unitary acting on $k$ qubits. To study noisy evolution, we define a dephasing noise

of strength $q$ given by the noise channel

$$\mathcal{E}[\rho] = (1-q)\rho + qZ\rho Z. \tag{A.10}$$

**Lemma 2.** *For a noisy Haar random circuit of depth $d$ on any parallel circuit architecture with heralded dephasing noise at rate $p$ with the dephasing parameter $q$, we have the upper bound on the expected collision probability*

$$\mathbb{E}_{\mathcal{B}}[Z] = \mathbb{E}_{\mathcal{B}}\Big[\sum_x p_x^2\Big] \leq 2^{-n}\exp[\frac{n}{3}e^{-\gamma p d}], \tag{A.11}$$

*where $\gamma = 8q(1-q)/3$.*

*Proof.* It is convenient to separate out the average over random locations of the dephasing events in the heralded dephasing model from the ensemble $\mathcal{B}$ (an ensemble of both gates and noise locations). We denote the ensemble of gates for a fixed set of locations $L$ by $\mathcal{B}_L$ and averages over the noise locations by $\mathbb{E}_{\mathcal{L}}$. We will show in Lemma 6 that given a random circuit ensemble $\mathcal{B}_L$ on a parallel circuit architecture with heralded dephasing noise and a fixed set of locations $L$, there exists another circuit ensemble $\mathcal{B}'_L$, with the gates drawn at random independently of $L$, composed solely of single-qubit gates and SWAP gates with an average collision probability $\mathbb{E}_{\mathcal{B}'_L}[Z]$ greater than or equal to the average collision probability of the original circuit $\mathbb{E}_{\mathcal{B}_L}[Z]$. Note, for every circuit in the new ensemble $C \in \mathcal{B}'_L$, we can append a network of SWAP gates to $C$ to return all qubits to their original positions. Adding these SWAP gates does not change the collision probability, since these gates only permute the support of the final probability distribution. We further break up the ensemble $\mathcal{B}'_L$ into an ensemble of single-qubit Haar random gates $\mathcal{B}'_1$ and the

random SWAP network $\mathcal{B}'_{\mathrm{SWAP}}$. The distribution of gates in the ensemble $\mathcal{B}'_1 \cup \mathcal{B}'_{\mathrm{SWAP}}$ is defined by taking every two-qubit gate for the circuits in $\mathcal{B}_L$ and replacing it with a SWAP gate or identity gate with equal probability on those sites, followed by Haar-random single-site gates on the two qubits. The joint distribution over SWAP networks and single-site gates is also conditionally independent, allowing us to commute averages over single-site gates, SWAP networks, and noise locations with each other.

Fixing a realization of SWAP gates and noise locations, we can then follow the path of a qubit, count the total number of dephasing events in that path and merge consecutive single-qubit gates without intervening noise locations. Since we are working with a parallel circuit architecture, there is never a case of consecutive dephasing events (there is always a single-qubit gate after each dephasing event). Let $t_i$ be the number of dephasing events on the path of qubit $i$. For the heralded dephasing model, we can write the random variable $t_i$ as a sum

$$t_i = \sum_{j=1}^{d} x_{ij}, \tag{A.12}$$

where $x_{ij} \in \{0, 1\}$ are independent, identically distributed Bernoulli random variables for each $i$ and $j$ with parameter $p$. We have $\mathbb{E}_{\mathcal{L}}[x_{ij}] = p$ and $\Pr_{\mathcal{L}}[x_{ij} = a, x_{kl} = b] = \Pr_{\mathcal{L}}[x_{ij} = a] \Pr_{\mathcal{L}}[x_{kl} = b]$ for every $ij \neq kl$.

After averaging over $\mathcal{B}'_1$ using Lemma 5, the final two-copy circuit-averaged state is given by

$$\bigotimes_{i=1}^{n} \left( M_{U_1} \circ \underbrace{(\mathcal{E} \circ M_{U_1}) \cdots \circ (\mathcal{E} \circ M_{U_1})}_{t_i} \right) [|0^n\rangle \langle 0^n|^{\otimes 2}] = \bigotimes_{i=1}^{n} \left[ \left( \frac{1}{12}(3 - \beta^{t_i}) \right) I + \frac{1}{6} \beta^{t_i} S \right], \tag{A.13}$$

where $\beta = 1 - 8q(1-q)/3$, and $I$ and $S$ are the $4 \times 4$ identity and SWAP operators, respectively. Using A.8 and noting that $\mathrm{tr}(I \left|0\right\rangle \left\langle 0\right|^{\otimes 2}) = \mathrm{tr}(S \left|0\right\rangle \left\langle 0\right|^{\otimes 2}) = 1$, the average collision probability for a fixed SWAP network and set of noise locations equals

$$\mathbb{E}_{\mathcal{B}'_1}[Z] = 2^n \prod_{i=1}^{n} \left[ \frac{1}{12}(3 - \beta^{t_i}) + \frac{1}{6}\beta^{t_i} \right] = 2^n \prod_{i=1}^{n} \frac{1}{2^2} \left[ 1 + \frac{1}{3}\beta^{t_i} \right] = \frac{1}{2^n} \prod_{i=1}^{n} \left[ 1 + \frac{1}{3}\beta^{t_i} \right]. \quad \text{(A.14)}$$

We now average over the noise locations using our assumption that the noise locations are uncorrelated with each other and the realization of the SWAP network.

$$\mathbb{E}_{\mathcal{L}}\mathbb{E}_{\mathcal{B}'_1}[Z] = \mathbb{E}_{\substack{t_i \\ 1 \le i \le n}} \left[ \mathbb{E}_{\mathcal{B}'_1}[Z] \right] = \frac{1}{2^n} \prod_{i=1}^{n} \left[ 1 + \mathbb{E}_{t_i} \left[ \frac{1}{3}\beta^{t_i} \right] \right] = \frac{1}{2^n} \prod_{i=1}^{n} \left[ 1 + \frac{1}{3} \prod_{j=1}^{d} \mathbb{E}_{x_{ij}} \left[ \beta^{x_{ij}} \right] \right]. \quad \text{(A.15)}$$

Using the fact that $x_{ij}$ are Bernoulli random variables, we can compute the expectation $\mathbb{E}_{x_{ij}} \left[ \beta^{x_{ij}} \right]$ as

$$\mathbb{E}_{x_{ij}} \left[ \beta^{x_{ij}} \right] = p\beta^1 + (1-p)\beta^0 = p\beta + (1-p) = 1 - p(1-\beta) = 1 - p\gamma, \quad \text{(A.16)}$$

where we have defined $\gamma = 1 - \beta$. Inserting this expectation in (A.15) and using 6, we get a bound on the average collision probability

$$\mathbb{E}_{\mathcal{B}}[Z] \le \mathbb{E}_{\mathcal{B}'}[Z] = \mathbb{E}_{\mathcal{B}'_{\mathrm{SWAP}}}\mathbb{E}_{\mathcal{L}}\mathbb{E}_{\mathcal{B}_{1'}}[Z] = \frac{1}{2^n} \left[ 1 + \frac{1}{3}(1 - p\gamma)^d \right]^n \le \frac{1}{2^n} \left[ 1 + \frac{1}{3} e^{-\gamma p d} \right]^n \le 2^{-n} \exp\left[ \frac{n}{3} e^{-\gamma p d} \right]. \quad \text{(A.17)}$$

Here, we used $\mathbb{E}_{\mathcal{B}}[Z] = \mathbb{E}_{\mathcal{L}}\mathbb{E}_{\mathcal{B}_L}[Z] \le \mathbb{E}_{\mathcal{B}'}[Z] := \mathbb{E}_{\mathcal{L}}\mathbb{E}_{\mathcal{B}'_L}[Z]$ in applying 6 in the first inequality. We also used the fact that, for any $x > 0$, $1 - x \le e^{-x}$ in the second inequality and $1 + x \le e^x$ in the third inequality.

□

**Lemma 5.** *Consider a random circuit consisting of $k$ dephasing error channels of strength $q$ sandwiched between $k+1$ single-qubit Haar-random gates (denoted by $U_1$). When this circuit acts on two copies of a single-qubit, the circuit-averaged state is given by*

$$M_{U_1} \circ \underbrace{(\mathcal{E} \circ M_{U_1}) \cdots \circ (\mathcal{E} \circ M_{U_1})}_{k}[|0\rangle \langle 0|^{\otimes 2}] = \frac{1}{12}(3-\beta^k)I + \frac{1}{6}\beta^k S, \tag{A.18}$$

*where $\beta = 1 - \frac{8}{3}q(1-q)$, and $I$ and $S$ are the $4 \times 4$ identity and SWAP operators, respectively.*

*Proof.* We first make an observation that $M_{U_1}[\rho] = M_{U_1} \circ M_{U_1}[\rho]$, that is, one can split a Haar-random gate into two Haar-random gates without changing the statistics. In the circuit described above, leaving the two terminal unitary gates intact, we split all inner gates into two. This lets us treat the circuit as a repeating sequence of $n$ units of the composite channel $\tilde{M}_{U_1,\mathcal{E}} = M_{U_1} \circ \mathcal{E} \circ M_{U_1}$.

From Ref. [131], we know the following:

$$M_{U_1}[\sigma] = \frac{1}{3}\left(\mathrm{tr}(\sigma) - 2^{-1}\,\mathrm{tr}(\sigma S)\right) I + \frac{1}{3}\left(\mathrm{tr}(\sigma S) - 2^{-1}\,\mathrm{tr}(\sigma)\right) S. \tag{A.19}$$

If we follow this gate by a dephasing error channel, we get

$$\begin{aligned}
\mathcal{E} \circ M_{U_1}[\sigma] &= \frac{1}{3}\left(\mathrm{tr}(\sigma) - 2^{-1}\,\mathrm{tr}(\sigma S)\right)\mathcal{E}[I] + \frac{1}{3}\left(\mathrm{tr}(\sigma S) - 2^{-1}\,\mathrm{tr}(\sigma)\right)\mathcal{E}[S], \\
&= \frac{1}{3}\left(\mathrm{tr}(\sigma) - 2^{-1}\,\mathrm{tr}(\sigma S)\right) I \\
&\quad + \frac{1}{3}\left(\mathrm{tr}(\sigma S) - 2^{-1}\,\mathrm{tr}(\sigma)\right)\left((1-q)^2 S + 2q(1-q)(ZI)S(ZI) + q^2(ZZ)S(ZZ)\right), \\
&= \frac{1}{3}\left(\mathrm{tr}(\sigma) - 2^{-1}\,\mathrm{tr}(\sigma S)\right) I \\
&\quad + \frac{1}{3}\left(\mathrm{tr}(\sigma S) - 2^{-1}\,\mathrm{tr}(\sigma)\right)\left(((1-q)^2 + q^2)S + 2q(1-q)(ZI)S(ZI)\right).
\end{aligned}$$

We follow this channel by another single-qubit random gate to finish the composite block. First we observe that $M_{U_1}[I] = I$ and $M_{U_1}[S] = S$. Similarly using (A.19) together with the fact that $\mathrm{tr}[S] = 2, \mathrm{tr}[(IZ)S(IZ)S] = 0$,

$$M_{U_1}[(IZ)S(IZ)] = \frac{2}{3}I - \frac{1}{3}S.$$

The composite channel thus gives

$$\tilde{M}_{U_1,\mathcal{E}}[\sigma] = \frac{1}{3}\left(\mathrm{tr}(\sigma) - 2^{-1}\,\mathrm{tr}(\sigma S)\right) M_{U_1}[I] + \tag{A.20}$$

$$\frac{1}{3}\left(\mathrm{tr}(\sigma S) - 2^{-1}\,\mathrm{tr}(\sigma)\right)\left(((1-q)^2+q^2)M_{U_1}[S] + 2q(1-q)M_{U_1}[(ZI)S(ZI)]\right),$$

$$= \frac{1}{3}\left(\mathrm{tr}(\sigma) - 2^{-1}\,\mathrm{tr}(\sigma S)\right) I \tag{A.21}$$

$$+ \frac{1}{3}\left(\mathrm{tr}(\sigma S) - 2^{-1}\,\mathrm{tr}(\sigma)\right)\left(((1-q)^2+q^2)S + 2q(1-q)\left(\frac{2}{3}I - \frac{1}{3}S\right)\right),$$

$$= \frac{1}{3}\left(\mathrm{tr}(\sigma) - 2^{-1}\,\mathrm{tr}(\sigma S) + \underbrace{\frac{4}{3}q(1-q)}_{\alpha}\left(\mathrm{tr}(\sigma S) - 2^{-1}\,\mathrm{tr}(\sigma)\right)\right) I + \tag{A.22}$$

$$\frac{1}{3}\left(\mathrm{tr}(\sigma S) - 2^{-1}\,\mathrm{tr}(\sigma)\right)\underbrace{\left(1 - \frac{8}{3}q(1-q)\right)}_{\beta} S,$$

$$= \frac{1}{3}\left(\mathrm{tr}(\sigma) - 2^{-1}\,\mathrm{tr}(\sigma S) + \alpha\left(\mathrm{tr}(\sigma S) - 2^{-1}\,\mathrm{tr}(\sigma)\right)\right) I + \frac{1}{3}\left(\mathrm{tr}(\sigma S) - 2^{-1}\,\mathrm{tr}(\sigma)\right)\beta S. \tag{A.23}$$

The composite sum returns a state of the form $aI + bS$. Acting on this state with other composite blocks only changes the coefficients $a$ and $b$. In fact, we can work out exactly how $a$ and $b$ change after each block. Knowing that $\mathrm{tr}(aI + bS) = 4a + 2b$ and $\mathrm{tr}(S(aI + bS)) = 2a + 4b$, we get

$$\tilde{M}_{U_1,\mathcal{E}}[aI + bS] = \frac{1}{3}\left(3a + \alpha(3b)\right) I + \frac{1}{3}(3b)\beta S = (a + \alpha b)I + (\beta b)S. \tag{A.24}$$

The first composite acts on the state $|0\rangle\langle 0|^{\otimes 2}$. Knowing that $\mathrm{tr}[|0\rangle\langle 0|^{\otimes 2}] = \mathrm{tr}(S\,|0\rangle\langle 0|^{\otimes 2}) = 1$,

and using A.23,

$$\tilde{M}_{U_1,\mathcal{E}}[|0\rangle\langle 0|^{\otimes 2}] = \frac{1}{3}\left(1-2^{-1}+\alpha\left(1-2^{-1}\right)\right)I + \frac{1}{3}\left(1-2^{-1}\right)\beta S = \frac{1}{6}(1+\alpha)\,I + \frac{1}{6}\beta S. \tag{A.25}$$

We take this state and apply another $k-1$ composite channels (since there are $k$ in total). We can calculate the final state recursively using A.24:

$$\tilde{M}_{U_1,\mathcal{E}}\circ\cdots\circ\tilde{M}_{U_1,\mathcal{E}}[|0\rangle\langle 0|^{\otimes 2}] = \frac{1}{6}\left[1+\alpha+\alpha\sum_{i=1}^{k-1}\beta^i\right]I + \frac{1}{6}\beta^k S = \frac{1}{12}(3-\beta^k)I + \frac{1}{6}\beta^k S. \tag{A.26}$$

This proves the lemma. □

It now remains to prove the following lemma, which lets us put a bound on the average collision probability in Lemma 1.

**Lemma 6.** *Consider a random quantum circuit ensemble on a parallel architecture, $\mathcal{B}_L$, with Haar-random two-qubit gates and heralded dephasing noise with a fixed set of noise locations $L$. There is a procedure to obtain another circuit ensemble $\mathcal{B}'_L$ with gates drawn randomly independently of $L$, composed solely of noisy single-qubit channels and SWAP gates, with an equal or higher average collision probability, i.e., $\mathbb{E}_{\mathcal{B}_L}[Z] \leq \mathbb{E}_{\mathcal{B}'_L}[Z]$.*

*Proof.* Note that without loss of generality, we can assume that every two-qubit Haar-random gate is preceded by Haar-random single-qubit gates on both incoming lines, since the two situations correspond to the same ensemble. When the noise is heralded, the circuit consists of three kinds of two-qubit gates:

1. Type A, where the two-qubit gate is noiseless.

2. Type B, where one of the two outgoing legs of the gate undergoes dephasing, followed by a single-qubit random gate.

3. Type C, where both outgoing legs undergo dephasing followed by single-qubit gates on both legs.

We will analyze each of these types separately and start with a brief review of the methods of Ref. [131] for noiseless random circuits. In Ref. [131], it was shown that taking a two copies of an $n$-qubit state $|0^n\rangle\langle 0^n|^{\otimes 2}$, acted on by a Haar random circuit $U \otimes U$, and averaged over the unitaries leads to a density matrix that can be represented by a linear combination of length-$n$ configurations in $\{I, S\}^n$ where $I$ and $S$ are the $4 \times 4$ identity and SWAP matrices. Any two-qubit unitary gate takes a linear combination to another linear combination. More precisely, for $\vec{\gamma} \in \{I, S\}^n$, a two-qubit unitary channel $M_{U_2}$, acting on qubits $i$ and $j$, transforms it to

$$M_{U_2}[\vec{\gamma}] = M_{U_2}\left[\bigotimes_{a=1}^{n} \gamma_a\right] = \sum_{\vec{\nu}\in\{I,S\}^n} M_{U_2}^{\vec{\gamma},\vec{\nu}} \bigotimes_{b=1}^{n} \nu_b =: \sum_{\vec{\nu}\in\{I,S\}} M_{U_2}^{\vec{\gamma},\vec{\nu}} \vec{\nu}, \tag{A.27}$$

where $M_{U_2}^{\vec{\gamma},\vec{\nu}}$ are matrix elements determined by qubit locations $i, j$

$$M_{U_2}^{\vec{\gamma},\vec{\nu}} = \begin{cases} 1 & \text{if } \gamma_i = \gamma_j \text{ and } \vec{\gamma} = \vec{\nu}, \\ 2/5 & \text{if } \gamma_i \neq \gamma_j \text{ and } \nu_i = \nu_j \text{ and } \gamma_k = \nu_k \; \forall k \in [n]/[i, j], \\ 0 & \text{otherwise.} \end{cases} \tag{A.28}$$

Therefore, a state can be represented as a linear combination of trajectories of the configuration strings, with each trajectory weighted according to A.28. Furthermore, since $\mathrm{tr}(\vec{\gamma}\,|0^n\rangle\langle 0^n|^{\otimes 2}) = 1$ for each $\vec{\gamma} \in \{I, S\}^n$, the collision probability can be, similarly, written as a sum over weighted

trajectories. More precisely, the average collision probability of a circuit with $s$ gates,

$$\mathbb{E}_{\mathcal{B}_L}[Z_s] = \frac{1}{3^n} \sum_{\gamma \in \{I,S\}^{n \times s}} \prod_{t=1}^{s-1} M_{U_2}^{\vec{\gamma}_t, \vec{\gamma}_{t+1}} = \frac{1}{3^n} \sum_{\gamma \in \{I,S\}^{n \times s}} \prod_{t=1}^{s-1} \mathrm{wt}(\gamma). \tag{A.29}$$

In the above, the factor $1/3^n$ comes from the fact that after the first layer of Haar-random single-qubit gates, the Haar-averaged two-copy state is given by $\frac{1}{6^n} \sum_{\vec{\gamma} \in \{I,S\}^n} \vec{\gamma}$, the uniform mixture of all configurations in $\{I, S\}^n$. Also, the weight $\mathrm{wt}(\gamma)$ of a configuration is defined as the product of the matrix elements $M_{U_2}^{\vec{\gamma}_t, \vec{\gamma}_{t+1}}$.

Now, we modify this construction to account for noise. We add one more gate of Type $A$, $B$ or $C$ to this circuit. Since all three types are two-qubit gates, we let $[i, j]$ denote the qubits the gate acts on. We can isolate the qubits $[i, j]$ from the decomposition in A.29 as follows:

$$\mathbb{E}_{\mathcal{B}_L}[Z_s] = \frac{1}{3^n} \left[ \sum_{\substack{\gamma \in \{I,S\}^{ns} \\ \vec{\gamma}_{ij}^s = II}} \mathrm{wt}(\gamma) + \sum_{\substack{\gamma \in \{I,S\}^{ns} \\ \vec{\gamma}_{ij}^s = IS}} \mathrm{wt}(\gamma) + \sum_{\substack{\gamma \in \{I,S\}^{ns}) \\ \vec{\gamma}_{ij}^s = SI}} \mathrm{wt}(\gamma) + \sum_{\substack{\gamma \in \{I,S\}^{ns} \\ \vec{\gamma}_{ij}^s = SS}} \mathrm{wt}(\gamma) \right]. \tag{A.30}$$

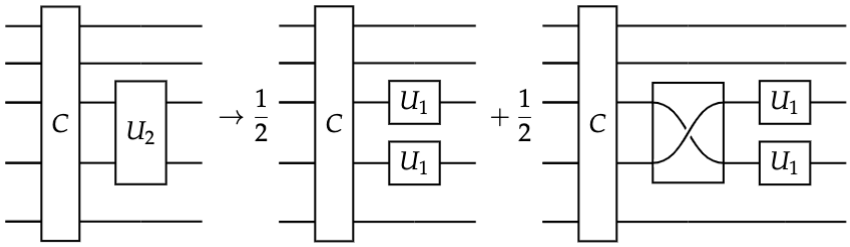


Figure A.1: Circuit of Type A.

Type A: When we add a noiseless two-qubit gate, the bit-strings transform according to A.28. Zooming on qubits $i$ and $j$, the trajectories evolve as follows:

$$M_{U_2}[II] = II \qquad M_{U_2}[SS] = SS \qquad M_{U_2}[IS, SI] = \frac{2}{5}(II + SS). \tag{A.31}$$

The trajectories for which $\vec{\gamma}_{ij}^{\,s} \in \{II, SS\}$ have their weights unchanged. The trajectories for which $\vec{\gamma}_{ij}^{\,s} \in \{IS, SI\}$ have their weights changed by $4/5$ (the trajectory splits two ways, each weighted by $2/5$).

$$\mathbb{E}_{\mathcal{B}_L}[Z_{s+1}] = \frac{1}{3^n}\left[\sum_{\substack{\gamma\in\{I,S\}^{n(s+1)}\\ \vec{\gamma}_{ij}^{\,s}=II}} \mathrm{wt}(\gamma) + \frac{4}{5}\sum_{\substack{\gamma\in\{I,S\}^{n(s+1)}\\ \vec{\gamma}_{ij}^{\,s}=IS}} \mathrm{wt}(\gamma) + \frac{4}{5}\sum_{\substack{\gamma\in\{I,S\}^{n(s+1)}\\ \vec{\gamma}_{ij}^{\,s}=SI}} \mathrm{wt}(\gamma) + \sum_{\substack{\gamma\in\{I,S\}^{n(s+1)}\\ \vec{\gamma}_{ij}^{\,s}=SS}} \mathrm{wt}(\gamma)\right]. \tag{A.32}$$

If, instead, we consider a modified random circuit where the two-qubit gate consists of a SWAP gate or identity with probability 1/2 followed by Haar random single-qubit gates, all the trajectories retain their original weights since the collision probability is invariant under a SWAP gate and $M_{U_1}[I] = I$ and $M_{U_1}[S] = S$. Denoting the locally modified circuit ensemble with the same set of noise locations by $\mathcal{B}'_L$, we have, in both cases,

$$\mathbb{E}_{\mathcal{B}'_L}[Z_{s+1}] = \mathbb{E}_{\mathcal{B}_L}[Z_s] \implies \mathbb{E}_{\mathcal{B}'_L}[Z_{s+1}] > \mathbb{E}_{\mathcal{B}_L}[Z_{s+1}]. \tag{A.33}$$

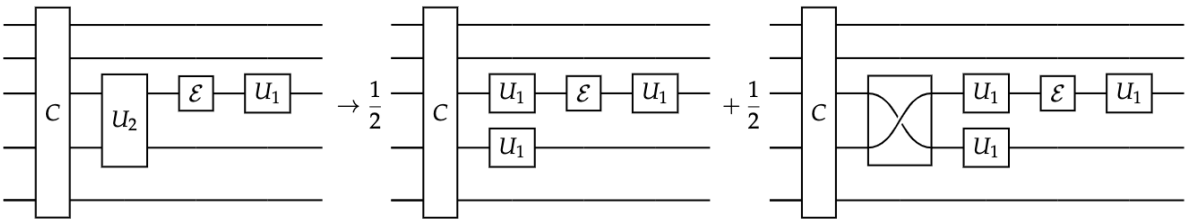


Figure A.2: Circuit of Type B.

Type B: The gate of Type B has a noiseless two-qubit gate followed by dephasing on one of the outgoing legs. The dephasing is also followed by a single-qubit random gate. To simplify things, we first understand the effect of the channel $M_{U_1} \otimes \mathcal{E}$ on $I$ and $S$. Of course, $M_{U_1} \circ \mathcal{E}[I] = I$, since neither the error nor the random gate has any effect on the identity matrix. However, for $S$, we get

$$M_{U_1}^{(i)} \circ \mathcal{E}^{(i)}[S] = M_{U_1}[(1-q)^2 S + q(1-q)(IZ)S(IZ) + q(1-q)(ZI)S(ZI) + q^2 S], \quad \text{(A.34)}$$

$$= \alpha I + \beta S, \quad \text{(A.35)}$$

with $\alpha = 4q(1-q)/3, \beta = 1 - 8q(1-q)/3$. Without losing generality, we assume that the dephasing happens on gate $i$, and the dephasing channel is denoted by $\mathcal{E}$. We now tabulate the effect of this composite channel:

$$M_{U_1}^{(i)} \circ \mathcal{E}^{(i)} \circ M_{U_2}[II] = II, \quad \text{(A.36)}$$

$$M_{U_1}^{(i)} \circ \mathcal{E}^{(i)} \circ M_{U_2}[SS] = \alpha IS + \beta SS, \quad \text{(A.37)}$$

$$M_{U_1}^{(i)} \circ \mathcal{E}^{(i)} \circ M_{U_2}[IS, SI] = M_{U_1}^{(i)}\left[\frac{2}{5}(II + SS)\right] = \frac{2}{5}(II + \alpha IS + \beta SS). \quad \text{(A.38)}$$

The average collision probability of the new circuit is given by

$$\mathbb{E}_{\mathcal{B}_L}[Z_{s+1}] = \frac{1}{3^n}\left[\sum_{\vec{\gamma}_{ij}^s = II} \text{wt}(\gamma) + \frac{2}{5}(1+\alpha+\beta)\left(\sum_{\vec{\gamma}_{ij}^s = IS} \text{wt}(\gamma) + \sum_{\vec{\gamma}_{ij}^s = SI} \text{wt}(\gamma)\right) + (\alpha+\beta)\sum_{\vec{\gamma}_{ij}^s = SS} \text{wt}(\gamma)\right]. \quad \text{(A.39)}$$

Using the same locally modified circuit ensemble as above, we obtain

$$M_{U_1}^{(i)} \circ \mathcal{E}^{(i)} \circ M_{U_2} \to \frac{1}{2} M_{U_1}^{(i)} \circ \mathcal{E}^{(i)} \circ M_{U_1}^{(i)} \circ M_{U_1}^{(j)} + \frac{1}{2} M_{U_1}^{(i)} \circ \mathcal{E}^{(i)} \circ M_{U_1}^{(i)} \circ M_{U_1}^{(j)} \circ \text{SWAP} \quad \text{(A.40)}$$

$$= \frac{1}{2} M_{U_1}^{(i)} \circ \mathcal{E}^{(i)} \circ M_{U_1}^{(i)} \circ M_{U_1}^{(j)} + \frac{1}{2} M_{U_1}^{(j)} \circ \mathcal{E}^{(j)} \circ M_{U_1}^{(j)} \circ M_{U_1}^{(i)}. \quad \text{(A.41)}$$

Under this new composite channel, the bit-strings evolve as follows:

$$II \to II, \qquad SS \to \beta SS + \frac{\alpha}{2}(IS + SI), \qquad IS \to \frac{1}{2}(IS + \alpha II + \beta IS), \qquad SI \to \frac{1}{2}(\alpha II + \beta SI + SI). \quad \text{(A.42)}$$

The collision probability of the modified circuit is given by

$$\mathbb{E}_{\mathcal{B}'_L}[Z_s] = \frac{1}{3^n} \left[ \sum_{\vec{\gamma}_{ij}^s = II} \text{wt}(\gamma) + \frac{1}{2}(1 + \alpha + \beta) \left( \sum_{\vec{\gamma}_{ij}^s = IS} \text{wt}(\gamma) + \sum_{\vec{\gamma}_{ij}^s = SI} \text{wt}(\gamma) \right) + (\alpha + \beta) \sum_{\vec{\gamma}_{ij}^s = SS} \text{wt}(\gamma) \right]. \quad \text{(A.43)}$$

Since $2/5 < 1/2$, we have $Z'_{s+1} > Z_{s+1}$.

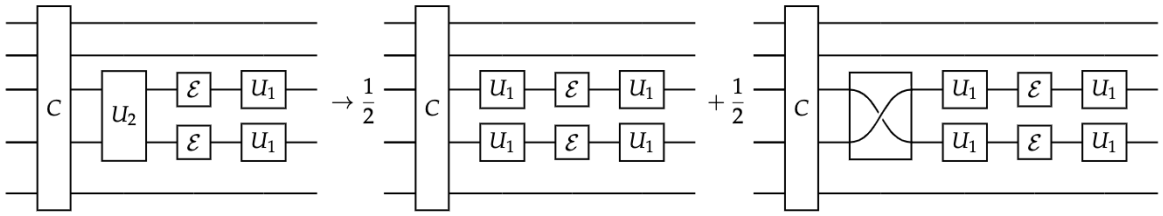


Figure A.3: Circuit of Type C.

Type C: These gates have dephasing noise on both legs. The noise is followed by single-qubit gates for both legs. The combined channel has the form $M_{U_1}^{(j)} \circ \mathcal{E}^{(j)} \circ M_{U_1}^{(i)} \circ \mathcal{E}^{(i)} \circ M_{U_2}$. The

bit-strings evolve as follows:

$$II \to II, \qquad SS \to \alpha^2 II + \alpha\beta IS + \alpha\beta SI + \beta^2 SS \tag{A.44}$$

$$IS \to \frac{2}{5}((1+\alpha^2)II + \alpha\beta IS + \alpha\beta SI + \beta^2 SS). \tag{A.45}$$

The average collision probability is thus given by

$$\mathbb{E}_{\mathcal{B}_L}[Z_{s+1}] = \frac{1}{3^n}\left[\sum_{\vec{\gamma}_{ij}^s=II} \text{wt}(\gamma) + \frac{2}{5}\left(1+(\alpha+\beta)^2\right)\left(\sum_{\vec{\gamma}_{ij}^s=IS} \text{wt}(\gamma) + \sum_{\vec{\gamma}_{ij}^s=SI} \text{wt}(\gamma)\right) + (\alpha+\beta)^2 \sum_{\vec{\gamma}_{ij}^s=SS} \text{wt}(\gamma)\right]. \tag{A.46}$$

If instead we replace the two-qubit gate with two single-qubit Haar random gates preceded by a SWAP gate with probability 1/2 (as shown in the diagram above), we get channels of the form $M_{U_1}^{(j)} \circ \mathcal{E}^{(j)} \circ \mathcal{E}^{(i)} \circ M_{U_1}^{(j)} \circ \mathcal{E}^{(i)} \circ M_{U_1}^{(i)} \circ \frac{1}{2}(SWAP + \mathbb{I})$, which, up to the SWAP gate, is same as the composite channel in Lemma 5 applied to both qubits. The states evolve as

$$II \to II, \qquad SS \to \alpha^2 II + \alpha\beta IS + \alpha\beta SI + \beta^2 SS$$

$$IS \to \alpha II + \frac{\beta}{2}(IS+SI), \qquad SI \to \alpha II + \frac{\beta}{2}(SI+IS).$$

The collision probability of the modified circuit is thus

$$\mathbb{E}_{\mathcal{B}'_L}[Z_{s+1}] = \frac{1}{3^n}\left[\sum_{\vec{\gamma}_{ij}^s=II} \text{wt}(\gamma) + (\alpha+\beta)\left(\sum_{\vec{\gamma}_{ij}^s=IS} \text{wt}(\gamma) + \sum_{\vec{\gamma}_{ij}^s=SI} \text{wt}(\gamma)\right) + (\alpha+\beta)^2 \sum_{\vec{\gamma}_{ij}^s=SS} \text{wt}(\gamma)\right]. \tag{A.47}$$

Since $(\alpha+\beta) = 1+4q(1-q)/3$, $\alpha+\beta \in [1, 4/3] \subset (\frac{1}{2}, 2)$, we have that $(2/5)\left(1+(\alpha+\beta)^2\right) < (\alpha+\beta)$, and therefore $Z'_{s+1} > Z_s$.

Starting from the input state, we can use the replacement procedure discussed above to

iteratively define a new circuit ensemble $\mathcal{B}'_L$ with the gates drawn at random independently of $L$, composed solely of single-qubit gates and SWAP gates, that has an equal or higher gate-averaged collision probability. This concludes the proof of the lemma. □

# Chapter B: Supplementary Material: Measurement-Induced Purification Phase Transition

## B.1 Measurement Protocol

In our circuit ensemble, each gate after the scrambling layer is followed by a probabilistic measurement. Given the constraints of the hardware, we choose a measurement strategy that reduces the number of measurements. In addition, the ensemble generated with our measurement strategy scales to system sizes that are beyond the reach of available hardware and can only be studied with numerical simulations.

We maintain a list $\mathcal{M}$ which is initialized to all system qubits in the beginning of the circuit. After each gate, we measure one of the qubits involved in the gate with probability $p$. Having decided to perform a measurement after a XX gate, we randomly choose the qubit to measure and the basis of measurement. If both qubits participating in the XX gate are in $\mathcal{M}$, we randomly select one with probability half and measure it in $X$ basis with probability $p_x$ and in $Z$ basis with probability $1 - p_x$. If only one of the qubits is in $\mathcal{M}$, we measure that qubit (in the $X$ basis with probability $p_x$ and in the Z basis with probability $(1 - p_x)$. If neither qubit is in $\mathcal{M}$, we do not measure any. Measurement outcomes in Clifford circuits are deterministic or are equally likely to be zero or one. In the absence of noise, measuring a qubit with a deterministic outcome

has no effect on the purification of the reference. As a result, we only measure qubits with non-deterministic outcomes. Additionally, after each physically performed measurement, we remove the measured qubit from $\mathcal{M}$. Once $|\mathcal{M}| = L - 4$, we reinitialize the list with all the qubits in the system. With a low measurement probability, $p = 0.15$, used in our experiment the number of measurements in the circuits investigated are less than 4, and thus the the list $\mathcal{M}$ need not be reinitialized. This ensures that no system qubit in the experiment is measured more than once.

## B.2 Scrambling Unitary

A scrambling unitary, $U_S$, is applied after the system is entangled with the reference, before the random time evolution begins. The scrambling unitary consists of $4$ layers: odd-numbered layers are composed of single-qubit operations on each qubit and even-numbered layers are composed of fully entangling XX($\pi/4$) gates on $L/2$ random qubit-pairs.

## B.3 Raw Data and Thresholding

Data presented in the main text Fig. 2.4A is presented after binning via a threshold. Fig. B.1 shows histograms of the outcomes for all circuits with each entropy averaged over the outcome of 1000 shots per circuit. Furthermore, Fig. B.2 shows the average classical entropy over all circuits for each system size and $p_x$ value. These average are clearly much higher than simulation.

The primary reason for the discrepancy between the simulations and the experimental data is that the simulations do not include noise. When including realistic noise sources in the simulations (see Appendix B.6), such as dephasing or gate amplitude errors, we find that the entropy outcomes are pushed to higher values. Nevertheless, we see in the data for L=4 and L =

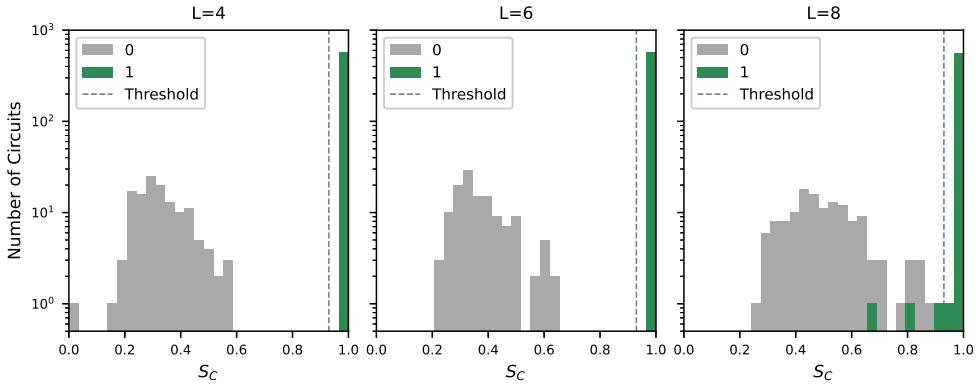


Figure B.1: All raw outcomes of SC in study of phases (main text Fig. 2.4). The legend indicates the simulated expected outcome for that circuit. The bin size is .033 and $S_C = .93$ (dashed line) is used as a threshold for all the data.

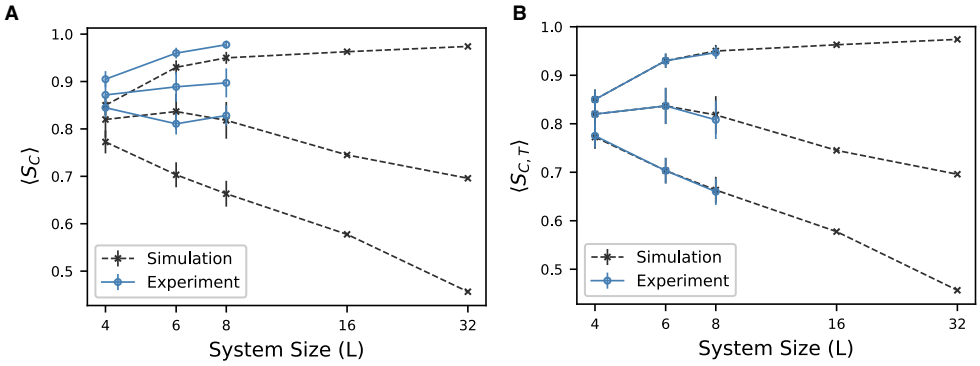


Figure B.2: (A) Raw average of all circuit outcomes without thresholding applied. (B) Thresholded data with extended simulations showing expected behavior up to L=32

6 that there is a clear separation observed in the entropy values for circuits which are mixed or pure (Fig. B.6). This separation is also evident in Fig. 2.1B, with the clear jump from mixed to pure in the evolution of the circuit.

We can use these properties of the circuits to mitigate noise effects. In the final data processing, we assume a Gaussian distribution of expected $S_C = 0$ circuit outcomes and $S_C = 1$ circuit outcomes and find their intersection, which is used as a threshold at $S_C = 0.93$. Circuit outcomes below the threshold are counted as 0 and outcomes above are counted as 1. We find three thresholded circuit outcomes disagree with the simulated expected value for that circuit,

for an error of 3/699 circuits for the $L = 8$ case. Fig. B.2 shows the result after all processing alongside simulations of the exact circuits for sizes $L = (4, 6, 8)$ and representative samples for sizes $L = (16, 32)$. The same threshold is used for all system sizes.

## B.4 Feedback Circuit

In order to reduce the number of circuits needed to evaluate $S_Q$, we append a feedback circuit to the end of each circuit that is expected to purify. The feedback uses single-qubit rotations and a circuit of CNOT gates between the reference and measurement ancillae to disentangle it from the measurement ancillae (Methods). With this addition, we replace measurement of $S_Q$ with the classical entropy $S_C$, and eliminate the need to measure in the $x$-basis and $y$-basis.

The feedback circuit is added at the end to disentangle the reference from the ancillae qubits. In the pure phase, the reference qubit purifies in one of $x$, $y$ or $z$ bases and its state (0 or 1) depends on the projections induced upon the measurement ancillae. The basis of purification can be anticipated with classical simulation of the Clifford circuit. A single-qubit rotation is performed on the reference qubit to ensure that it returns to the $z$-basis following purification. Since we do not have access to the measurement outcome until the very end of the circuit, we construct a logic circuit, consisting of CNOT gates, to ensure that the reference qubit purifies to the zero state. This is done by classically anticipating the entanglement between measurement ancillae and reference qubit, then generating a sequence of CNOT gates to disentangle the reference.

For example, in the batch $L = 4, p_x = 0$, circuit $\#45$ purifies the reference in the $x$-basis. There are three measurements. The outcomes of the measurement ancillae and the reference qubit are related by the truth table in Fig. B.4.

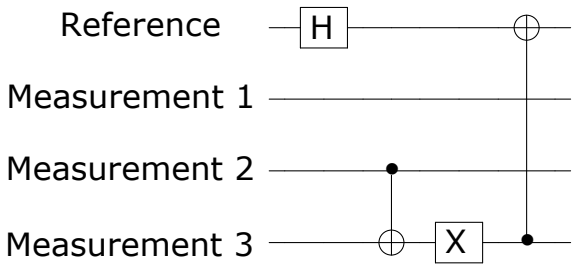


Figure B.3: Representative Example of a Feedback Circuit #45

| Measurement Record | Reference State |
|---|---|
| 001<br>010<br>101<br>110 | 0 |
| 000<br>011<br>100<br>111 | 1 |

Figure B.4: Truth table for outcomes of measurement ancillae and reference qubit for the circuit in Fig. B.3.

## B.5 Critical Scaling Theory

Our method for locating the critical point in these all-to-all models is illustrated in Fig. B.5. For $p_x \sim p_{xc}$, we can run the dynamics out to a time where $\langle S_Q(t) \rangle$ exhibits a simple exponential decay $\propto e^{-t/\tau}$. We then use least squares fitting to find the exponential decay rate $\tau$ for each value of $p_x$ and $L$. Deep in the mixed phase, $\tau$ diverges exponentially with $L$ [48], while in the pure phase $\tau$ approaches a constant independent of system size. At the critical point ($p = p_{xc}$), $\tau \sim L^z$, where $z$ is the dynamical critical exponent. Thus, we can estimate $p_{xc}$ by looking for the value of $p_x$ where $\tau(L)$ goes through an inflection point on a log-log plot. This behavior is illustrated in Fig. B.5B for the model with $p = 0.15$ and $|\mathcal{M}| \geq L - 4$). Near $p_x = 0.7 - 0.75$, we see that the decay rate $\tau$ grows as power law $L^{1/5}$ over the given range of sizes. This value of

$z = 1/5$ is consistent with the scaling one would expect from mean-field percolation. The close ties between these phase transitions and percolation have been noted in past works. Notably, for the Hartley entropy of Haar random circuits with measurements, there is an exact mapping to a percolation problem in the circuit geometry [45]. In the all-to-all setting considered here, this mapping also predicts $z = 1/5$.

Using this estimate for $z$, we can accurately measure the critical point $p_{xc}$ and critical exponent $\nu$ of the purification transition using the method illustrated in Fig. 3B. We hypothesize a scaling form for $\tau = L^z f[(p_x - p_{xc})L^{z/\nu}]$, which predicts that a crossing will appear with increasing sizes when plotting $\tau/L^z$ vs $p_x$. We see consistent results with this scaling assumption in Fig. 3B, from which we locate $p_{xc} = 0.72(1)$. A similar analysis was used for other values of $p \neq 0.15$ to extract the phase diagram in Fig. 2.3A. After locating $p_{xc}$, we then collapse the data as shown in the inset to Fig. 2.4B to obtain an estimate $\nu = 1/2$, which is also consistent with the predication from mean-field percolation. We leave a more detailed analysis of the critical properties of this model for future work.

## B.6 Noise Model

For the noisy simulation, we assume a simple model of XX-gate crosstalk, which is the dominant error mechanism in this work. The crosstalk value is predicted from the measured single-qubit Rabi crosstalk and the participation matrix for each gate [63]. With an increase of 50% above the predicted crosstalk value, we find that the noisy simulation is qualitatively similar to the experimental results. Such an increase could easily be caused by a shift in the ion positions relative to the individual-addressing beams, since the addressing crosstalk increases sharply for

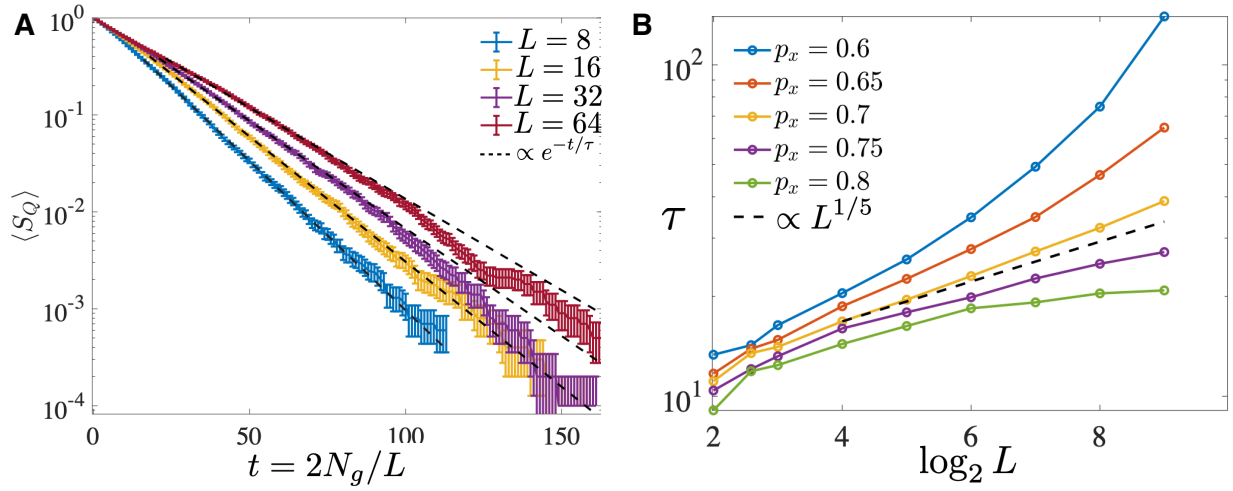


Figure B.5: (A) Late time decay of $\langle S_Q \rangle$ showing the exponential decay regime used to extract the decay rate $\tau$. Here, we took $(p, p_x) = (0.15, 0.7)$ near the critical point. (B) Scaling of $\tau$ vs $L$ for different values of $p_x$ at $p = 0.15$. We can estimate $p_{xc}$ and extract $z$ by looking for the inflection point in this family of curves and fitting the slope

small ion displacements from their optimal positions. A sample noisy simulation is shown in Fig. B.6 for the case of $L = 8$ and $p_x = 1$. Any additional noise that decoheres the state of the reference or system will further shift the distribution of outcome entropies upwards, towards the mixed state. Other noise mechanisms that likely contribute to the shift observed in the data include $T_2$ dephasing, random over/under rotation errors caused by beam position fluctuations, spurious entanglement of qubits with the axial modes of the ion chain, and SPAM errors.

## B.7 Error Mitigation

An interesting aspect of noiseless stabilizer circuits is that measurements of Pauli operators often have deterministic expectation values. We can use this fact to aid error mitigation of the noisy implementation of these circuits. As we scale the system to larger sizes or higher circuit depths, this type of error mitigation may become useful. Here, we describe those strategies and show data from Fig. 1B without and with these error mitigation techniques (Fig. B.7A-B). For

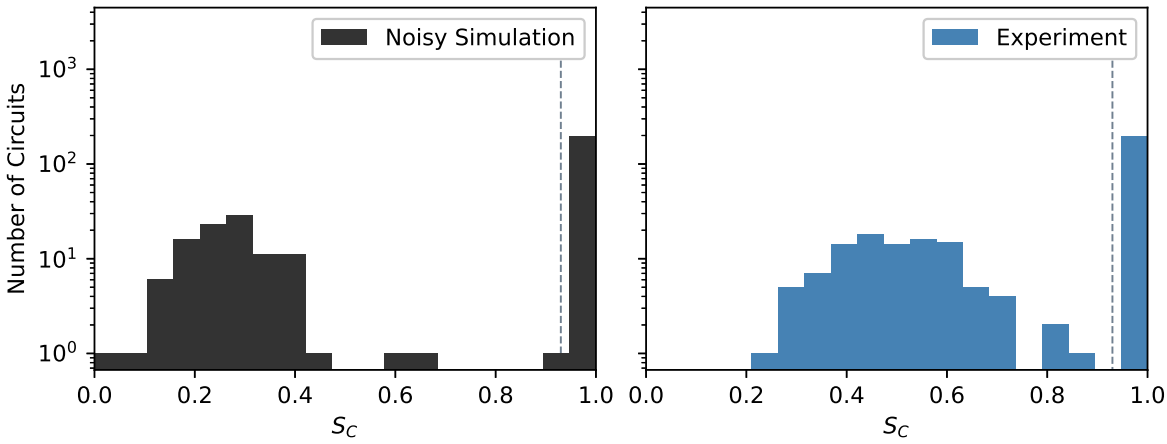


Figure B.6: **Comparison of Noisy Simulations to Experiment** Example results of a noisy simulation for all circuits corresponding to $L = 8$ and $p_x = 1$ (left) compared to the experimental outcomes (right). Bin size is .05. Dashed lines show the threshold of $S_C = 0.93$

simplicity, all the data presented in the main text does not use these error mitigation techniques.

In the ideal implementation of the circuit, certain qubits have a deterministic output in $x$, $y$ or $z$ basis at the end of a circuit. In addition, the qubits that do not participate in the purification dynamics should ideally be in the zero state in the computational ($z$-basis) state. The basis and the respective deterministic outcome can be anticipated with classical simulation. If a qubit is deterministic along $x$ or $y$ basis, we append a single-qubit rotation to align that qubit along the $z$-basis. In the error mitigation stage, we discard the records where the non-participating qubits read a value other than zero or the deterministic qubits, which now should all be purified in the $z$-basis, do not match the simulated expectation. Note, that this method relies on post-selection, so is not directly scalable to the large-$L$ limit. Eventually, active error correction, or similar techniques, would need to be applied to design scalable protocols to probe the ideal circuit evolution in the presence of noise.

To investigate the amount of data discarded by error-mitigation, we consider the quantity $n = \langle \left(\sum_i N_{b,i}\right) / N \rangle_{b \in \{x,y,z\}}$, which measures the proportion of observations retained after error-

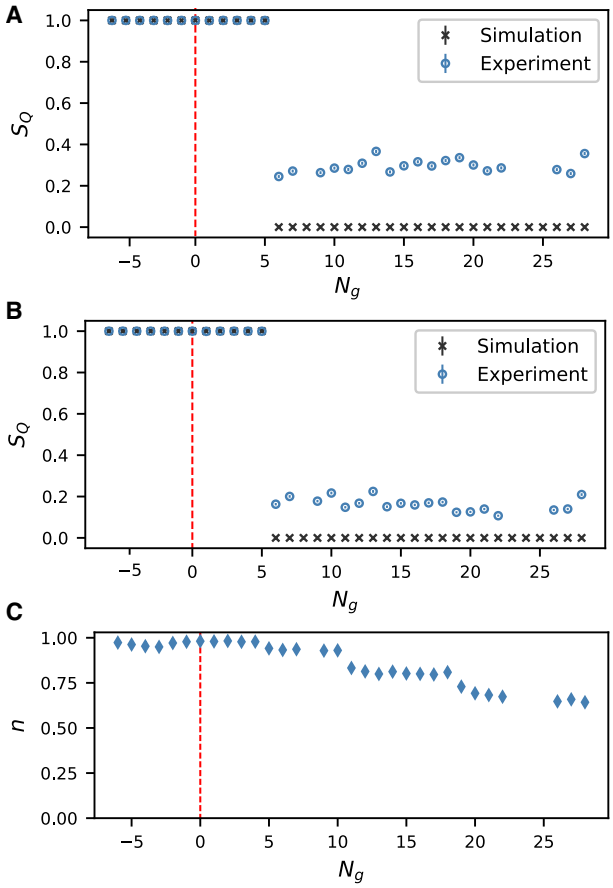


Figure B.7: **Error Mitigation on Purifying Circuit** Time evolution of a sample $L = 6$ circuit, conditioned on a particular choice of outcomes for the intermediate measurements, that purifies without (A) and with (B) error mitigation applied. (C) Average proportion of shots retained, $n$, for each time step

mitigation, aggregated by measurement outcomes and averaged across the three bases. Here $N_{b,i}$ is the number of observations for a tomography circuit used to measure the Pauli expectation along basis $b$, that, conditioned on the measurement record reading $i$, have deterministic qubits matching simulation, and $N$ is the total shots for each circuit used in tomography, which in this instance is 4000. These data were taken in a random order. In (Fig. B.7C), we plot the $n$ for each time-step of (Fig. B.7B). As expected, the proportion of erroneous observations increases with larger circuit depths.

# Chapter C: Supplementary Material: Phase Transition in Magic

## C.1 Basis-Minimized measurement entropy as a measure of magic

Here we show that the basis-minimized conditional entropy is a good measure of non-stabilizerness. Consider a pure state $|\psi\rangle$. Measuring this state in the computational basis produces a classical bitstring $x$ drawn from the Born probability distribution $p(x) = |\langle x|\psi\rangle|^2$. We can instead choose to measure in a stabilizer basis different than the computational basis, by rotating the state using a Clifford unitary. The basis-minimized measurement entropy is the entropy of this probability distribution, minimized over bases:

$$z^*(\psi) = \min_C \left[ -\sum_x |\langle x|C^\dagger|\psi\rangle|^2 \log |\langle x|C^\dagger|\psi\rangle|^2 \right] \tag{C.1}$$

We would like to show that the the basis-minimized conditional entropy is i) zero for stabilizer states, ii) non-increasing under Clifford unitaries and iii) sub-additive.

1. **Faithfulness**: If $|\psi\rangle$ is a pure stabilizer state, there exists some $C^*$ such that $|\psi\rangle = C^*|0\rangle$. We can therefore choose $C = (C^*)^\dagger$ in (C.1) to get $z^* = 0$.

2. **Stability under Clifford Unitaries**: Applying anther Clifford gate $C'$ to some $|\psi\rangle$ should not change $z^*$. Suppose the Shannon entropy of $|\psi\rangle$ is minimized for some $C^*$. Now the

Clifford operation $C'$ takes the state to $|\psi'\rangle = C' |\psi\rangle$. The quantity $z^*$ is now

$$\begin{aligned} z^*(\psi') &= \min_C \left[ -\sum_x |\langle x|\psi'\rangle|^2 \log |\langle x|\psi'\rangle|^2 \right] \\ &= \min_C \left[ -\sum_x |\langle x|C'|\psi\rangle|^2 \log |\langle x|(C')|\psi\rangle|^2 \right] \end{aligned} \tag{C.2}$$

We can recover the original $z^*(\psi)$ by taking $C = C'C^*$. Therefore $z^*$ does not increase under Clifford gates.

3. **Subadditivity**: Given a product state $|\psi\rangle = |\phi\rangle \otimes |\sigma\rangle$, we have

$$\begin{aligned} z^*(|\psi\rangle) &= \min_C \left[ -\sum_x |\langle x|C|\phi,\sigma\rangle|^2 \log |\langle x|C|\phi,\sigma\rangle|^2 \right] \\ &\leq \min_{C_1 \otimes C_2} \left[ -\sum_x |\langle x|C_1 \otimes C_2|\phi,\sigma\rangle|^2 \log |\langle x|C_1 \otimes C_2|\phi,\sigma\rangle|^2 \right] \\ &= \min_{C_1 \otimes C_2} \left[ -\sum_{x_1,x_2} |\langle x_1,x_2|C_1 \otimes C_2|\phi,\sigma\rangle|^2 \log |\langle x_1,x_2|C_1 \otimes C_2|\phi,\sigma\rangle|^2 \right] \\ &= \min_{C_1} \left[ -\sum_{x_1} |\langle x_1|C_1|\phi\rangle|^2 \log |\langle x_1|C_1|\phi\rangle|^2 \right] \\ &\quad + \min_{C_2} \left[ -\sum_{x_2} |\langle x_2|C_2|\sigma\rangle|^2 \log |\langle x_2|C_2|\sigma\rangle|^2 \right] \\ &= z^*(|\phi\rangle) + z^*(|\sigma\rangle) \end{aligned} \tag{C.3}$$

Here, in the second step we confine the minimization to Clifford unitaries of the form $C_1 \otimes C_2$. In the fourth step, we use the independence of the probability distribution across the two halves of the quantum state to decompose the Shannon entropy.

## C.2 Details on Circuit Execution

The circuits were produced by randomly sampling Clifford encoders. Each encoder has depth $d$, where a unit of depth consists of a layer of $N$ single-qubit gates and a layer of $N/2$ disjoint pairs of entangling gates. The single qubit gates are sampled from the set of 24 single-qubit Clifford gates. The entangling gate is chosen to be the fixed-angle Mølmer-Sørensen gate, $MS(\pi/2)$. After selecting the gate sequence for each circuit, the encoder and decoder are optimized separately. After optimization, the circuits are compiled natively to a gateset comprising GPi, GPi2 and MS gates, as described in IonQ Documentation [92]. As a part of execution, the circuits were further augmented with single-qubit gates to minimize noise, using a firmware-level protocol described in [93].

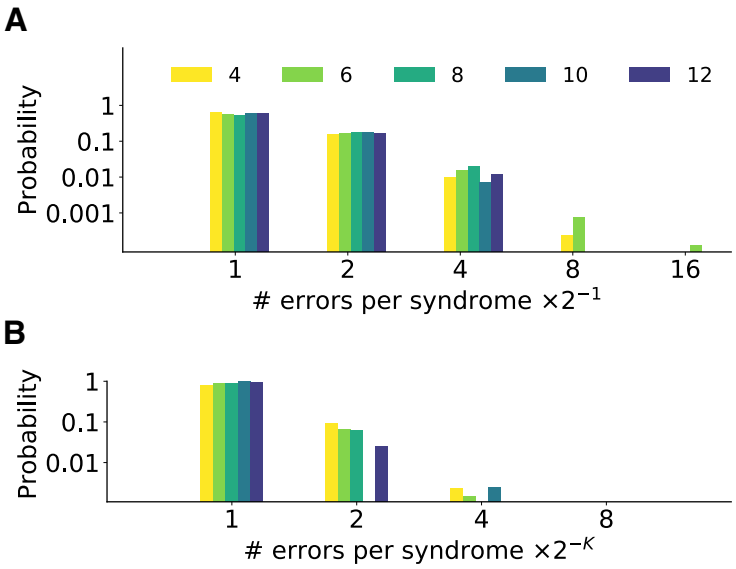


Figure C.1: **Distribution of Errors** The distribution of error per syndrome for vanishing rate codes (**A**) and constant rate codes (**B**). We observe that in both cases, with high probability, the errors are uniformly distributed across syndromes, such that there are $2^K$ unique errors per syndrome. Colorbars give the number of qubits $N$.

## C.3 Analytical Estimate of Magic in the Vanishing Rate Code

In this section we estimate the magic our model at vanishing rate—that is, for a single logical qubit. We first compute the action of the channel on that logical qubit; we find that near the Clifford point, $\alpha = \pi/2$, it is a unitary with probability $1/2$. (Whether or not it is a unitary depends on circuit and syndrome measurement outcome.) We then pass a stabilizer state through the channel and compute the magic of the result. For $\epsilon = \pi/2 - \alpha$ we find that the magic resulting from a single circuit (C) and syndrome measurement outcome is $M_{2;C} = (n\epsilon)^2$, where the integer $n$ is determined by the weights of the errors corresponding to the measurement outcome. Averaging across measurement outcomes this becomes $\mathbb{E}(M_2) = (1/4)N\epsilon^2$ for $N\epsilon^2 \ll 1$, and $\mathbb{E}(M_2) = f(N\epsilon^2)$ in general.

### C.3.1 Action of the Channel on the Logical Space

#### C.3.1.1 The Clifford point

Consider the vanishing-rate (single qubit) code at the Clifford point $\alpha = \pi/2$. Let the Clifford encoder used in the circuit be $C$. The error unitaries can be expanded as

$$U_\alpha = C^\dagger \prod_{j=1}^{N} e^{i\alpha\sigma_z/2} C = \prod_j [\cos\alpha/2 + i \sin\alpha/2 \; \tilde{\sigma}_z^{(j)}] = 2^{-N/2} \sum_{\boldsymbol{a}\in\mathbb{B}^N} i^{n_{\boldsymbol{a}}} \tilde{\sigma}^{\boldsymbol{a}}, \tag{C.4}$$

where $\tilde{\sigma}_z^{(j)} = C^\dagger \sigma_z^{(j)} C$ and $\boldsymbol{a}$ are length-$N$ bitstrings, $\sigma^{\boldsymbol{a}}$ is

$$\tilde{\sigma}^{\boldsymbol{a}} = \prod_{j=1}^{N} \left(\tilde{\sigma}_z^{(j)}\right)^{a_j} \qquad \text{with} \qquad \left(\tilde{\sigma}_z^{(j)}\right)^0 = 1 \tag{C.5}$$

and $n_{\boldsymbol{a}}$ counts the number of error Paulis in $\sigma^{\boldsymbol{a}}$, that is: $n_{\boldsymbol{a}} = \sum_j a_j$.

Below we rewrite $\tilde{\sigma}$ operators as simply $\sigma_z$, noting that these are now highly non-local operations due to conjugation by $C$.

There are $2^N$ such bitstrings, hence $2^N$ such errors (including the trivial "error", the identity operator $\boldsymbol{a} = 0$). When we measure all the $N-1$ syndrome qubits, we see one of $2^{N-1}$ syndromes. (Since vanishing rate codes have 2 errors per syndrome with high probability, we observe in Fig. C.1, we restrict this analysis to to codes in which each syndrome corresponds to exactly 2 errors. In numerics this can be done by postselection. ) Say the measured syndrome is $s$, so projective measurement onto that syndrome is $P_s$. Let us also denote the two errors giving rise to $s$ by $\sigma_z^{\boldsymbol{a}}$ and $\sigma_z^{\boldsymbol{b}}$. If $|\psi\rangle$ is the state after the encoding Clifford unitary, noise layer and the conjgate of the Clifford encoder, the state after the syndrome measurement is then proportional to

$$P_s\left(\sigma^{\boldsymbol{a}} + i^{n_{\boldsymbol{b}}-n_{\boldsymbol{a}}}\sigma^{\boldsymbol{b}}\right)|\psi\rangle\,. \tag{C.6}$$

The errors $\sigma^{\boldsymbol{a},\boldsymbol{b}}$ are Pauli strings. Let $\sigma_1^{\boldsymbol{a},\boldsymbol{b}}$ be the Pauli in each Pauli string that acts on site 1 in the code basis. Then, the effective action of the error channel and syndrome measurement on the logical qubit 1 is

$$K = \sigma_1^{\boldsymbol{a}} + i^m\sigma_1^{\boldsymbol{b}}\,, \quad m = \zeta(\boldsymbol{b}) - \zeta(\boldsymbol{a}) + n_{\boldsymbol{b}} - n_{\boldsymbol{a}}\,, \tag{C.7}$$

where $\zeta(a)$ and $\zeta(b)$ account for the fact that $\sigma_{\boldsymbol{a}}$ and $\sigma_{\boldsymbol{b}}$ can put different phases on the states corresponding to our syndrome $s$.[1] This action $K$ is (proportional to a) unitary if $m$ is odd and

[1]Consider for example $N = 2$ with (non-commuting) errors $\sigma_{\boldsymbol{a}} = xx$ and $\sigma_{\boldsymbol{b}} = xy$. These give the same

$[\sigma^{\boldsymbol{a}}, \sigma^{\boldsymbol{b}}] = 0$, or $m$ is even and $\{\sigma^{\boldsymbol{a}}, \sigma^{\boldsymbol{b}}\} \neq 0$. Otherwise $K$ is a projector. We expect this will happen with probability $1/2$. If we average over syndromes, the result is a channel

$$\mathcal{E}_{k=1}(\rho) = \frac{1}{2} P\rho P + \frac{1}{2} U\rho U^\dagger \tag{C.8}$$

where $P$ is a projector onto some stabilizer state and $U$ is a unitary deducible from the syndrome and the coding circuit $C$.

#### C.3.1.2 Away from the Clifford point

Now move slightly away from the clifford point—take $\alpha \neq \pi/2$. The action on the logical space (C.7) becomes

$$K \propto \left[ {\sigma^{\boldsymbol{a}}}_1 + i^m (\tan \alpha/2)^{n_{\boldsymbol{b}} - n_{\boldsymbol{a}}} {\sigma^{\boldsymbol{b}}}_1 \right] . \tag{C.9}$$

Once again this is unitary for $m$ odd and $[\sigma^{\boldsymbol{a}}, \sigma^{\boldsymbol{b}}] = 0$, or $m$ even and $\{\sigma^{\boldsymbol{a}}, \sigma^{\boldsymbol{b}}\} \neq 0$, and once again these case arises with probability $p \approx \frac{1}{2}$. In the other cases, $K$ is (unitarily equivalent to) a weak projection

$$K = P' \sim \begin{bmatrix} 1 & 0 \\ 0 & \frac{1}{2}\left[1 - (\tan \alpha/2)^{n_{\boldsymbol{b}} - n_{\boldsymbol{a}}}\right] \end{bmatrix} \approx \begin{bmatrix} 1 & 0 \\ 0 & \frac{n_{\boldsymbol{b}} - n_{\boldsymbol{a}}}{2} \epsilon \end{bmatrix} . \tag{C.10}$$

### C.3.2 Magic

To see how far away from the set of stabilizer states the error and measurement take us, let us apply $K$ to an initial stabilizer state $|0\rangle$ on the logical qubit. (We can check $|0\rangle$ without loss of

syndrome with different phases; the $\zeta$ term encodes those phases.

generality, because other initial stabilizer states correspond to different elements of the ensemble of encoding circuits.) If $K$ acts as a weak projector, the result is again a stabilizer state.

But now suppose $K$ acts as a unitary. If $[\sigma^{\boldsymbol{a}}, \sigma^{\boldsymbol{b}}] = 0$ then (up to a Clifford operator)

$$K\,|0\rangle = \frac{1}{\sqrt{2}}(1 + i^m)\,|0\rangle \ : \tag{C.11}$$

(with $m$ odd): $K$ maps $|0\rangle$ to another stabilizer state. If on the other hand $\{\sigma^{\boldsymbol{a}}, \sigma^{\boldsymbol{b}}\} = 0$, then up to a Clifford unitary

$$K\,|0\rangle = \frac{1}{\sqrt{2}}\Big[\,|0\rangle + i^m(\tan\alpha/2)^{n_{\boldsymbol{b}}-n_{\boldsymbol{a}}}\,|1\rangle\,\Big]\ . \tag{C.12}$$

For $\epsilon = \pi/2 - \alpha \ll 1$, taking $m = 0$, this is

$$K\,|0\rangle \approx \frac{1}{\sqrt{2}} e^{i(n_{\boldsymbol{b}}-n_{\boldsymbol{a}})\epsilon\sigma_x}\Big[\,|0\rangle + |1\rangle\,\Big]\ . \tag{C.13}$$

(If $m \neq 0$ then $\sigma^x$ becomes $-\sigma^x$ or $\pm\sigma^y$.) This is an $(n_{\boldsymbol{b}} - n_{\boldsymbol{a}})\epsilon$ rotation away from the stabilizer state $|0\rangle + |1\rangle$. The second Rényi entropy of magic is $M_2 = [n_{\boldsymbol{b}} - n_{\boldsymbol{a}}]^2\epsilon^2$. Fig. 3.2A shows the magic for individual syndromes, together with this prediction. The average over measurement outcomes and circuits is therefore $\langle M_2\rangle = p_{\text{unitary}} \times (1/2)\epsilon^2\,\langle n_{\boldsymbol{b}} - n_{\boldsymbol{a}}\rangle = (1/4)N\epsilon^2$.

For $(n_{\boldsymbol{b}} - n_{\boldsymbol{a}})\epsilon \not\ll 1$ the Taylor series approximation of C.13 still breaks down, but the characteristic scale is still $(n_{\boldsymbol{b}} - n_{\boldsymbol{a}})\epsilon \sim \sqrt{N}\epsilon$ , so one expects a scaling collapse when we plot $M_2$ against $\epsilon\sqrt{N}$. Fig. 3.2B shows this scaling collapse.

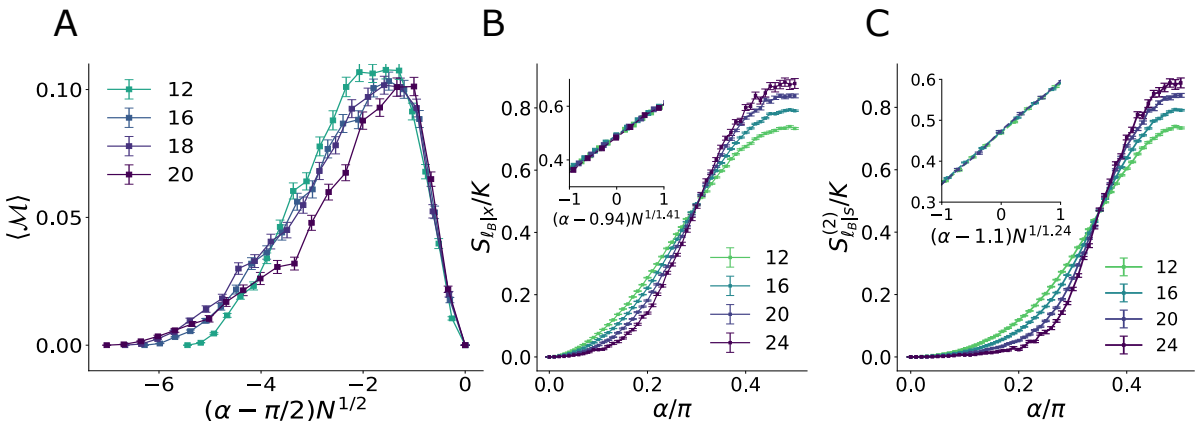


Figure C.2: Numerical Simulations for circuits with depth $d = N/2$. **A**: SSRE for vanishing-rate code. Like with $d = N$ circuits, this exhibits a $\sqrt{N}$ scaling near the critical point at $\alpha = \pi/2$. **B**: Finite size scaling of the conditional entropy and its collapse (inset) computed numerically using simulations at code rate $r = 1/2$. The error bars are omitted in the scaling collapse (inset) which has critical parameters $\alpha_c = 0.943(5)$ and $\nu = 1.41(6)$. These critical parameters are used in the collapse of experimental data in Fig. 3.3E. **C**: Finite size scaling of the Rényi-approximation of the conditional entropy and its collapse (inset) computed numerically using simulations at code rate $r = 1/2$. The error bars are omitted in the scaling collapse (inset) which has critical parameters $\alpha_c = 1.102(3)$ and $\nu = 1.24(4)$. These critical parameters are used in the collapse of experimental data in Fig. 3.3F.

## C.4 Numerics for $d = N/2$ and $d = 2N$

While the numerical data presented in the main text (Fig. 3.1C , Fig. 3.2AB and Fig. 3.3ABCE) used simulations of circuits of depth $d = N$, the experiments were performed with circuits of depth $d = N/2$ to reduce the effects of noise. In Fig. C.2, we present numerics using simulations with circuits of depth $d = N/2$ for quantities we experimentally probe, namely magic in vanishing rate codes and conditional entropies in constant rate codes. The critical exponents so obtained are used for scaling collapse for the experimental data presented in the maintext.

Note that the critical exponents of conditional entropies in Fig. C.2(B,C) are different than the critical exponents for circuits with $d = N$. We expect the critical exponents to converge for sufficiently deep encoding circuits – that is once the circuits start forming good error correcting

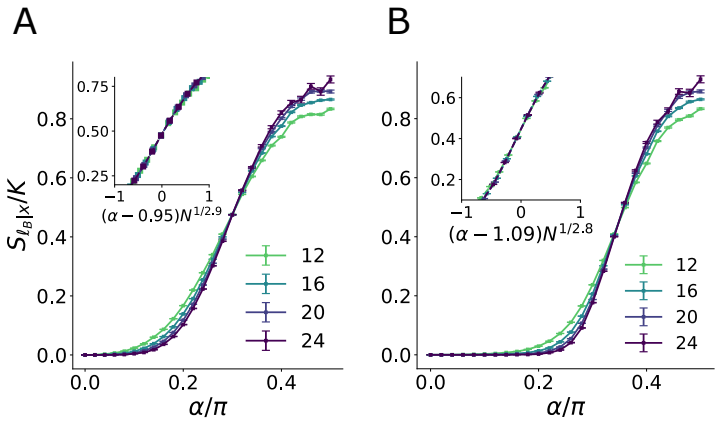


Figure C.3: Numerical Simulations for circuits with depth $d = 2N$. **A**: Finite size scaling of the conditional entropy and its collapse (inset) computed numerically using simulations at code rate $r = 1/2$. The scaling collapse (inset) has critical parameters $\alpha_c = 0.94(1)$ and $\nu = 2.9(4)$. **B**: Finite size scaling of the Rényi-approximation of the conditional entropy and its collapse (inset) computed numerically using simulations at code rate $r = 1/2$. The scaling collapse (inset) has critical parameters $\alpha_c = 1.093(1)$ and $\nu = 2.8(4)$.

codes. In Fig. C.3, we present numerics on $d = 2N$ circuits, which results in critical exponents close to $d = N$ circuits. This suggests that the $d = N$ circuits can adequately capture ensemble-average properties.

## C.5 Finite Size Scaling

To obtain the critical parameters of the scaling collapse, we assume that the quality of interest $f(\alpha, N)$ is a function of error rate $\alpha$ and the code size $N$ and can be expanded as

$$f(\alpha, N) \approx A + Bx + Cx^2 \qquad x = (\alpha - \alpha_c)N^{1/\nu} \tag{C.14}$$

Using data collected using numerical simulations $y_{\alpha,N}$, we minimize the following mean squared error to obtain the estimate for the critical parameters $\alpha_c$ and $\nu$:

$$\hat{\alpha}_c, \hat{\nu} = \text{argmin}_{\alpha_c,\nu} \min_{A,B,C} \sum_{y_{\alpha,N}} (A + Bx + Cx^2 - y_{\alpha,N})^2 \qquad \text{with } x = (\alpha - \alpha_c)N^{1/\nu} \tag{C.15}$$

To obtain the error in the estimate of critical parameters, we introduce a new estimate $\hat{\alpha}_c^{\overline{y_{\alpha,N}}}$ obtained by removing the datapoint $y_{\alpha,N}$ from the dataset (whose size we denote by $D$). Denoting the number of datapoints by $D$, the variance in the estimate is taken to be

$$\text{Var}(\alpha_c) = \frac{D-1}{D} \sum_{y_{\alpha,N}} \left(\overline{\alpha_c} - \hat{\alpha}_c^{\overline{y_{\alpha,N}}}\right)^2 \qquad \text{where} \quad \overline{\alpha_c} = \frac{1}{D} \sum_{y_{\alpha,N}} \hat{\alpha}_c^{\overline{y_{\alpha,N}}}, \tag{C.16}$$

The error in $\nu$ is obtained similarly.

## C.6 Bootstrap Estimate of Error

The bootstrap resampling technique is commonly used to estimate errorbars and confidence intervals when straightforward error propagation is difficult. We use this procedure to estimate the errorbars for experimental data. Given an sample of size $N$, we generate 1000 new samples of size 20. This is done by uniformly picking elements from the original sample with replacement. We take the standard deviation of the means of the new samples to be the boostrap error.

## C.7 Basis-minimized Measurement Entropy and Decoder Breakdown

The basis-minimized measurement entropy is a direct probe of the breakdown of the optimal Clifford decoder. To see why, imagine storing a classical bit string as a computational basis

state, encoding it using the Clifford circuit of our model, subjecting it to error, performing the conjugate of the the encoding circuit and error measurements, and attempting to recover it by measuring the logical state in the computational basis. Without error, there will be exactly one possible syndrome and one possible logical measurement outcome. With error, there may be many: approximately $Z_{\boldsymbol{s},\text{comp.}} = \exp S[p_{\boldsymbol{s},\text{comp}}]$ possible bitstrings correspond to syndrome $\boldsymbol{s}$, where $p_{\boldsymbol{s},\text{comp}}$ is the Born probability distribution of outcomes of measuring the logical state corresponding to syndrome $\boldsymbol{s}$ in the computational basis, and $S$ is the entropy. If $Z_{\boldsymbol{s},\text{comp}}$ is not small, measuring in the computational basis may produce any of number of outcomes—not just the initial stored bitstring.

If the noise is coherent, the net effect of the channel is to apply a unitary or weak projection to the logical state. In this case measuring in a different basis may recover the information; the basis change is known as a decoder. The best Clifford decoder gives $Z_{\boldsymbol{s}} = \min_B \exp S[p_{\boldsymbol{s},B}]$ possible logical measurement outcomes, where now $p_{\boldsymbol{s},B}$ is the Born probability distribution of outcomes of measuring the logical state corresponding to syndrome $\boldsymbol{s}$ in the basis given by Clifford circuit $B$. Across syndromes, the typical number of possible logical measurements is given by the average over syndromes

$$Z_{l,\text{typical}} = \exp \left\langle \ln Z_{l;\boldsymbol{s}} \right\rangle_{\boldsymbol{s}} = \exp \left\langle \min_B S[p_{\boldsymbol{s},B}] \right\rangle_{\boldsymbol{s}} \tag{C.17}$$

When this quantity is materially greater than 1, i.e.

$$\varepsilon < \left\langle \min_B S[p_{\boldsymbol{s},B}] \right\rangle_{\boldsymbol{s}} \tag{C.18}$$

for some small $\varepsilon$, the code has broken down and cannot even store classical information: it has probability $\sim e^{\varepsilon}$ of irrecoverably muddling the input bitstring.

Storing classical information in this way is a weaker condition than storing quantum information. Moreover, while a large measurement entropy indicates that classical information is irrecoverable, small measurement entropy does not indicate that classical information is recoverable, because syndrome measurement may project the logical state to a pure stabilizer state different from the initial state.

The condition (C.18) implicitly allows the choice of measurement basis for the logical space to vary with syndrome. An intelligent decoder will use the syndrome to pick an optimal basis. A more primitive decoder will pick a fixed basis, and use that for all syndromes. Such a decoder will fail if $\varepsilon < \min_B \langle S[p_{\boldsymbol{s},B}]\rangle_{\boldsymbol{s}}$. The simplest decoder of all leaves the logical state in the computational basis; it fails if $\varepsilon < \langle S[p_{\boldsymbol{s},B}]\rangle_{\boldsymbol{s}}$. This is the quantity we treat in the main text.

## C.8 Analytics on Rényi-approximation to Conditional Entropy

In this section, we use Schur-Weyl duality to analytically approximate the Rényi analogue of the conditional entropy, $S^{(2)}_{\ell|s} = S^{(2)}_{\ell,s} - S^{(2)}_{s}$, with $S^{(2)}_{X} = -\log \sum_{x\in X} p_x^2$ being the Rényi entropy. As a reminder, $\ell$ is the distribution of measurements of the $K$ logical qubits, and $s$ is the distribution of measurements of the $N-K$ syndrome qubits, both in the computational basis. We would like to compute the Rényi, analogue of the conditional entropy, averaged over Clifford encoders.

The circuit-averaged measure we are interested in is therefore,

$$\mathbb{E}_C S^{(2)}_{\ell|s} = \mathbb{E}_C S^{(2)}_{\ell,s} - \mathbb{E}_C S^{(2)}_{s} = -(\mathbb{E}_C \log M_N - \mathbb{E}_C \log M_{N-K}) \qquad \text{with } M_k = \sum_{x\in\{0,1\}^k} p_x^2 \tag{C.19}$$

where we have introduced the notation $M_k$ to denote the collision probability over the distribution of measurements of $k$ qubits.

Crucially, if the circuit-to-circuit variability of the collision probability is negligible, we can take the expectation over Clifford circuits inside the logarithm. We observe that such a typicality assumption is indeed valid for sufficiently large system, but breaks down for small $N$ and large error-rate $\alpha \to \pi/2$. Here, we proceed with the typicality assumption to get

$$\mathbb{E}_C S^{(2)}_{\ell|s} \approx -(\log \mathbb{E}_C M_N - \log \mathbb{E}_C M_{N-K}) \tag{C.20}$$

Consider the circuit-averaged collision probability in our model model where we begin with qubits in a $|0\rangle^{\otimes N}$ state, followed by a Clifford unitary $C$, followed by a noise operation $N(\alpha) = \prod_{i=1}^{N} \exp(i\sigma_z \alpha/2)$, followed by $C^\dagger$. We finally measure all $N-K$ qubits at the end.

distribution induced by measurements of $N-K$ qubits out of a $N$ qubit system $|\psi\rangle$:

$$\begin{aligned}
\mathbb{E}_C M_{N-K} &= \sum_{x\in\{0,1\}^{N-K}} p_x^2 \\
&= \sum_{x\in\{0,1\}^{N-K}} \operatorname{tr}\left(I_{2^K}\otimes|x\rangle\langle x|\,|\psi\rangle\langle\psi|\right)^2 \\
&= \sum_{x\in\{0,1\}^{N-K}} \mathbb{E}_C \operatorname{tr}\left((I_{2^K}\otimes|x\rangle\langle x|)C^\dagger N(\alpha)C\,|0\rangle\langle 0|\,C^\dagger N(\alpha)^\dagger C\right)^2 \\
&= \sum_{x\in\{0,1\}^{N-K}} \mathbb{E}_C \operatorname{tr}\Big((I_{2^K}\otimes|x\rangle\langle x|)\otimes(I_{2^K}\otimes|x\rangle\langle x|)\Big)\left(C^\dagger\right)^{\otimes 2} \\
&\qquad N(\alpha)^{\otimes 2}C^{\otimes 2}\,|0,0\rangle\langle 0,0|\left(C^\dagger\right)^{\otimes 2}\left(N(\alpha)^\dagger\right)^{\otimes 2}C^{\otimes 2}\Big),
\end{aligned}$$

where we define $I_{2^K}$ to be the identity operator on $K$ logical qubits. Substituting the basis-decomposed representation of $I_{2^k}=\sum_{i\in\{0,1\}^K}|i\rangle\langle i|$ above, we get

$$\begin{aligned}
&\mathbb{E}_C M_{N-K} \\
&= \sum_{\substack{x\in\{0,1\}^{N-K}\\ i,j\in\{0,1\}^K}} \mathbb{E}_C \operatorname{tr}\left((|i,x\rangle\langle i,x|)\otimes(|j,x\rangle\langle j,x|)\right) \\
&\qquad \left(C^\dagger\right)^{\otimes 2} N(\alpha)^{\otimes 2}C^{\otimes 2}\,|0^N,0^N\rangle\langle 0^N,0^N|\left(C^\dagger\right)^{\otimes 2}\left(N(\alpha)^\dagger\right)^{\otimes 2}C^{\otimes 2}\Big) \\
&= \sum_{\substack{x\in\{0,1\}^{N-K}\\ i,j\in\{0,1\}^K}} \mathbb{E}_C \Big[\langle(i,x),(j,x)|\left(C^\dagger\right)^{\otimes 2}\mathcal{N}(\alpha)^{\otimes 2}C^{\otimes 2}\,|0^n,0^n\rangle \\
&\qquad \langle 0^N,0^N|\left(C^\dagger\right)^{\otimes 2}\left(\mathcal{N}(\alpha)^\dagger\right)^{\otimes 2}C^{\otimes 2}\,|(i,x),(j,x)\rangle\Big] \\
&= \sum_{\substack{x\in\{0,1\}^{N-K}\\ i,j\in\{0,1\}^K}} \mathbb{E}_C \langle(i,x),(j,x),0^n,0^n|\left(C^\dagger\right)^{\otimes 4}\left(\mathcal{N}(\alpha)^{\otimes 2}\otimes(\mathcal{N}(\alpha)^\dagger)^{\otimes 2}\right)C^{\otimes 4}|0^n,0^n,(i,x),(j,x)\rangle \\
&= \sum_{\substack{x\in\{0,1\}^{N-K}\\ i,j\in\{0,1\}^K}} \langle(i,x),(j,x),0^N,0^N|\mathbb{E}_C\left[\left(C^\dagger\right)^{\otimes 4}\left(\mathcal{N}(\alpha)^{\otimes 2}\otimes(\mathcal{N}(\alpha)^\dagger)^{\otimes 2}\right)C^{\otimes 4}\right]|0^N,0^N,(i,x),(j,x)\rangle
\end{aligned}$$

In the second line, we have used the relation $\mathrm{tr}(|x\rangle\langle x|A|0\rangle\langle 0|B) = \langle x|A|0\rangle\langle 0|B|x\rangle$. In the third line, we combine the two inner products $\langle x|A|0\rangle\langle 0|B|x\rangle = \langle x,0|(A\otimes B)|0,x\rangle$. In the fourth line, we have moved the expectation inside the inner-product.

The Schur-Weyl duality gives a decomposition of a Clifford-averaged operator as a linear sum of representation of a semigroup $\Sigma_4$ which consists of 30 elements.

$$\mathbb{E}_C\left[\left(C^\dagger\right)^{\otimes 4}\left(N(\alpha)^{\otimes 2}\otimes(N(\alpha)^\dagger)^{\otimes 2}\right)C^{\otimes 4}\right] = \sum_{T\in\Sigma_4} a_T R(T) \tag{C.21}$$

$R(T)$ is the representation for $T\in\Sigma_4$ operator which acts on four copies of the $N$-qubit state. Knowing all the representations $R(T)$, it is possible to calculate the coefficients $a_T$ for each error-rate $\alpha$. Substituting the decomposition into our expression for $\mathbb{E}_C M$, we get,

$$\mathbb{E}_C M_{N-K} = \sum_{\substack{x\in\{0,1\}^{N-K}\\ i,j\in\{0,1\}^K}}\sum_{T\in\Sigma_4} a_T\langle(i,x),(j,x),0^n,0^n|R(T)|0^n,0^n,(i,x),(j,x)\rangle \tag{C.22}$$

Note that $R(T)$ is a qubit-wise representation, that is $R(T) = r(T)^n$ for some $r(T)$ acting on four copies of a single-qubit state. We can then re-write the expression above, distributing the representation to the "syndrome" register and the "logical qubit" register.

$$\mathbb{E}_C M_{N-K} = \sum_{\substack{x\in\{0,1\}^{N-K}\\ i,j\in\{0,1\}^K}}\sum_{T\in\Sigma_4} a_T\langle i,j,0^k,0^k|r(T)^k|0^k,0^k,i,j\rangle\langle x,x,0^n,0^n|r(T)^{n-k}|0^n,0^n,x,x\rangle \tag{C.23}$$

We would like to evaluate this expression. First, consider the case where $x=0$. The second inner-product resolves to 1 for all $T$ when $x=0$. The first inner product also resolves to 1 for all $T$ if $i=j=0$. If $i=0$ but $j\neq 0$, a certain subset of $\Sigma_4$ resolve to one (the rest evaluate

to zero). Let's call this set $S_{0,x}$). Similarly, if $j = 0$ and $i \neq 0$, denote the subset that resolves to 1 by $S_{x,0}$). Similarly, let the set $S_{x,x}$ denote elements that evaluate to 1 whenever $i = j \neq 0$. Finally, let $S_{x,y}$ be the set of elements that resolves $\langle i, j, 0, 0 | r(T)^K | 0, 0, i, j \rangle$ to one whenenver $i \neq 0, j \neq 0, i \neq j$. The total contribution of the $x = 0$ term is given by

$$\sum_{T\in\Sigma_4} a_T \quad \underset{i=0,j=0}{} + \underbrace{\sum_{i\in\{0,1\}^K} \sum_{T\in S_{x,0}} a_T}_{i\neq 0, j=0} + \underbrace{\sum_{\substack{j\in\{0,1\}^K \\ j\neq 0}} \sum_{T\in S_{0,x}} a_T}_{i=0, j\neq 0} + \underbrace{\sum_{\substack{j\in\{0,1\}^K \\ j\neq 0}} \sum_{T\in S_{x,x}} a_T}_{i=j\neq 0} + \sum_{\substack{i,j\in\{0,1\}^K \\ i\neq j \\ i\neq 0, j\neq 0}} \sum_{T\in S_{x,x}} a_T$$

$$= \sum_{T\in\Sigma_4} a_T + (2^K - 1) \sum_{T\in S_{x,0}} a_T + (2^K - 1) \sum_{T\in S_{0,K}} a_T$$

$$+ (2^K - 1) \sum_{T\in S_{x,x}} a_T + (2^K - 1)(2^K - 2) \sum_{T\in S_{x,y}} a_T \tag{C.24}$$

Second, whenever $x \neq 0$, the second inner product resolves to 1 only for the set $S_{x,x}$, otherwise it evaluates to 0. The condition that $T \in S_{x,x}$ also necessitates that $i = j$ in the first inner product. The set $\{x \neq 0\}$ has size $2^{N-K} - 1$. Therefore, the total contribution from the $x \neq 0$ terms is simply

$$(2^{N-K} - 1) \left( 2^K \sum_{T\in S_{x,x}} a_T + 2^K (2^K - 1) \sum_{T\in S_{x,y}} a_T \right) \tag{C.25}$$

Adding (C.24) and (C.25), we get the expected $M_K$.

Finally, we approximate the the circuit-averaged Renyi-analogue of the conditional entropy using (C.20).

# Chapter D: Supplementary Material: Error Mitigation Threshold in Random Circuits

## D.1 Mean-Field Theory in Brownian Circuits

Here, we develop a mean-field theory for the error mitigation threshold in the noisy-mitigated Brownian circuit model.

The unitary dynamics in the Brownian quantum circuit model is described by a stochastic Hamiltonian

$$H(t) = \sum_{i<j,\mu,\nu} J_{ij\mu\nu}(t)\sigma_i^\mu \sigma_j^\nu, \tag{D.1}$$

where $\sigma_i^\mu$ are Pauli operators $\mu \in \{X, Y, Z\}$ for site $i$ of $N$ qubits and $J_{ij\mu\nu}(t)$ is a white-noise correlated coupling with variance [128, 129]

$$\langle J_{ij\mu\nu}(t) J_{k\ell\gamma\delta}(t')\rangle = \frac{J}{2N}\delta_{ik}\delta_{j\ell}\delta_{\mu\gamma}\delta_{\nu\delta}\delta(t-t'). \tag{D.2}$$

The noise and antinoise are treated using a Lindblad master equation

$$\dot{\rho} = -i[H(t), \rho] + \sum_i \frac{\gamma_i - \gamma_a}{4}\Big(-3\rho + \sum_\mu \sigma_i^\mu \rho \sigma_i^\mu\Big), \tag{D.3}$$

where $\gamma_i$ is the local random noise rate and $\gamma_a$ is the antinoise rate.

To analyze the dynamics we derive an effective master equation that describes the replicated system

$$M_k(\rho) = \mathbb{E}[U^{\otimes k} \rho U^{\dagger \otimes k}], \tag{D.4}$$

where $U = \mathcal{T} e^{-i \int_0^t dt' H(t')}$ is the time evolution operator under the Hamiltonian. Expanding to second order in an infinitesimal time-step, we arrive at the equation $M_k(\rho) = e^{\mathcal{L}_k t}$ for a Lindbladian $\mathcal{L}_k$ given by

$$\mathcal{L}_k(\rho) = \frac{J}{2N} \sum_{i \neq j, \mu, \nu, r, s} \sigma_{ir}^{\mu} \sigma_{jr}^{\nu} \rho \sigma_{is}^{\mu} \sigma_{js}^{\nu} - \frac{1}{2} \{ \sigma_{ir}^{\mu} \sigma_{is}^{\mu} \sigma_{jr}^{\nu} \sigma_{js}^{\nu}, \rho \}, \tag{D.5}$$

where $r$ and $s$ are replica indices that run over $1, \ldots, k$. Thus, we arrive at a master equation describing the average dynamics of the replicated density matrices

$$\dot{\rho} = \mathcal{L}_k(\rho) + \sum_i \frac{\gamma_i - \gamma_a}{4} \Big( -3k\rho + \sum_{r,\mu} \sigma_{ir}^{\mu} \rho \sigma_{ir}^{\mu} \Big). \tag{D.6}$$

To develop the mean field theory, we study the two-replica problem $k = 2$. Similar to a Haar random circuit, the Lindbladian $\mathcal{L}_2$ has two steady states $I^{\otimes N}$ and $S^{\otimes N}$. As our mean-field ansatz, we therefore use a product state of the form $\rho = \bigotimes_{i=1}^{N} \rho_i$. A further simplification arises from the nature of the dynamics that has an effective SU(2) symmetry in the average-replica dynamics. As a result, we can express

$$\rho_i = (1/4 + \delta_i) |s\rangle\langle s| + (1/4 - \delta_i/3) P_T, \tag{D.7}$$

where $\delta_i$ is the deviation from an infinite temperature state, $|s\rangle$ is a two-qubit singlet state across

the two replicas, and $P_T$ is the projector onto the two-qubit triplet subspace of the two replicas.

The mean-field equations for $\delta_i$ take the form

$$\dot{\delta}_i = -4\Big[\Delta_i + \frac{J}{N}\sum_{j\neq i}(3+4\delta_j)\Big]\delta_i, \tag{D.8}$$

where $\Delta_i = \gamma_i - \gamma_a$. This equation has the two steady-state solutions $\delta_i = 0$ and $\delta_i = -3/4$, corresponding to the $I^{\otimes N}$ and $S^{\otimes N}$ solutions, respectively. In the case of binary disorder, we define two populations of sites $A_{1/2}$ such that $\Delta_i = \gamma_{1/2} - \gamma_a$, respectively, for $i \in A_{1/2}$. We have the zero-mean field condition $p\Delta_1 + (1-p)\Delta_2 = 0$. Defining $G_\pm = \frac{1}{N}\Big(\sum_{i\in A_2}\delta_i \pm \sum_{i\in A_1}\delta_i\Big)$, we arrive at simple closed set of equations in the large-$N$ limit

$$\dot{G}_+ = -4J(3+4G_+)G_+ + \frac{4|\Delta_1|}{2(1-p)}[G_- - (2p-1)G_+],$$
$$\dot{G}_- = -4J(3+4G_+)G_- + \frac{4|\Delta_1|}{2(1-p)}[G_+ - (2p-1)G_-].$$

Setting $p = 1/2$, these equations reduce to the particularly simple form

$$\dot{G}_+ = -4J(3+4G_+)G_+ + 4|\Delta_1|G_-, \tag{D.9}$$

$$\dot{G}_- = -4J(3+4G_+)G_- + 4|\Delta_1|G_+, \tag{D.10}$$

For general $p$, the steady state solutions are $G_+ = 0, -(3-|\Delta_1|/J)/4, -(3+\Delta_2/J)/4$. The all identity solution $G_+ = G_- = 0$ only becomes an unstable fixed point for $|\Delta_1|/J \geq 3$, whereas it remains stable for weaker disorder. As a result, the phase transition in the mean-field theory occurs at the disorder strength $|\Delta_1| = 3J$. Beyond this value of disorder, the mean-field steady-

state solution flows to an unphysical state; however, for weaker disorder, the physical mean-field solution remains stable.

## D.2 Statistical Mechanics Mapping Formalism

Here, we review the statistical mechanics for the model with noise and antinoise, generalizing the mappings studied in Ref. [51,125,130–132]. In this paper, we focus our attention to calculating second-moment quantities of a quantum state, which includes measures like fidelity, collision probability, and linear cross entropy. The circuit-averaged calculations of such quantities lends itself to a statistical mechanical mapping to an Ising spin model.

Consider a second moment measure $M$, averaged over circuits from ensemble $\mathcal{U}$. For a state a state $\rho_C$ of dimension $2^{2n} \times 2^{2n}$, generated using a circuit $C$ from an ensemble $\mathcal{U}$, a circuit-averaged second moment measure $M$ for can be written as a two-copy expectation of a linear operator $O_M$ of dimension $2^{4n} \times 2^{4n}$.

$$\mathbb{E}_{C\in\mathcal{U}}[M[\rho_C]] = \mathbb{E}_{C\in\mathcal{U}}\left[\mathrm{tr}\left(O_M \rho_C \otimes \rho_C\right)\right] = \mathrm{tr}\left(O_M \mathbb{E}_{C\in\mathcal{U}}\left[\rho_C \otimes \rho_C\right]\right) \tag{D.11}$$

The circuit-averaged two-copy state $\mathbb{E}_{C\in\mathcal{U}}[\rho_C \otimes \rho_C]$, therefore, enables us to calculated second-moment measures.

We consider circuit models that can be decomposed into a series of elementary two-qubit gates (noisy or noiseless), each drawn independently from the two-qubit Haar ensemble $\mathcal{U}_2$. The action of the circuit map on two-copies of an initial input state is, thus, given by

$$\rho_C^{\otimes 2} = C_s \circ C_{s-1} \circ \cdots \circ C_1[\rho_0 \otimes \rho_0], \tag{D.12}$$

where the elementary single-qubit or two-qubit channels are indexed using integers $[1, s]$. For noiseless gates, $C_i[\rho_0 \otimes \rho_0] = (C_i \otimes C_i)\rho(C_i^\dagger \otimes C_i^\dagger)$. We can model a noisy circuit by adding error channel $\mathcal{E}$ after each noiseless gate:

$$\rho_C^{\otimes 2} = \mathcal{E}_s \circ C_{s-1} \circ \mathcal{E}_{s-1} C_{s-1} \circ \cdots \circ \mathcal{E}_1 \circ C_1[\rho_0 \otimes \rho_0]. \tag{D.13}$$

In general, the error channel may act on any set of qubits. For our purposes, we assume that the error channel $\mathcal{E}_i$ acts on the qubit or the pair of qubits acted on by the noiseless gate $C_i$. Since we draw each gate from the random one-qubit or two-qubit Haar ensemble, we can replace the noiseless maps $C_i[\rho]$ with the gate-averaged map $\overline{C}_i[\sigma] = \mathbb{E}_{C \in \mathcal{U}_{1/2}} C[\sigma]$,

$$\mathbb{E}_{C \in \mathcal{U}}[\rho_C \otimes \rho_C] = \mathcal{E}_s \circ \overline{C}_{s-1} \circ \mathcal{E}_{s-1} \overline{C}_{s-1} \circ \cdots \circ \mathcal{E}_1 \circ \overline{C}_1[\rho_0 \otimes \rho_0]. \tag{D.14}$$

The action of a random single-qubit gate $C$, on a state residing in the two-copy Hilbert space is given by

$$\overline{C}^{(1)}[\sigma] = \frac{\mathrm{tr}((1 - S/2)\sigma)}{3} I + \frac{\mathrm{tr}((S - 1/2)\sigma)}{3} S, \tag{D.15}$$

where $I$ and $S$ are the $4 \times 4$ identity matrix and SWAP matrices, respectively. Similarly, the action of a random two-qubit gate on two copies of a qubit-pair is given by

$$\overline{C}^{(2)}[\sigma] = \frac{\mathrm{tr}((1 - SS/4)\sigma)}{15} II + \frac{\mathrm{tr}((SS - 1/4)\sigma)}{15} SS, \tag{D.16}$$

where we use the shorthand $SS = S \otimes S$ and $II = I \otimes I$. If two copies of a quantum state can be represented by a string of $\rho^{\otimes 2} \in \{I, S\}^n$, a single-qubit gate acts on qubit $k$ by modifying the

$j$th bit of the $I - S$ string using the transition rules

$$I \to I \qquad S \to S, \tag{D.17}$$

while leaving the rest of the bits in the string unchanged. Similarly, a two-qubit gate acting on qubits $j$ and $k$ modifies the $j$th and $k$th bits according to the transition rules:

$$II \to II \qquad IS, SI \to \frac{2}{5}(II + SS) \qquad SS. \to SS. \tag{D.18}$$

A noiseless random circuit, therefore, can be represented as a linear operator acting on the reduced space spanned by basis elements in $\{I, S\}^n$, with each noiseless single-qubit gate given an identity map, and a two-qubit gate given by the transition matrix

$$T[\overline{C}^{(2)}] = \begin{pmatrix} 1 & 2/5 & 2/5 & 0 \\ 0 & 0 & 0 & 0 \\ 0 & 0 & 0 & 0 \\ 0 & 2/5 & 2/5 & 1 \end{pmatrix}. \tag{D.19}$$

We can similarly, find the transition matrices corresponding to the noise and antinoise channel. The single-qubit depolarization channel with error rate $q$, given by the following map

$$\mathcal{E}^{(1)}(\rho) = (1 - q)\rho + q \operatorname{tr}(\rho)\frac{\mathbb{1}}{2}, \tag{D.20}$$

acts on two copies of a qubit such that

$$\mathcal{E}[I] = \mathcal{E}[I_2 \otimes I_2] = \mathcal{E}^{(1)}[I_2] \otimes \mathcal{E}^{(1)}[I_2] = I_2 \otimes I_2 = I, \tag{D.21}$$

where $I_2$ is a $2 \times 2$ identity matrix. Similarly,

$$\begin{aligned}
&\mathcal{E}[S] \\
&= (\mathcal{E}^{(1)} \otimes \mathcal{E})[I_2 \otimes I_2 + X \otimes X + Y \otimes Y + Z \otimes Z]/2 \\
&= \left[I_2 \otimes I_2 + (1-q)^2 \left(X \otimes X + Y \otimes Y + Z \otimes Z\right)\right]/2 \\
&= \left[(1-(1-q)^2)/2 I + (1-q)^2 S\right]
\end{aligned}$$

where we have used the fact that $S = (I_2 \otimes I_2 + X \otimes X + Y \otimes Y + Z \otimes Z)/2$. The transition matrix corresponding to a depolarizing noise, in the statistical mechanical picture is given by,

$$T[\mathcal{E}_q] = \begin{pmatrix} 1 & (1-(1-q)^2)/2 \\ 0 & (1-q)^2 \end{pmatrix} \tag{D.22}$$

Likewise, the antinoise channel of strength $q_a$, given by

$$\mathcal{A}^{(1)}(\rho) = \frac{1}{1-q_a}\left(\rho - q_a \operatorname{tr}(\rho)\frac{\not{1}}{2}\right), \tag{D.23}$$

acts on two-copies of a qubit such that

$$\mathcal{A}[I] = (\mathcal{A}^{(1)} \otimes \mathcal{A}^{(1)})[I_2 \otimes I_2] = I, \text{ and} \tag{D.24}$$

$$\mathcal{A}[S] = \left[\left(1 - \frac{1}{(1-q_a)^2}\right)\frac{I}{2} + \frac{1}{(1-q_a)^2}S\right], \tag{D.25}$$

giving a transition matrix

$$T[\mathcal{A}_{q_a}] = \begin{pmatrix} 1 & (1-(1-q_a)^{-2})/2 \\ 0 & (1-q_a)^{-2}. \end{pmatrix} \tag{D.26}$$

Concatenating the transition matrix for the noise channel and the antinoise channel gives the transition matrix for the composite channel. $T[\mathcal{A}_{q_a} \circ \mathcal{E}_q] = T[\mathcal{A}_{q_a}].T[\mathcal{E}_q]$.

In our simulations, we start with an initial state drawn from the Haar ensemble or a random product state. A Haar random state is proportional to $I^{\otimes n}+S^{\otimes n}$ in the two-copy descrpition, while a random product state is proportional to $(I+S)^{\otimes n}$. We can then use the statistical mechanical formalism discussed above to evolve this state using the respective transition matrices for two-qubit gates, noise and antinoise channels.

## D.3 Local Probe

In Fig. 4.2, we presented different correlation metrics between two qubits in the system as a probe of the phase transition. Here, we present an alternative metric based on the entropy of a single qubit in the system.

Deep in the below threshold phase, this single-qubit entropy quantity saturates to one bit,

while above threshold it diverges to large negative values due to the unphysical density matrix. As a result, we expect a crossing to occur at the phase transition. Numerical simulations of the two-replica stat-mech model for the all-to-all circuit model illustrate this behavior. In Fig. D.1(a), we show the unscaled behavior of the entropy for different system sizes, which shows a crossing near $\sigma_c/\bar{q} = 0.65(5)$. Collapsing the data with this value of $\sigma_c$ fixed, we estimate a critical exponent $\mu = 1.0(2)$. In Fig. 4.2(c-d), we fixed $\mu = 1$ in collapsing the mutual information data based on these scaling results. This single-qubit quantity also has advantages for experimental probes of the transition as it requires minimal tomographic overhead to estimate.

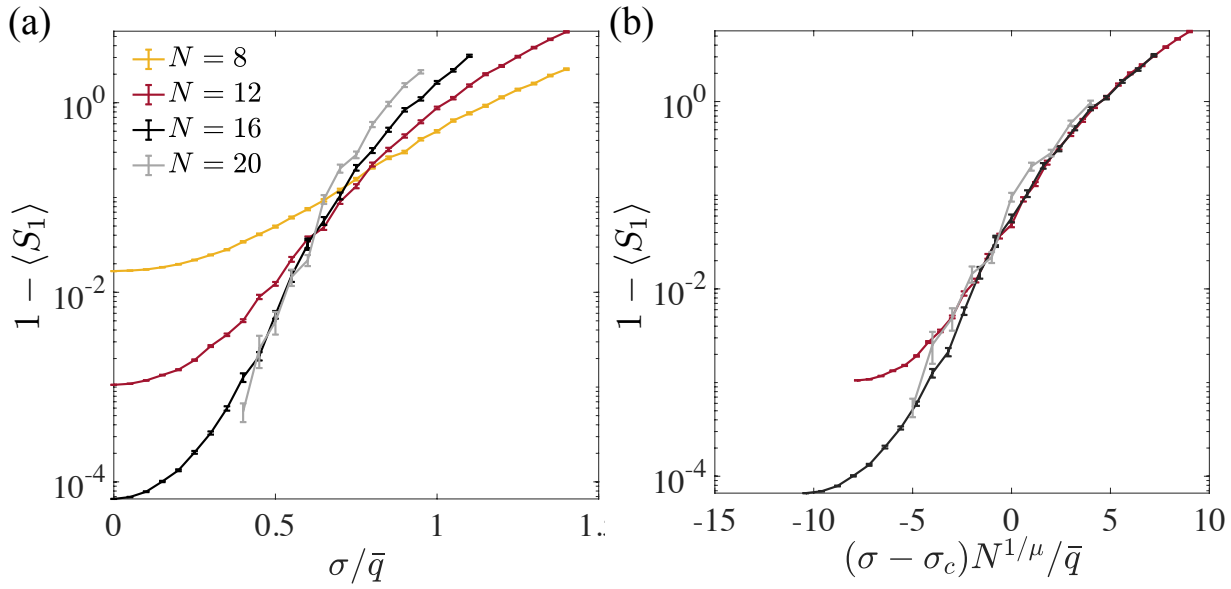


Figure D.1: Local probe of the error mitigation threshold: (a) Entanglement entropy of a single-site in the system for different system sizes. The larger sizes begin to develop a crossing, indicative of the phase transition. (b) Scaling collapse for $\sigma_c/\bar{q} = 0.65(5)$ and $\mu = 1.0(2)$.

## D.4 Error Mitigated Fidelity Benchmarks

Here, we introduce mitigated fidelity benchmarks and demonstrate an exponential improvement in a mitigated verison of the linear cross-entropy benchmark below the error mitigation threshold.

The task of sampling from the output distribution of a noiseless random circuit is widely conjectured to be intractable with classical computers [9, 12, 139, 146]. This conjecture forms the basis for claims of achievement of quantum computational advantage in recent experiments [138, 141, 142]. The experimental claims remain controversial, however, partly because of the effects of noise on the output that render the signal classically simulatable at high depth [144, 147, 148]. To provide evidence that the output signal still remains close to the ideal case, one can estimate fidelity benchmarks using the samples from the experiment. Verifying the claim of computational advantage in the case of noisy circuits then reduces to the task of achieving a sufficiently high "score" on the benchmark [143].

Recall that the linear XEB is given by the formula [12, 138]

$$F_{\mathrm{XEB}} = 2^n \sum_x p_n(x) p_0(x) - 1, \tag{D.27}$$

where $p_0(x) = |\langle x|U_d \cdots U_1|0\rangle|^2$ is the probability of measuring outcome $x$ for the noiseless circuit of depth $d$ and $p_n(x) = \langle x|\mathcal{E}_d \circ \mathcal{U}_d \circ \cdots \mathcal{E}_1 \circ \mathcal{U}_1(|0\rangle\langle 0|)|x\rangle$ is the analogous probability for the noisy circuit.

We now introduce the mitigated linear XEB, which is instead given by the formula

$$F_{\mathrm{XEB_M}} = 2^n \sum_x p_n(x) p_a(x) - 1, \tag{D.28}$$

where $p_a(x) = \langle x|\mathcal{A}\circ\mathcal{U}_d \circ \cdots \mathcal{A}\circ\mathcal{U}_1(|0\rangle\langle 0|)|x\rangle$ is a quasi-probability for the circuit with antinoise inserted in place of noise. The quantity $p_a(x)$ can be computed on a classical computer, which

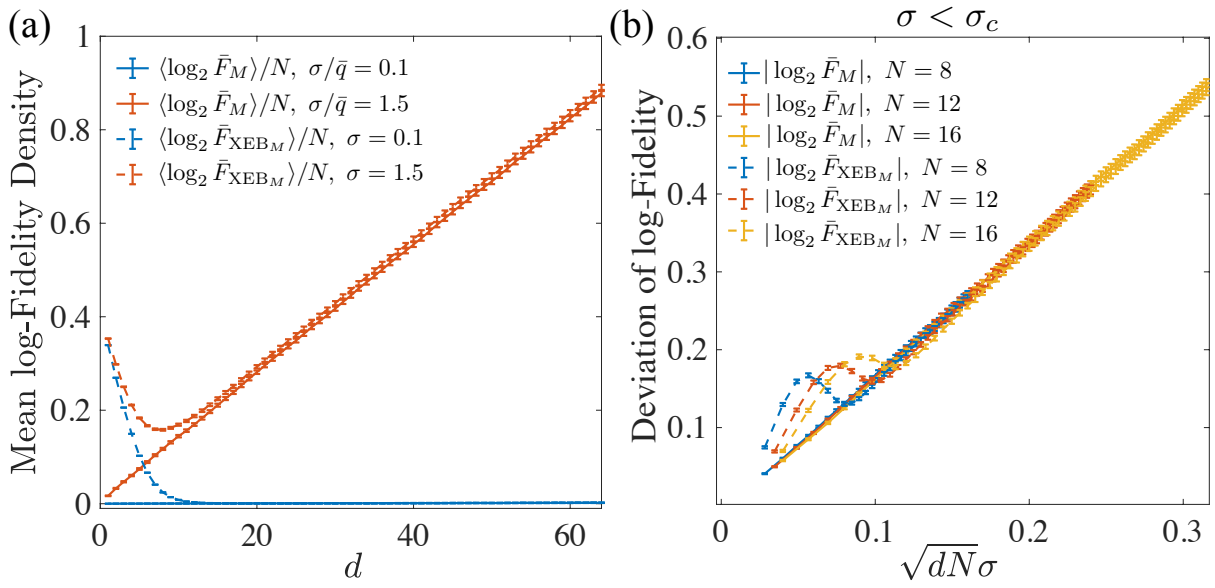


Figure D.2: Dynamics of fidelity benchmarks above and below threshold: (a) Disorder-averaged mean value of the logarithm of the circuit averaged mitigated fidelity $-\langle \log \bar{F}_M \rangle / N$ and cross-entropy benchmarking mitigated fidelity $-\langle \log F_{\mathrm{XEB}_M} \rangle / N$ above and below the error mitigation threshold in the all-to-all model. (b) Dynamics of the standard deviation over the noise of the log-circuit-averaged mitigated fidelities below threshold showing the improved scaling of the typical log-fidelity as $\pm\mathcal{O}(\sqrt{Nd})$. In both plots, we took a pure product initial state with noise parameters $\bar{q} = 0.1$ and $p = 0.9$.

leads to a sampling formula for $F_{\mathrm{XEB_M}}$ using $M$ samples $x_i$ obtained from $p_n(x)$

$$F_{\mathrm{XEB_M}} = \frac{2^n}{M} \sum_{i=1}^{M} p_a(x_i) - 1. \tag{D.29}$$

This formula illustrates that the mitigated fidelity can be obtained without directly implementing PEC except in purely classical post-processing. After circuit averaging, one can quickly show that for depolarizing noise and its antinoise partner, the mitigated fidelity is equivalent to the formula

$$\bar{F}_{\mathrm{XEB}_M} = 2^n \mathbb{E}_U \sum_x p_0(x) p_{an}(x) - 1, \tag{D.30}$$

where $p_{an}(x) = \langle x | \mathcal{A} \circ \mathcal{E}_d \circ \mathcal{U}_d \circ \cdots \mathcal{A} \circ \mathcal{E}_1 \circ \mathcal{U}_1(|0\rangle\langle 0|) | x \rangle$ implements the antinoise on the same

copy as the noise. This identity follows because the noise and antinoise on one copy have the identical effect on the $I$ and $S$ operators after averaging over circuits. From this expression, we see that, in the case of perfect mitigation, $\bar{F}_{\mathrm{XEB}_M}$ reduces to its ideal value.

We can also define a mitigated fidelity that takes the form

$$F_M = \mathrm{tr}[\mathcal{A} \circ \mathcal{U}_d \circ \cdots \circ \mathcal{A} \circ \mathcal{U}_1(|0\rangle\langle 0|) \\ \times \mathcal{E}_d \circ \mathcal{U}_d \circ \cdots \circ \mathcal{E}_1 \circ \mathcal{U}_1(|0\rangle\langle 0|)].$$

In the case where $\mathcal{E}_i = \mathcal{A}^{-1}$ for every $i$, we can see that $F_M = 1$.

In Fig. D.2], we show that the log-fidelity at low noise rates and $d$ grows as $\mathcal{O}(Nd)$, whereas using error mitigation this scaling can be improved to $\mathcal{O}(\sqrt{Nd})$, representing an exponential improvement in the score that brings it closer to the $\mathcal{O}(d)$ scaling of the log-total variation distance [133]. Moreover, as explained above, the cross-entropy benchmark fidelity can be mitigated entirely in classical post-processing. As a result, the mitigated XEB fidelity can be estimated with existing experimental data from random circuit sampling experiments.

# Bibliography


[1] Alan Edelman and N Raj Rao. Random matrix theory. *Acta numerica*, 14:233–297, 2005.

[2] Thomas Guhr, Axel Müller-Groeling, and Hans A Weidenmüller. Random-matrix theories in quantum physics: common concepts. *Physics Reports*, 299(4-6):189–425, 1998.

[3] Florence Jessie MacWilliams and Neil James Alexander Sloane. *The theory of error-correcting codes*, volume 16. Elsevier, 1977.

[4] Michael A. Nielsen and Isaac L. Chuang. *Quantum Computation and Quantum Information*. Cambridge University Press, New York, NY, USA, 10th edition, 2011.

[5] Matthew PA Fisher, Vedika Khemani, Adam Nahum, and Sagar Vijay. Random quantum circuits. *Annual Review of Condensed Matter Physics*, 14:335–379, 2023.

[6] Yulun Wang and Predrag S Krstic. Prospect of using grover's search in the noisy-intermediate-scale quantum-computer era. *Physical Review A*, 102(4):042609, 2020.

[7] Emanuel Knill, Dietrich Leibfried, Rolf Reichle, Joe Britton, R Brad Blakestad, John D Jost, Chris Langer, Roee Ozeri, Signe Seidelin, and David J Wineland. Randomized benchmarking of quantum gates. *Physical Review A*, 77(1):012307, 2008.

[8] Adam Bouland, Bill Fefferman, Chinmay Nirkhe, and Umesh Vazirani. On the complexity and verification of quantum random circuit sampling. *Nature Physics*, 15(2):159–163, 2019.

[9] Ramis Movassagh. Efficient unitary paths and quantum computational supremacy: A proof of average-case hardness of Random Circuit Sampling. 2018.

[10] Frank Arute, Kunal Arya, Ryan Babbush, Dave Bacon, Joseph C Bardin, Rami Barends, Rupak Biswas, Sergio Boixo, Fernando GSL Brandao, David A Buell, et al. Quantum supremacy using a programmable superconducting processor. *Nature*, 574(7779):505–510, 2019.

[11] A Morvan, B Villalonga, X Mi, S Mandra, A Bengtsson, PV Klimov, Z Chen, S Hong, C Erickson, IK Drozdov, et al. Phase transition in random circuit sampling. *arXiv preprint arXiv:2304.11119*, 2023.

[12] Sergio Boixo, Sergei V. Isakov, Vadim N. Smelyanskiy, Ryan Babbush, Nan Ding, Zhang Jiang, Michael J. Bremner, John M. Martinis, and Hartmut Neven. Characterizing quantum supremacy in near-term devices. *Nature Phys.*, 14(6):595–600, 2018.

[13] Brian Skinner, Jonathan Ruhman, and Adam Nahum. Measurement-Induced Phase Transitions in the Dynamics of Entanglement. *arXiv:1808.05953 [cond-mat, physics:hep-th, physics:quant-ph]*, August 2018. arXiv: 1808.05953.

[14] Yaodong Li, Romain Vasseur, Matthew P. A. Fisher, and Andreas W. W. Ludwig. Statistical Mechanics Model for Clifford Random Tensor Networks and Monitored Quantum Circuits, October 2021. arXiv:2110.02988 [cond-mat, physics:quant-ph].

[15] Pradeep Niroula, Sarang Gopalakrishnan, and Michael J Gullans. Error mitigation thresholds in noisy quantum circuits. *arXiv preprint arXiv:2302.04278*, 2023.

[16] Crystal Noel, Pradeep Niroula, Daiwei Zhu, Andrew Risinger, Laird Egan, Debopriyo Biswas, Marko Cetina, Alexey V Gorshkov, Michael J Gullans, David A Huse, et al. Measurement-induced quantum phases realized in a trapped-ion quantum computer. *Nature Physics*, 18(7):760–764, 2022.

[17] Pradeep Niroula, Christopher David White, Qingfeng Wang, Sonika Johri, Daiwei Zhu, Christopher Monroe, and Michael Gullans. Phase transition in magic with random quantum circuits, April 2023.

[18] Jonas Haferkamp. Random quantum circuits are approximate unitary $t$-designs in depth $\mathcal{O}\left(nt^{5+o(1)}\right)$. *Quantum*, 6:795, 2022.

[19] David Gross, Sepehr Nezami, and Michael Walter. Schur–weyl duality for the clifford group with applications: Property testing, a robust hudson theorem, and de finetti representations. *Communications in Mathematical Physics*, 385(3):1325–1393, 2021.

[20] Benoit Collins, Sho Matsumoto, and Jonathan Novak. The weingarten calculus. *arXiv preprint arXiv:2109.14890*, 2022.

[21] Nicholas Hunter-Jones. Unitary designs from statistical mechanics in random quantum circuits. *arXiv preprint arXiv:1905.12053*, 2019.

[22] Brayden Ware, Abhinav Deshpande, Dominik Hangleiter, Pradeep Niroula, Bill Fefferman, Alexey V Gorshkov, and Michael J Gullans. A sharp phase transition in linear cross-entropy benchmarking. *arXiv preprint arXiv:2305.04954*, 2023.

[23] Yaodong Li, Xiao Chen, and Matthew P. A. Fisher. Measurement-driven entanglement transition in hybrid quantum circuits. *Physical Review B*, 100:134306, October 2019.

[24] Piotr Sierant, Marco Schirò, Maciej Lewenstein, and Xhek Turkeshi. Measurement-induced phase transitions in (d+ 1)-dimensional stabilizer circuits. *Physical Review B*, 106(21):214316, 2022.

[25] Simone Montangero, Evenson Montangero, and Evenson. *Introduction to tensor network methods*. Springer, 2018.

[26] Stefanie Czischek, Giacomo Torlai, Sayonee Ray, Rajibul Islam, and Roger G Melko. Simulating a measurement-induced phase transition for trapped-ion circuits. *Physical Review A*, 104(6):062405, 2021.

[27] Xiaozhou Feng, Brian Skinner, and Adam Nahum. Measurement-induced phase transitions on dynamical quantum trees. *arXiv preprint arXiv:2210.07264*, 2022.

[28] Scott Aaronson and Daniel Gottesman. Improved simulation of stabilizer circuits. *Physical Review A*, 70(5):052328, 2004.

[29] Yaodong Li, Xiao Chen, and Matthew PA Fisher. Quantum zeno effect and the many-body entanglement transition. *Physical Review B*, 98(20):205136, 2018.

[30] Chao-Ming Jian, Yi-Zhuang You, Romain Vasseur, and Andreas W. W. Ludwig. Measurement-induced criticality in random quantum circuits. *Physical Review B*, 101(10):104302, March 2020. arXiv:1908.08051 [cond-mat, physics:quant-ph].

[31] Michael J. Gullans and David A. Huse. Dynamical purification phase transitions induced by quantum measurements. *Physical Review X*, 10(4):041020, October 2020. arXiv: 1905.05195.

[32] Yimu Bao, Soonwon Choi, and Ehud Altman. Theory of the phase transition in random unitary circuits with measurements. *Physical Review B*, 101(10):104301, 2020.

[33] Soonwon Choi, Yimu Bao, Xiao-Liang Qi, and Ehud Altman. Quantum error correction in scrambling dynamics and measurement-induced phase transition. *Physical Review Letters*, 125(3):030505, 2020.

[34] Michael J. Gullans and David A. Huse. Scalable probes of measurement-induced criticality. *Phys. Rev. Lett.*, 125:070606, Aug 2020.

[35] Lorenzo Leone, Salvatore FE Oliviero, Gianluca Esposito, and Alioscia Hamma. Phase transition in stabilizer entropy and efficient purity estimation. *arXiv preprint arXiv:2302.07895*, 2023.

[36] Victor Veitch, Seyed Ali Hamed Mousavian, Daniel Gottesman, and Joseph Emerson. The Resource Theory of Stabilizer Computation. *New Journal of Physics*, 16(1):013009, January 2014. arXiv: 1307.7171.

[37] Lorenzo Leone, Salvatore FE Oliviero, You Zhou, and Alioscia Hamma. Quantum chaos is quantum. *Quantum*, 5:453, 2021.

[38] Sergei Bravyi and Alexei Kitaev. Universal Quantum Computation with ideal Clifford gates and noisy ancillas. *Physical Review A*, 71(2):022316, February 2005. arXiv: quant-ph/0403025.

[39] Salvatore FE Oliviero, Lorenzo Leone, Alioscia Hamma, and Seth Lloyd. Measuring magic on a quantum processor. *npj Quantum Information*, 8(1):148, 2022.

[40] Steven T Flammia and Yi-Kai Liu. Direct fidelity estimation from few pauli measurements. *Physical review letters*, 106(23):230501, 2011.

[41] Xun Gao, Marcin Kalinowski, Chi-Ning Chou, Mikhail D. Lukin, Boaz Barak, and Soonwon Choi. Limitations of Linear Cross-Entropy as a Measure for Quantum Advantage. 2021.

[42] Zhenyu Cai, Ryan Babbush, Simon C Benjamin, Suguru Endo, William J Huggins, Ying Li, Jarrod R McClean, and Thomas E O'Brien. Quantum error mitigation. *arXiv preprint arXiv:2210.00921*, 2022.

[43] Howard Carmichael. *An open systems approach to quantum optics*. Springer, Berlin, Germany, 1993.

[44] C. W. Gardiner and P. Zoller. *Quantum Noise*. Springer, Berlin, Germany, 2000.

[45] Brian Skinner, Jonathan Ruhman, and Adam Nahum. Measurement-induced phase transitions in the dynamics of entanglement. *Phys. Rev. X*, 9:031009, Jul 2019.

[46] Yaodong Li, Xiao Chen, and Matthew P. A. Fisher. Quantum zeno effect and the many-body entanglement transition. *Phys. Rev. B*, 98:205136, Nov 2018.

[47] Yaodong Li, Xiao Chen, and Matthew P. A. Fisher. Measurement-driven entanglement transition in hybrid quantum circuits. *Phys. Rev. B*, 100:134306, Oct 2019.

[48] Michael J. Gullans and David A. Huse. Dynamical purification phase transition induced by quantum measurements. *Phys. Rev. X*, 10:041020, Oct 2020.

[49] Soonwon Choi, Yimu Bao, Xiao-Liang Qi, and Ehud Altman. Quantum error correction in scrambling dynamics and measurement-induced phase transition. *Phys. Rev. Lett.*, 125:030505, Jul 2020.

[50] Chao-Ming Jian, Yi-Zhuang You, Romain Vasseur, and Andreas W. W. Ludwig. Measurement-induced criticality in random quantum circuits. *Phys. Rev. B*, 101:104302, Mar 2020.

[51] Yimu Bao, Soonwon Choi, and Ehud Altman. Theory of the phase transition in random unitary circuits with measurements. *Phys. Rev. B*, 101:104301, Mar 2020.

[52] Dorit Aharonov. Quantum to classical phase transition in noisy quantum computers. *Phys. Rev. A*, 62(6):062311, November 2000.

[53] Daniel Gottesman. An Introduction to Quantum Error Correction and Fault-Tolerant Quantum Computation. *arXiv:0904.2557*, April 2009.

[54] Tiff Brydges, Andreas Elben, Petar Jurcevic, Benoît Vermersch, Christine Maier, Ben P. Lanyon, Peter Zoller, Rainer Blatt, and Christian F. Roos. Probing rényi entanglement entropy via randomized measurements. *Science*, 364(6437):260–263, 2019.

[55] E Schrödinger. Probability relations between separated systems. *Math. Proc. Camb. Philos. Soc.*, 32(3):446–452, October 1936.

[56] David J. Wineland. Nobel lecture: Superposition, entanglement, and raising schrödinger's cat. *Rev. Mod. Phys.*, 85:1103–1114, Jul 2013.

[57] Serge Haroche. Nobel lecture: Controlling photons in a box and exploring the quantum to classical boundary. *Rev. Mod. Phys.*, 85:1083–1102, Jul 2013.

[58] Z. K. Minev, S. O. Mundhada, S. Shankar, P. Reinhold, R. Gutiérrez-Jáuregui, R. J. Schoelkopf, M. Mirrahimi, H. J. Carmichael, and M. H. Devoret. To catch and reverse a quantum jump mid-flight. *Nature*, 570(7760):200–204, 2019.

[59] Julio T Barreiro, Markus Müller, Philipp Schindler, Daniel Nigg, Thomas Monz, Michael Chwalla, Markus Hennrich, Christian F Roos, Peter Zoller, and Rainer Blatt. An open-system quantum simulator with trapped ions. *Nature*, 470(7335):486–491, February 2011.

[60] Dayou Yang, Andrey Grankin, Lukas M Sieberer, Denis V Vasilyev, and Peter Zoller. Quantum non-demolition measurement of a many-body Hamiltonian. *Nature Commun.*, 11(1):1–8, February 2020.

[61] Vittorio Vitale, Andreas Elben, Richard Kueng, Antoine Neven, Jose Carrasco, Barbara Kraus, Peter Zoller, Pasquale Calabrese, Benoit Vermersch, and Marcello Dalmonte. Symmetry-resolved dynamical purification in synthetic quantum matter. *arXiv:2101.07814*, 2021.

[62] Peter Lukas Wilhelm Maunz. High optical access trap 2.0. *Sandia National Laboratories Report No. SAND2016-0796R*, 2016.

[63] Laird Egan, Dripto M. Debroy, Crystal Noel, Andrew Risinger, Daiwei Zhu, Debopriyo Biswas, Michael Newman, Muyuan Li, Kenneth R. Brown, Marko Cetina, and Christopher Monroe. Fault-tolerant control of an error-corrected qubit. *Nature*, 598(7880):281–286, 2021.

[64] Michael Foss-Feig, Stephen Ragole, Andrew Potter, Joan Dreiling, Caroline Figgatt, John Gaebler, Alex Hall, Steven Moses, Juan Pino, Ben Spaun, Brian Neyenhuis, and David Hayes. Entanglement from tensor networks on a trapped-ion qccd quantum computer. *arXiv:2104.11235*, 2021.

[65] Daniel Gottesman. The heisenberg representation of quantum computers. In *Proc. XXII International Colloquium on Group Theoretical Methods in Physics*, pages 32–43, Cambridge, MA, 1998. International Press.

[66] Scott Aaronson and Daniel Gottesman. Improved simulation of stabilizer circuits. *Phys. Rev. A*, 70(5):052328, 2004.

[67] Matteo Ippoliti, Michael J. Gullans, Sarang Gopalakrishnan, David A. Huse, and Vedika Khemani. Entanglement phase transitions in measurement-only dynamics. *Phys. Rev. X*, 11:011030, Feb 2021.

[68] M Cetina, LN Egan, CA Noel, ML Goldman, AR Risinger, D Zhu, D Biswas, and C Monroe. Quantum gates on individually-addressed atomic qubits subject to noisy transverse motion. *arXiv:2007.06768*, 2020.

[69] Ali Lavasani, Yahya Alavirad, and Maissam Barkeshli. Measurement-induced topological entanglement transitions in symmetric random quantum circuits. *Nature Phys.*, 17(3):342–347, March 2021.

[70] Shengqi Sang and Timothy H. Hsieh. Measurement-protected quantum phases. *Phys. Rev. Research*, 3:023200, Jun 2021.

[71] John Napp, Rolando L La Placa, Alexander M Dalzell, Fernando G S L Brandao, and Aram W Harrow. Efficient classical simulation of random shallow 2D quantum circuits. *arXiv:2001.00021*, December 2020.

[72] Michael J. Gullans, Stefan Krastanov, David A. Huse, Liang Jiang, and Steven T. Flammia. Quantum coding with low-depth random circuits. *Phys. Rev. X*, 11:031066, Sep 2021.

[73] Daniel Gottesman. The heisenberg representation of quantum computers. *arXiv preprint quant-ph/9807006*, 1998.

[74] Scott Aaronson and Daniel Gottesman. Improved Simulation of Stabilizer Circuits. *Physical Review A*, 70(5):052328, November 2004.

[75] Sergey Bravyi, Dan Browne, Padraic Calpin, Earl Campbell, David Gosset, and Mark Howard. Simulation of quantum circuits by low-rank stabilizer decompositions. *arXiv e-prints*, 1808:arXiv:1808.00128, July 2018.

[76] Kaifeng Bu and Dax Enshan Koh. Efficient classical simulation of Clifford circuits with nonstabilizer input states. *arXiv e-prints*, 1902:arXiv:1902.11257, February 2019.

[77] Austin G. Fowler, Matteo Mariantoni, John M. Martinis, and Andrew N. Cleland. Surface codes: Towards practical large-scale quantum computation. *Physical Review A*, 86(3):032324, September 2012.

[78] Joe O'Gorman and Earl T. Campbell. Quantum computation with realistic magic-state factories. *Physical Review A*, 95(3):032338, March 2017.

[79] Earl T. Campbell, Barbara M. Terhal, and Christophe Vuillot. Roads towards fault-tolerant universal quantum computation. *Nature*, 549(7671):172–179, September 2017.

[80] Kaifeng Bu, Roy J. Garcia, Arthur Jaffe, Dax Enshan Koh, and Lu Li. Complexity of quantum circuits via sensitivity, magic, and coherence. *arXiv:2204.12051 [math-ph, physics:quant-ph]*, April 2022.

[81] Christopher David White, ChunJun Cao, and Brian Swingle. Conformal field theories are magical. *Physical Review B*, 103(7):075145, February 2021.

[82] Barbara M. Terhal. Quantum error correction for quantum memories. *Rev. Mod. Phys.*, 87:307–346, Apr 2015.

[83] Andrew C. Potter and Romain Vasseur. Entanglement dynamics in hybrid quantum circuits. pages 211–249. 2022. arXiv:2111.08018 [cond-mat, physics:quant-ph].

[84] Aidan Zabalo, Michael J. Gullans, Justin H. Wilson, Sarang Gopalakrishnan, David A. Huse, and J. H. Pixley. Critical properties of the measurement-induced transition in random quantum circuits. *Physical Review B*, 101(6):060301, February 2020. Publisher: American Physical Society.

[85] Aidan Zabalo, Michael J. Gullans, Justin H. Wilson, Romain Vasseur, Andreas W. W. Ludwig, Sarang Gopalakrishnan, David A. Huse, and J. H. Pixley. Operator scaling dimensions and multifractality at measurement-induced transitions. *arXiv:2107.03393 [cond-mat, physics:quant-ph]*, July 2021. arXiv: 2107.03393.

[86] Jason Iaconis, Andrew Lucas, and Xiao Chen. Measurement-induced phase transitions in quantum automaton circuits. *Physical Review B*, 102(22):224311, December 2020. Publisher: American Physical Society.

[87] Fergus Barratt, Utkarsh Agrawal, Sarang Gopalakrishnan, David A. Huse, Romain Vasseur, and Andrew C. Potter. Field theory of charge sharpening in symmetric monitored quantum circuits. *Physical Review Letters*, 129(12):120604, September 2022. arXiv:2111.09336 [cond-mat, physics:quant-ph].

[88] Utkarsh Agrawal, Aidan Zabalo, Kun Chen, Justin H Wilson, Andrew C Potter, JH Pixley, Sarang Gopalakrishnan, and Romain Vasseur. Entanglement and charge-sharpening transitions in u (1) symmetric monitored quantum circuits. *Physical Review X*, 12(4):041002, 2022.

[89] Lorenzo Leone, Salvatore F. E. Oliviero, and Alioscia Hamma. Stabilizer R\'enyi entropy. *Physical Review Letters*, 128(5):050402, February 2022. arXiv:2106.12587 [quant-ph].

[90] Winton Brown and Omar Fawzi. Short random circuits define good quantum error correcting codes. In *2013 IEEE International Symposium on Information Theory*, pages 346–350. IEEE, 2013.

[91] Daniel Gottesman. *Stabilizer codes and quantum error correction*. California Institute of Technology, 1997.

[92] IonQ: Getting started with native gates. `https://ionq.com/docs/getting-started-with-native-gates`. Accessed: 2023-04-23.

[93] Andrii Maksymov, Jason Nguyen, Yunseong Nam, and Igor Markov. Enhancing quantum computer performance via symmetrization. *arXiv preprint arXiv:2301.07233*, 2023.

[94] Matteo Ippoliti, Michael J. Gullans, Sarang Gopalakrishnan, David A. Huse, and Vedika Khemani. Entanglement phase transitions in measurement-only dynamics. *Physical Review X*, 11(1):011030, February 2021.

[95] Sergey Bravyi, Matthias Englbrecht, Robert König, and Nolan Peard. Correcting coherent errors with surface codes. *npj Quantum Inf.*, 4(1):55, 2018.

[96] D. Aharonov and M. Ben-Or. Fault-tolerant quantum computation with constant error. In *Proceedings of the Twenty-Ninth Annual ACM Symposium on Theory of Computing - STOC '97*, pages 176–188, El Paso, Texas, United States, 1997. ACM Press.

[97] Eric Dennis, Alexei Kitaev, Andrew Landahl, and John Preskill. Topological quantum memory. *J. Math. Phys.*, 43(9):4452–4505, August 2002.

[98] Sebastian Krinner, Nathan Lacroix, Ants Remm, Agustin Di Paolo, Elie Genois, Catherine Leroux, Christoph Hellings, Stefania Lazar, Francois Swiadek, Johannes Herrmann, Graham J. Norris, Christian Kraglund Andersen, Markus Müller, Alexandre Blais, Christopher Eichler, and Andreas Wallraff. Realizing repeated quantum error correction in a distance-three surface code. *Nature*, 605(7911):669–674, 2022.

[99] Rajeev Acharya, Igor Aleiner, Richard Allen, Trond I. Andersen, Markus Ansmann, Frank Arute, Kunal Arya, Abraham Asfaw, Juan Atalaya, Ryan Babbush, Dave Bacon, Joseph C. Bardin, Joao Basso, Andreas Bengtsson, Sergio Boixo, Gina Bortoli, Alexandre Bourassa, Jenna Bovaird, Leon Brill, Michael Broughton, Bob B. Buckley, David A. Buell, Tim Burger, Brian Burkett, Nicholas Bushnell, Yu Chen, Zijun Chen, Ben Chiaro, Josh Cogan, Roberto Collins, Paul Conner, William Courtney, Alexander L. Crook, Ben Curtin, Dripto M. Debroy, Alexander Del Toro Barba, Sean Demura, Andrew Dunsworth, Daniel Eppens, Catherine Erickson, Lara Faoro, Edward Farhi, Reza Fatemi, Leslie Flores Burgos, Ebrahim Forati, Austin G. Fowler, Brooks Foxen, William Giang, Craig Gidney, Dar Gilboa, Marissa Giustina, Alejandro Grajales Dau, Jonathan A. Gross, Steve Habegger, Michael C. Hamilton, Matthew P. Harrigan, Sean D. Harrington, Oscar Higgott, Jeremy Hilton, Markus Hoffmann, Sabrina Hong, Trent Huang, Ashley Huff, William J. Huggins, Lev B. Ioffe, Sergei V. Isakov, Justin Iveland, Evan Jeffrey, Zhang Jiang, Cody Jones, Pavol Juhas, Dvir Kafri, Kostyantyn Kechedzhi, Julian Kelly, Tanuj Khattar, Mostafa Khezri, Mária Kieferová, Seon Kim, Alexei Kitaev, Paul V. Klimov, Andrey R. Klots, Alexander N. Korotkov, Fedor Kostritsa, John Mark Kreikebaum, David Landhuis, Pavel Laptev, Kim-Ming Lau, Lily Laws, Joonho Lee, Kenny Lee, Brian J. Lester, Alexander Lill, Wayne Liu, Aditya Locharla, Erik Lucero, Fionn D. Malone, Jeffrey Marshall, Orion Martin, Jarrod R. McClean, Trevor Mccourt, Matt McEwen, Anthony Megrant, Bernardo Meurer Costa, Xiao Mi, Kevin C. Miao, Masoud Mohseni, Shirin Montazeri, Alexis Morvan, Emily Mount, Wojciech Mruczkiewicz, Ofer Naaman, Matthew Neeley, Charles Neill, Ani Nersisyan, Hartmut Neven, Michael Newman, Jiun How Ng, Anthony Nguyen, Murray Nguyen, Murphy Yuezhen Niu, Thomas E. O'Brien, Alex Opremcak, John Platt, Andre Petukhov, Rebecca Potter, Leonid P. Pryadko,

Chris Quintana, Pedram Roushan, Nicholas C. Rubin, Negar Saei, Daniel Sank, Kannan Sankaragomathi, Kevin J. Satzinger, Henry F. Schurkus, Christopher Schuster, Michael J. Shearn, Aaron Shorter, Vladimir Shvarts, Jindra Skruzny, Vadim Smelyanskiy, W. Clarke Smith, George Sterling, Doug Strain, Marco Szalay, Alfredo Torres, Guifre Vidal, Benjamin Villalonga, Catherine Vollgraff Heidweiller, Theodore White, Cheng Xing, Z. Jamie Yao, Ping Yeh, Juhwan Yoo, Grayson Young, Adam Zalcman, Yaxing Zhang, and Ningfeng Zhu. Suppressing quantum errors by scaling a surface code logical qubit. *arXiv:2207.06431*, 2022.

[100] V V Sivak, A Eickbusch, B Royer, S Singh, I Tsioutsios, S Ganjam, A Miano, B L Brock, A Z Ding, L Frunzio, S M Girvin, R J Schoelkopf, and M H Devoret. Real-time quantum error correction beyond break-even. *arXiv*, 2022.

[101] Sam McArdle, Suguru Endo, Alán Aspuru-Guzik, Simon C Benjamin, and Xiao Yuan. Quantum computational chemistry. *Rev. Mod. Phys.*, 92(1):015003, 2020.

[102] Kristan Temme, Sergey Bravyi, and Jay M. Gambetta. Error mitigation for short-depth quantum circuits. *Phys. Rev. Lett.*, 119:180509, Nov 2017.

[103] Ying Li and Simon C. Benjamin. Efficient variational quantum simulator incorporating active error minimization. *Phys. Rev. X*, 7:021050, Jun 2017.

[104] Youngseok Kim, Christopher J. Wood, Theodore J. Yoder, Seth T. Merkel, Jay M. Gambetta, Kristan Temme, and Abhinav Kandala. Scalable error mitigation for noisy quantum circuits produces competitive expectation values. *Nature Phys.*, 2023.

[105] Jarrod R. McClean, Mollie E. Kimchi-Schwartz, Jonathan Carter, and Wibe A. de Jong. Hybrid quantum-classical hierarchy for mitigation of decoherence and determination of excited states. *Phys. Rev. A*, 95:042308, Apr 2017.

[106] X. Bonet-Monroig, R. Sagastizabal, M. Singh, and T. E. O'Brien. Low-cost error mitigation by symmetry verification. *Phys. Rev. A*, 98:062339, Dec 2018.

[107] Sam McArdle, Xiao Yuan, and Simon Benjamin. Error-mitigated digital quantum simulation. *Phys. Rev. Lett.*, 122:180501, May 2019.

[108] Jordan Cotler, Soonwon Choi, Alexander Lukin, Hrant Gharibyan, Tarun Grover, M. Eric Tai, Matthew Rispoli, Robert Schittko, Philipp M. Preiss, Adam M. Kaufman, Markus Greiner, Hannes Pichler, and Patrick Hayden. Quantum virtual cooling. *Phys. Rev. X*, 9:031013, Jul 2019.

[109] William J. Huggins, Sam McArdle, Thomas E. O'Brien, Joonho Lee, Nicholas C. Rubin, Sergio Boixo, K. Birgitta Whaley, Ryan Babbush, and Jarrod R. McClean. Virtual distillation for quantum error mitigation. *Phys. Rev. X*, 11:041036, Nov 2021.

[110] Bálint Koczor. Exponential error suppression for near-term quantum devices. *Phys. Rev. X*, 11:031057, Sep 2021.

[111] Piotr Czarnik, Andrew Arrasmith, Patrick J. Coles, and Lukasz Cincio. Error mitigation with Clifford quantum-circuit data. *Quantum*, 5:592, 2021.

[112] Armands Strikis, Dayue Qin, Yanzhu Chen, Simon C. Benjamin, and Ying Li. Learning-based quantum error mitigation. *PRX Quantum*, 2:040330, Nov 2021.

[113] Joseph Emerson, Robert Alicki, and Karol Życzkowski. Scalable noise estimation with random unitary operators. *J Opt. B Quantum Semiclassical Opt.*, 7(10):S347 – S352, 10 2005.

[114] E. Knill, D. Leibfried, R. Reichle, J. Britton, R. B. Blakestad, J. D. Jost, C. Langer, R. Ozeri, S. Seidelin, and D. J. Wineland. Randomized benchmarking of quantum gates. *Phys. Rev. A*, 77:012307, Jan 2008.

[115] Erik Nielsen, John King Gamble, Kenneth Rudinger, Travis Scholten, Kevin Young, and Robin Blume-Kohout. Gate Set Tomography. *Quantum*, 5:557, 2021.

[116] S. T. Flammia and J. J. Wallman, ACM Transactions on Quantum Computing 1 (1), 1-32 (2020). arXiv:1907.12976.

[117] Robin Harper, Steven T Flammia, and Joel J Wallman. Efficient learning of quantum noise. *Nature Physics*, 332:1059, 08 2020.

[118] Eyal Bairey, Itai Arad, and Netanel H. Lindner. Learning a Local Hamiltonian from Local Measurements. *Physical Review Letters*, 122(2):020504, 2019.

[119] Anurag Anshu, Srinivasan Arunachalam, Tomotaka Kuwahara, and Mehdi Soleimanifar. Sample-efficient learning of interacting quantum systems. *Nature Physics*, 17(8):931–935, 2021.

[120] Ewout van den Berg, Zlatko K Minev, Abhinav Kandala, and Kristan Temme. Probabilistic error cancellation with sparse Pauli-Lindblad models on noisy quantum processors. *arXiv:2201.09866*, 2022.

[121] Matthew P. A. Fisher, Vedika Khemani, Adam Nahum, and Sagar Vijay. Random quantum circuits, 2022.

[122] A C Potter and R Vasseur. Entanglement dynamics in hybrid quantum circuits. In *Entanglement in Spin Chains*, Quantum Science and Technology, pages 211–249. Springer, 2022.

[123] Yoseph Imry and Shang-keng Ma. Random-field instability of the ordered state of continuous symmetry. *Phys. Rev. Lett.*, 35:1399–1401, Nov 1975.

[124] Adam Nahum, Jonathan Ruhman, Sagar Vijay, and Jeongwan Haah. Quantum entanglement growth under random unitary dynamics. *Phys. Rev. X*, 7:031016, Jul 2017.

[125] Adam Nahum, Sagar Vijay, and Jeongwan Haah. Operator spreading in random unitary circuits. *Phys. Rev. X*, 8:021014, Apr 2018.

[126] C. W. von Keyserlingk, Tibor Rakovszky, Frank Pollmann, and S. L. Sondhi. Operator hydrodynamics, otocs, and entanglement growth in systems without conservation laws. *Phys. Rev. X*, 8:021013, Apr 2018.

[127] Jinzhao Sun, Xiao Yuan, Takahiro Tsunoda, Vlatko Vedral, Simon C. Benjamin, and Suguru Endo. Mitigating realistic noise in practical noisy intermediate-scale quantum devices. *Phys. Rev. Appl.*, 15:034026, Mar 2021.

[128] Nima Lashkari, Douglas Stanford, Matthew Hastings, Tobias Osborne, and Patrick Hayden. Towards the fast scrambling conjecture. *J. High Energy Phys.*, 2013(4):22, 2013.

[129] Shao-Kai Jian, Gregory Bentsen, and Brian Swingle. Linear Growth of Circuit Complexity from Brownian Dynamics. *arXiv:2206.14205*, 2022.

[130] Chao-Ming Jian, Yi-Zhuang You, Romain Vasseur, and Andreas W. W. Ludwig. Measurement-induced criticality in random quantum circuits. *Phys. Rev. B*, 101:104302, Mar 2020.

[131] Alexander M. Dalzell, Nicholas Hunter-Jones, and Fernando G. S. L. Brandão. Random quantum circuits anticoncentrate in log depth. *PRX Quantum*, 3:010333, Mar 2022.

[132] Alexander M. Dalzell, Nicholas Hunter-Jones, and Fernando G. S. L. Brandão. Random quantum circuits transform local noise into global white noise. 2021.

[133] Abhinav Deshpande, Pradeep Niroula, Oles Shtanko, Alexey V. Gorshkov, Bill Fefferman, and Michael J. Gullans. Tight bounds on the convergence of noisy random circuits to the uniform distribution. *PRX Quantum*, 3:040329, Dec 2022.

[134] Xun Gao, Marcin Kalinowski, Chi-Ning Chou, Mikhail D Lukin, Boaz Barak, and Soonwon Choi. Limitations of Linear Cross-Entropy as a Measure for Quantum Advantage. *arXiv:2112.01657*, 2021.

[135] D P DiVincenzo, D W Leung, and B M Terhal. Quantum data hiding. *IEEE Transactions on Information Theory*, 48(3):580 – 598, 2002-03.

[136] Brian Skinner, Jonathan Ruhman, and Adam Nahum. Measurement-Induced Phase Transitions in the Dynamics of Entanglement. *Phys. Rev. X*, 9(3):031009, 2019.

[137] Yaodong Li, Xiao Chen, and Matthew P. A. Fisher. Measurement-driven entanglement transition in hybrid quantum circuits. *Phys. Rev. B*, 100:134306, Oct 2019.

[138] Frank Arute, Kunal Arya, Ryan Babbush, Dave Bacon, Joseph C. Bardin, Rami Barends, Rupak Biswas, Sergio Boixo, Fernando G. S. L. Brandao, David A. Buell, Brian Burkett, Yu Chen, Zijun Chen, Ben Chiaro, Roberto Collins, William Courtney, Andrew Dunsworth, Edward Farhi, Brooks Foxen, Austin Fowler, Craig Gidney, Marissa Giustina, Rob Graff, Keith Guerin, Steve Habegger, Matthew P. Harrigan, Michael J. Hartmann, Alan Ho, Markus Hoffmann, Trent Huang, Travis S. Humble, Sergei V. Isakov, Evan Jeffrey, Zhang Jiang, Dvir Kafri, Kostyantyn Kechedzhi, Julian Kelly, Paul V. Klimov, Sergey Knysh, Alexander Korotkov, Fedor Kostritsa, David Landhuis, Mike Lindmark,

Erik Lucero, Dmitry Lyakh, Salvatore Mandrà, Jarrod R. McClean, Matthew McEwen, Anthony Megrant, Xiao Mi, Kristel Michielsen, Masoud Mohseni, Josh Mutus, Ofer Naaman, Matthew Neeley, Charles Neill, Murphy Yuezhen Niu, Eric Ostby, Andre Petukhov, John C. Platt, Chris Quintana, Eleanor G. Rieffel, Pedram Roushan, Nicholas C. Rubin, Daniel Sank, Kevin J. Satzinger, Vadim Smelyanskiy, Kevin J. Sung, Matthew D. Trevithick, Amit Vainsencher, Benjamin Villalonga, Theodore White, Z. Jamie Yao, Ping Yeh, Adam Zalcman, Hartmut Neven, and John M. Martinis. Quantum supremacy using a programmable superconducting processor. *Nature*, 574(7779):505–510, 2019.

[139] Adam Bouland, Bill Fefferman, Chinmay Nirkhe, and Umesh Vazirani. On the complexity and verification of quantum random circuit sampling. *Nature Phys.*, 15(2):159–163, 2019.

[140] Ramis Movassagh. Quantum supremacy and random circuits. 2019.

[141] Yulin Wu, Wan-Su Bao, Sirui Cao, Fusheng Chen, Ming-Cheng Chen, Xiawei Chen, Tung-Hsun Chung, Hui Deng, Yajie Du, Daojin Fan, Ming Gong, Cheng Guo, Chu Guo, Shaojun Guo, Lianchen Han, Linyin Hong, He-Liang Huang, Yong-Heng Huo, Liping Li, Na Li, Shaowei Li, Yuan Li, Futian Liang, Chun Lin, Jin Lin, Haoran Qian, Dan Qiao, Hao Rong, Hong Su, Lihua Sun, Liangyuan Wang, Shiyu Wang, Dachao Wu, Yu Xu, Kai Yan, Weifeng Yang, Yang Yang, Yangsen Ye, Jianghan Yin, Chong Ying, Jiale Yu, Chen Zha, Cha Zhang, Haibin Zhang, Kaili Zhang, Yiming Zhang, Han Zhao, Youwei Zhao, Liang Zhou, Qingling Zhu, Chao-Yang Lu, Cheng-Zhi Peng, Xiaobo Zhu, and Jian-Wei Pan. Strong quantum computational advantage using a superconducting quantum processor. *Phys. Rev. Lett.*, 127:180501, Oct 2021.

[142] Qingling Zhu, Sirui Cao, Fusheng Chen, Ming-Cheng Chen, Xiawei Chen, Tung-Hsun Chung, Hui Deng, Yajie Du, Daojin Fan, Ming Gong, Cheng Guo, Chu Guo, Shaojun Guo, Lianchen Han, Linyin Hong, He-Liang Huang, Yong-Heng Huo, Liping Li, Na Li, Shaowei Li, Yuan Li, Futian Liang, Chun Lin, Jin Lin, Haoran Qian, Dan Qiao, Hao Rong, Hong Su, Lihua Sun, Liangyuan Wang, Shiyu Wang, Dachao Wu, Yulin Wu, Yu Xu, Kai Yan, Weifeng Yang, Yang Yang, Yangsen Ye, Jianghan Yin, Chong Ying, Jiale Yu, Chen Zha, Cha Zhang, Haibin Zhang, Kaili Zhang, Yiming Zhang, Han Zhao, Youwei Zhao, Liang Zhou, Chao-Yang Lu, Cheng-Zhi Peng, Xiaobo Zhu, and Jian-Wei Pan. Quantum Computational Advantage via 60-Qubit 24-Cycle Random Circuit Sampling. *arXiv:2109.03494*, 2021.

[143] Scott Aaronson and Sam Gunn. On the Classical Hardness of Spoofing Linear Cross-Entropy Benchmarking. *arXiv*, 2019.

[144] Adam Bouland, Bill Fefferman, Zeph Landau, and Yunchao Liu. Noise and the frontier of quantum supremacy. 2021.

[145] D. Aharonov, M. Ben-Or, R. Impagliazzo, and N. Nisan. Limitations of Noisy Reversible Computation. 1996.

[146] Dominik Hangleiter and Jens Eisert. Computational advantage of quantum random sampling. *arXiv:2206.04079*, 2022.

[147] Xun Gao and Luming Duan. Efficient classical simulation of noisy quantum computation. 2018.

[148] Dorit Aharonov, Xun Gao, Zeph Landau, Yunchao Liu, and Umesh Vazirani. A polynomial-time classical algorithm for noisy random circuit sampling. *arXiv:2211.03999*, 2022.